Institut für Astronomische und Physikalische Geodäsie

Gravity Field Analysis from the Satellite Missions CHAMP and GOCE

Martin K. Wermuth

Vollständiger Abdruck der von der Fakultät für Bauingenieur- und Vermessungswesen der Technischen Universität München zur Erlangung des akademischen Grades eines

Doktor-Ingenieurs (Dr.-Ing.)

genehmigten Dissertation.

Vorsitzender:	Univ.-Prof. Dr.-Ing. U. Stilla
Prüfer der Dissertation:	
	1. Univ.-Prof. Dr.-Ing., Dr. h.c. R. Rummel
	2. Univ.-Prof. Dr.-Ing. N. Sneeuw, Universität Stuttgart

Die Dissertation wurde am 04.03.2008 bei der Technischen Universität München eingereicht und durch die Fakultät für Bauingenieur- und Vermessungswesen am 04.07.2008 angenommen.

Zusammenfassung

In dieser Arbeit ist die Bestimmung von globalen Schwerefeldmodellen aus Beobachtungen der Satellitenmissionen CHAMP und GOCE beschrieben. Im Fall von CHAMP wird die sogenannte Energieerhaltungs-Methode auf GPS Beobachtungen des tief fliegenden CHAMP Satelliten angewandt. Im Fall von GOCE ist Gradiometrie die wichtigste Beobachtungsgröße. Die Erfahrung die bei der Verarbeitung von Echtdaten der CHAMP Mission gewonnen wurde, fließt in die Entwicklung einer operationellen Quick-look Software für die GOCE Mission ein. Die Aufgabe globaler Schwerefeldbestimmung ist es, aus Beobachtungen entlang einer Satellitenbahn ein Model des Gravitationsfeldes der Erde abzuleiten, das auf der Erdoberfläche in sphärisch-harmonischen Koeffizienten beschrieben wird. Die theoretischen Grundlagen, die nötig sind um die Beobachtungen mit dem Schwerefeld in Bezug zu setzen und ein globales Schwerefeld aus Satellitenbeobachtungen zu berechnen sind werden ausführlich erklärt.

Die CHAMP Mission wurde im Jahr 2000 gestartet. Sie ist die erste Schwerefeldmission mit einem GPS Empfänger an Bord. Die Hauptbeobachtungsgrößen sind die GPS Bahn-Beobachtungen zu CHAMP, das sogenannte "satellite-to-satellite tracking" (SST). Ein Schwerefeldmodell wird mit der Energieerhaltungs-Methode unter Verwendung von kinematischen Bahnen berechnet. Die Methode beruht auf dem Energieerhaltungssatz, der besagt, dass die Summe aus kinetischer und potenzieller Energie in einem konservativen Kraftfeld konstant bleibt. Die kinetische Energie kann aus den Positionen der Satellitenbahn über die Geschwindigkeiten berechnet werden. Die unbekannte Energiekonstante kann aus den Beobachtungen geschätzt werden und damit das Schwerepotenzial berechnet werden. Der Satellit ist nicht-konservativen Kräften ausgesetzt, deren Einfluss berücksichtigt werden muss. Diese Kräfte können zum Teil mit dem an Bord befindlichen Beschleunigungsmesser erfasst werden und zum Teil aus Modellen berechnet werden. Die sphärisch-harmonischen Koeffizienten werden dann aus den Potenzialwerten, die entlang der Bahn gegeben sind in einer Ausgleichung nach kleinsten Quadraten bestimmt. Die Lösung wird mit Hilfe von Daten aus GPS-Nivellements validiert und mit anderen globalen Schwerefeldlösungen verglichen.

Der Start der GOCE Mission ist für Anfang 2009 geplant. Sie ist die erste Mission bei der Gradiometrie im All verwendet wird. Die bandbgrenzten "satellite gravity gradiometry" (SGG) Beobachtungen werden von SST komplementiert. Aufgrund der komplexen Datenauswertung werden die endgültigen Resultate erst mehrere Wochen nach Ende der Mission verfügbar sein. Da es aber nötig ist, die Daten parallel zur Mission zu analysieren wurde eine Quick-look Schwerefeldanalyse entwickelt. Sie benützt den semi-analytischen Ansatz, der auf der vereinfachenden Annahme einer kreisförmigen Bahn beruht. Diese Vereinfachung ermöglicht die Verwendung von schnellen Fourier-Transformationen (FFT) bei der Aufstellung der Normalgleichungen. Die Normalgleichungen werden blockdiagonal und können sehr effizient gelöst werden. Der Geschwindigkeitsgewinn wird allerdings durch eine schlechtere Genauigkeit erkauft. Die Methode kann in zwei verschiedene Ansätze unterteilt werden: den 1D-FFT Ansatz und den 2D-FFT Ansatz - auch als Torus-Ansatz bekannt. Die beiden Ansätze werden auf echte CHAMP-Daten und simulierte GOCE-Daten angewandt um ihre Vor- und Nachteile zu bewerten.

Abstract

This work describes global gravity field modeling from observations of the CHAMP and the GOCE satellite mission. In the case of CHAMP the so-called Energy Balance Approach is applied to measurements of GPS high-low tracking of the low orbiting CHAMP spacecraft. In the case of GOCE gravity gradiometry is the main observable. The experience gained processing real data of the CHAMP satellite mission is incorporated in the development of operational quick-look software for the GOCE mission. The task of global gravity field analysis is to derive from measurements along the satellite orbit a model of the Earth's gravitational field expressed in spherical harmonic coefficients on the Earth's surface. The theoretical background needed to relate the observations to the gravity field and compute a global model from satellite observations is explained in detail.

The CHAMP mission has been launched in 2000. It is the first dedicated gravity field mission to carry a GPS receiver in space. The main observables are the observations from the GPS satellites to CHAMP, the so-called satellite-to-satellite tracking (SST). A gravity field model is computed with the Energy Balance Approach using kinematic orbit positions. It is based on the law of energy conservation, which states, that the sum of potential and kinetic energy is constant in a conservative force field. The kinetic energy is computed from the orbit positions via the orbit velocities. The unknown energy constant can be estimated which allows for the computation of the potential. The satellite is subject to non-conservative forces which are corrected for. These forces are partly measured by the onboard accelerometer and partly computed by models. The spherical harmonic coefficients are then derived from the potential values along the orbit in a least squares adjustment. The solution is validated using GPS-leveling data and compared to other global gravity field solutions.

The GOCE mission is scheduled for launch in early 2009. It is the first gravity gradiometer in space. The bandlimited satellite gravity gradiometry (SGG) observations are supported by SST. Due to the complexity of the mission and the data processing final results will only be available several weeks after the end of the mission. As there is a need for an analysis of the data in parallel to the mission, a quick-look gravity field analysis has been developed and implemented. It uses the semi-analytical approach which is based on the simplifying assumption of a circular orbit. This simplification allows to set up normal equations using fast Fourier transform (FFT) techniques. The normal equation matrix becomes block-diagonal and the least squares adjustment can be solved very efficiently. The gain in speed comes at the cost of accuracy. The method can be divided in two sub-approaches: the 1D-FFT approach and the 2D-FFT or (torus-) approach. Both approaches are applied to real CHAMP data and simulated GOCE data in order to asses their possibilities and limitations.

Contents

1 Introduction

In the period between 2000 and 2010 three dedicated gravity missions CHAMP, GRACE and GOCE have been or will be launched. They will improve global gravity models by several orders of magnitude. They benefit from the possibility of continuous and precise orbit determination with onboard GPS receivers and the development of highly accurate accelerometers. Combined with terrestrial, airborne and seaborne gravity observations, which are available in some regions with higher resolution but lack global coverage, they will form a new generation of gravity field models. However the global gravity field analysis poses challenges as the computation of global gravity field models poses high requirements to computer resources.

The purpose of this work is to describe gravity field analysis from CHAMP and GOCE in detail. As the GOCE mission has not yet been launched, only simulation data is available to prepare the processing software. Hence real data from the CHAMP mission is used here to get a more realistic insight into possible error sources for satellite data. The necessary theoretical background to compute a global model from satellite observations is explained in detail.

A brief description of the satellites and their instrumentation is given below.

CHAMP: The Challenging Minisatellite Payload (CHAMP) (cf. Reigber et al. (1998)) was launched in 2000. It was initiated by the GeoForschungsZentrum Potsdam (GFZ) and is operated by the German Aerospace Center (DLR). Although being a relatively economical mission, it has significantly improved the gravity field models for wavelengths above 550 km. Furthermore it has helped to test new technology which has since then been further developed and is used on GRACE and GOCE as well.

It is the first low Earth orbiter (LEO) dedicated to gravity field analysis with a GPS receiver on board. This allows for a continuous and accurate orbit tracking, referred to as high-low satellite-to-satellite tracking (hl-SST). The GPS-observations are the main observable of the mission. The orbit can be related to the gravity field as shown in chapter 2 and used for gravity field analysis. The GPS receiver is complemented by an accelerometer which measures all non-gravitational forces acting on the satellite and by a star tracker which determines the orientation of the satellite in space. The orientation is needed for the rotation of the measured accelerations to the reference frame in which the orbits are given. The accelerations are used to correct the observations for non-gravitational effects.

In addition to gravity field determination, the CHAMP satellite has two further scientific goals: first it is equipped with two magnetometers for the determination of the Earth magnetic field, and second with GPS receivers for atmosphere sounding by the method of radio occultation.

GRACE: The Gravity Recovery and Climate Experiment (GRACE) (cf. Tapley and Reigber (2001)) was launched in 2002 and is operated by the National American Space Agency (NASA), the German Aerospace Center (DLR), the University of Texas, Center for Space Research (CSR) and the GeoForschungsZentrum Potsdam (GFZ).

The mission consists of two almost identical satellites, which follow each other on the same orbit in about 220 km distance. They are connected via a K-band microwave link which measures their distance with high accuracy at the μm-level. This measurement technique called low-low satellite-to-satellite tracking (ll-SST) allows for a much higher gravity resolution than hl-SST, and gravity field models for wavelengths down to 300 km could be determined. Due to the high accuracy and the continuous

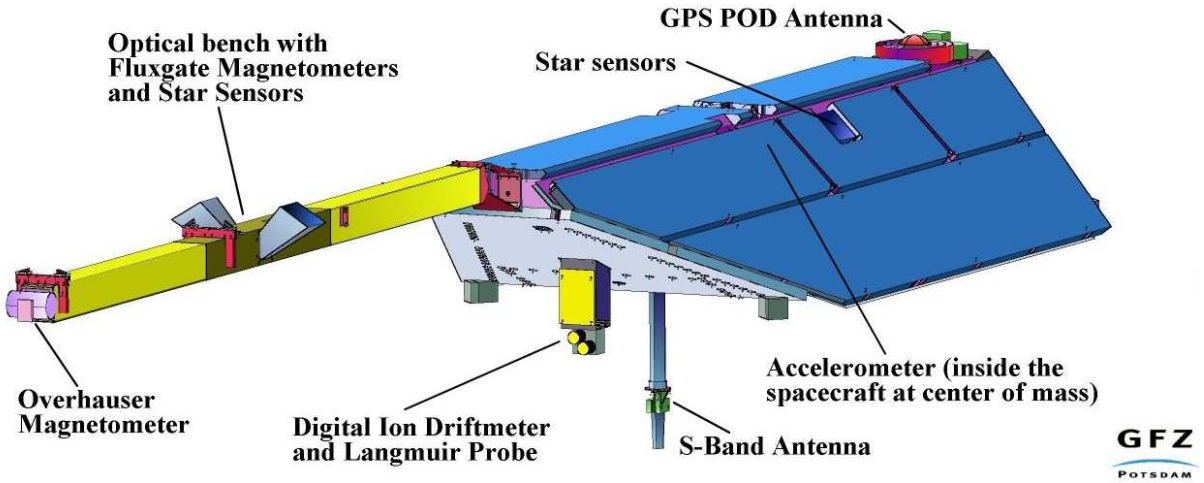

Figure 1.1: The CHAMP satellite and its instruments (source: GFZ Potsdam).

tracking over several years, temporal variations of the gravity field caused by large scale mass-variations (e.g. seasonal hydrological effects or melting of ice masses) can be detected. As shown in figure 1.2, the design of the GRACE satellites is similar to the CHAMP satellite. They contain a GPS receiver, an accelerometer and star tracker cameras. In addition, each of the GRACE satellites carries a K-band horn directed at the other satellite, which is the main instrument of the mission.

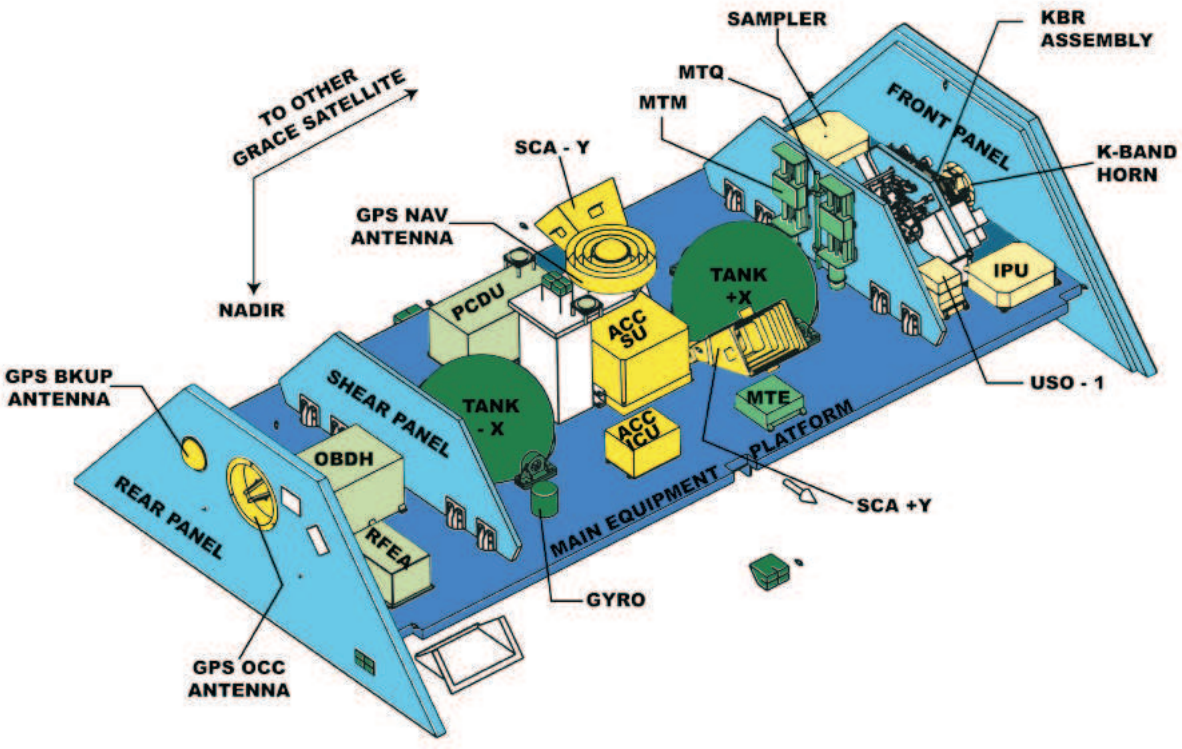

Figure 1.2: One of the GRACE satellites and its instruments (source: Astrium).

The GRACE mission is not subject of this work, but it is mentioned here as it complements the other missions. It is focused on the determination of temporal variations of the gravity field, while GOCE will determine the static part with high resolution and accuracy.

GOCE: The Gravity field and steady-state Ocean Circulation Explorer (GOCE) (cf. ESA (1999)) is scheduled for launch in early 2009. It has been selected as the first Earth Explorer Core Mission

of ESA's Living Planet Programme. It will combine hl-SST with a new measurement type: satellite gravity gradiometry (SGG). The GOCE mission will be the first to fly a gradiometer in space.

The gradiometer will consist of six accelerometers, similar to those of CHAMP and GRACE, but with an increased accuracy (see tab. 1.1). They will be arranged pairwise along the three axes of the satellite and symmetric to the satellite's center of mass (see fig. 2.5). The x-axis will nominally point in flight direction, the z-axis radially outward and the y-axis will complement an orthogonal right-hand triad. By differential measurements between the pairs of accelerometers it is possible to derive the matrix of second derivatives of the gravity potential field (see sec. 2.3). Second derivatives measured along the orbit with low altitude allow for a global gravity field solution with higher resolution than for CHAMP and GRACE. Wavelengths down to 100 km will be resolved.

Due to the limited measurement bandwidth of the gradiometer from 5 - 100 mHz, wavelengths roughly above 1500 km cannot be resolved by SGG and have to be derived from hl-SST observations measured by the onboard GPS receiver. Similar to CHAMP and GRACE, the GOCE-satellite is equipped with star trackers to determine the orientation of the satellite and the gradiometer in space.

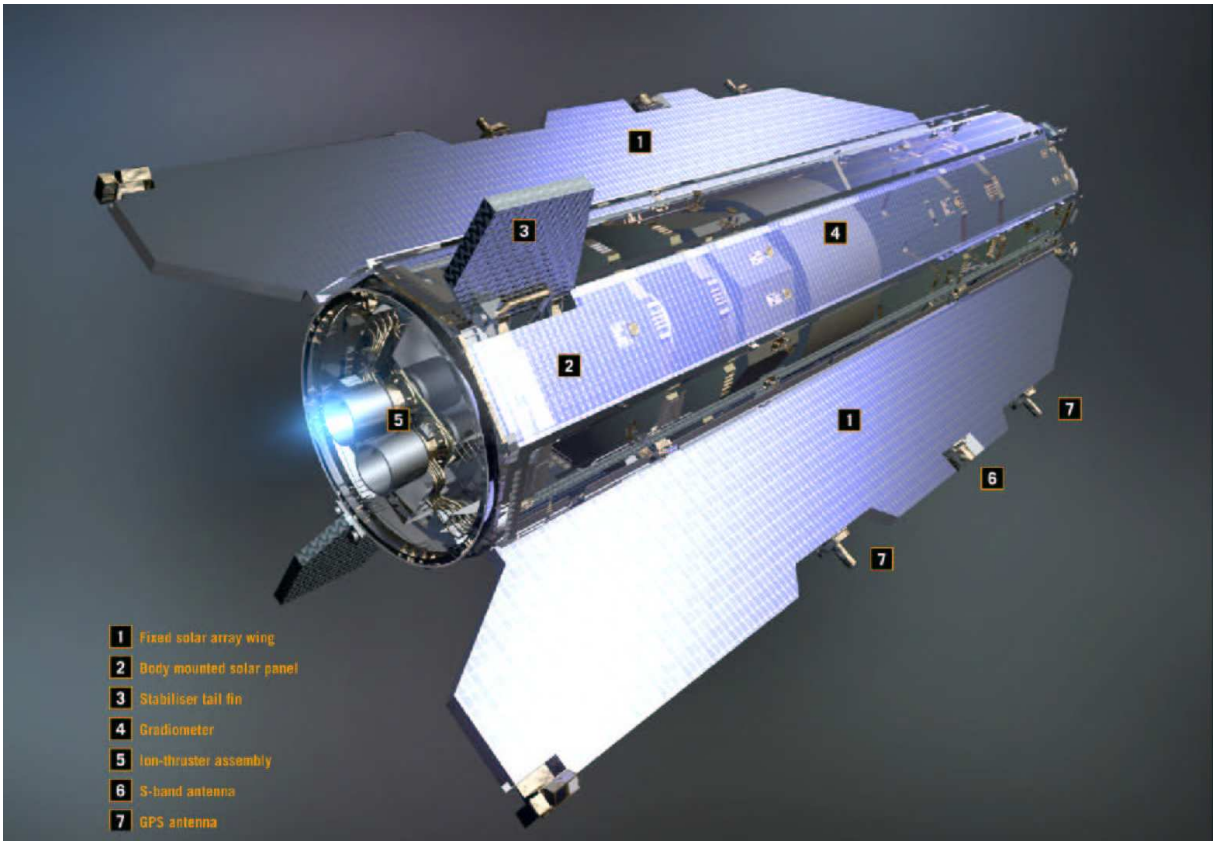

Figure 1.3: The GOCE satellite and its instruments (source ESA).

Several features of the GOCE mission design pose special challenges to the gravity field analysis. They will be discussed in section 4.1. In order to increase the sensitivity, the satellite will fly at the low altitude of about 250 km. At this altitude, there is considerable air drag from the Earth's atmosphere. The air drag has to be compensated by thrusters in order to keep the satellite in orbit. At the same time this removes external accelerations acting on the satellite to a large extent. The range of the observed accelerations becomes smaller and the sensitivity of the gradiometer to small differences in gravity is increased. This is done by the drag-free and attitude control system (DFACS). It only compensates drag within the measurement bandwidth allowing small long-term variations in orbit height (see fig 4.9). Fuel consumption of the continuous drag compensation limits the mission duration to two years at most.

In order to provide a continuous power supply, the solar panels of the satellite will always point in

direction of the sun and a sun-synchronous orbit is required. This is achieved by by choosing the orbit parameters such, that the precession of the orbital plane caused by the oblateness of the Earth will perform exactly one revolution per year. At an orbit altitude of about 250 km, an inclination of 96.6° is required. The non polar orbit leaves two small polar gaps which are not covered with observations. This leads to an ill-posed system of equations in the gravity field determination process(cf. sec. 4.1). In addition, due to the orbit design, the satellite will experience seasons of eclipses, where it will enter the Earth's shadow during each revolution. The power supply is interrupted during those eclipses and the satellite brought into a hibernation mode. The mission profile is divided into two or three observation phases of about six months.

The spacecraft attitude is controlled by three orthogonal magnetic torquers. They are coils which use the magnetic field of the Earth to induce a torque on the satellite. As only forces can be induced which are perpendicular to the lines of magnetic flux, the satellite cannot be rotated around all three axes at any given time. If the satellite is for example crossing the polar region, where the lines of magnetic flux are almost pointing in radial (z-) direction, no torque around the z-axis can be induced. As a consequence, the attitude of the satellite will deviate by up to 3° from the nominal attitude in flight direction. The implications of this deviation will be discussed in section 4.1.

	CHAMP	GRACE	GOCE
launch date	2000	2002	2009
number of satellites	1	2	1
orbit altitude	450-350 km	450-300 km	250 km
weight	400 kg	432 kg	250 km
orbit inclination	87.3°	89.5°	96.6°
accelerometer accuracy (sensitive axes in MBW)	$3 \cdot 10^{-9}\,\mathrm{m/s^2}$	$1 \cdot 10^{-10}\,\mathrm{m/s^2}$	$1 \cdot 10^{-12}\,\mathrm{m/s^2}$

Table 1.1: Comparison of the CHAMP, GRACE and GOCE satellite missions.

Accelerometers: The accelerometers are among the core instruments of all three missions. The GOCE gradiometer is composed by six of them. Although having different accuracies (cf. table 1.1), they are all based on the same principle. A proof mass is kept levitating in an electric field inside a cage of electrodes. If external forces act on the satellite the proof mass has the tendency to move inside the cage due to inertia. Any motion or rotation of the proof mass will be detected by a capacitive sensor, as the capacity between the electrodes will change. The voltage applied to the electrodes will be immediately corrected by a so-called force feedback system in order to keep the proof mass in its original location. The voltage which is necessary to keep the proof mass in place is the actual observation and can be converted to acceleration by a transfer function.

The accelerometers all have only two highly sensitive axes and one less sensitive axes. During the calibration before launch one axis cannot be calibrated with the highest sensitivity as the gravitational force of the Earth has to be compensated. For CHAMP this axis will point radially outward, for GRACE in cross-track direction. The six accelerometers forming the GOCE gradiometer are aligned such (see fig. 2.5), that only the less important xy- and yz-components of the gravity tensor will have degraded accuracy. A view of the proof-masses and electrodes of an accelerometer are shown in figure 1.4. A drawing of the assembled gradiometer in a thermic cage is shown in figure 1.5.

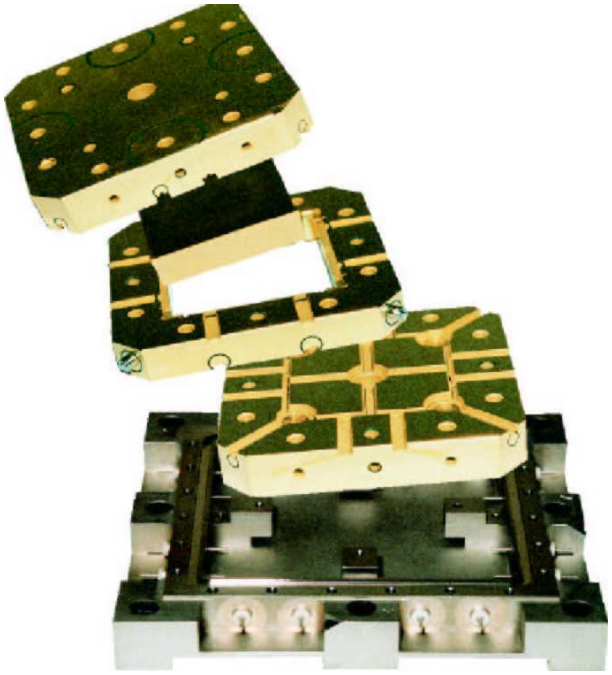

Figure 1.4: Test mass and electrodes of one accelerometer (source: ESA).

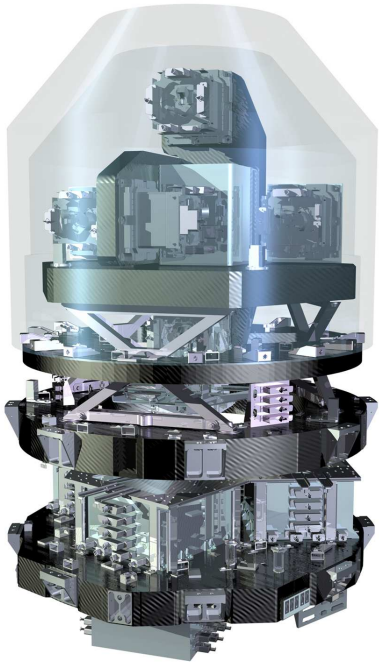

Figure 1.5: GOCE-gradiometer with double-layered thermic cage (source: ESA).

2 Theory of Gravity Field Analysis From Satellite Measurements

The goal of global gravity field analysis is to derive a potential model expressed in spherical harmonic coefficients on the Earth's surface from measurements along the satellite orbit. The analysis can be divided in two steps. For both steps several alternative methods have been developed which are displayed in figure 2.1. The theory for some of these methods (the ones in green boxes) is explained in detail in this chapter. In the first step a linear relation between the observations and functionals of the potential is derived. In case of high-low satellite-to-satellite tracking (hl SST) the main observation is the GPS tracking from a low-Earth-orbiting (LEO) satellite. They can be transformed via orbit positions and velocities to potential values along the orbit with the Energy Balance Approach (see sec. 2.2). Satellite Gravity Gradiometry (SGG) observes components of the tensor of second derivatives of the gravity potential in the satellite fixed coordinate frame. They are already functionals of the potential and do not need to be linearized. Nevertheless they are subject to several data processing steps and a frame transformation which are explained in section 2.3. In the second step the point values along the orbit have to be transformed into a global model on the Earth's surface. This is the solution of an over-determined and ill-posed system of equations. The Direct Solution shown in section 2.4 is a strict least-squares adjustment. As this often poses large requirements on computer resources, several iterative solution strategies have been developed and one of them, the semi-analytic Approach is presented in section 2.5. The connection between both steps is the series expansion of the potential and its derivatives which is derived in section 2.1.

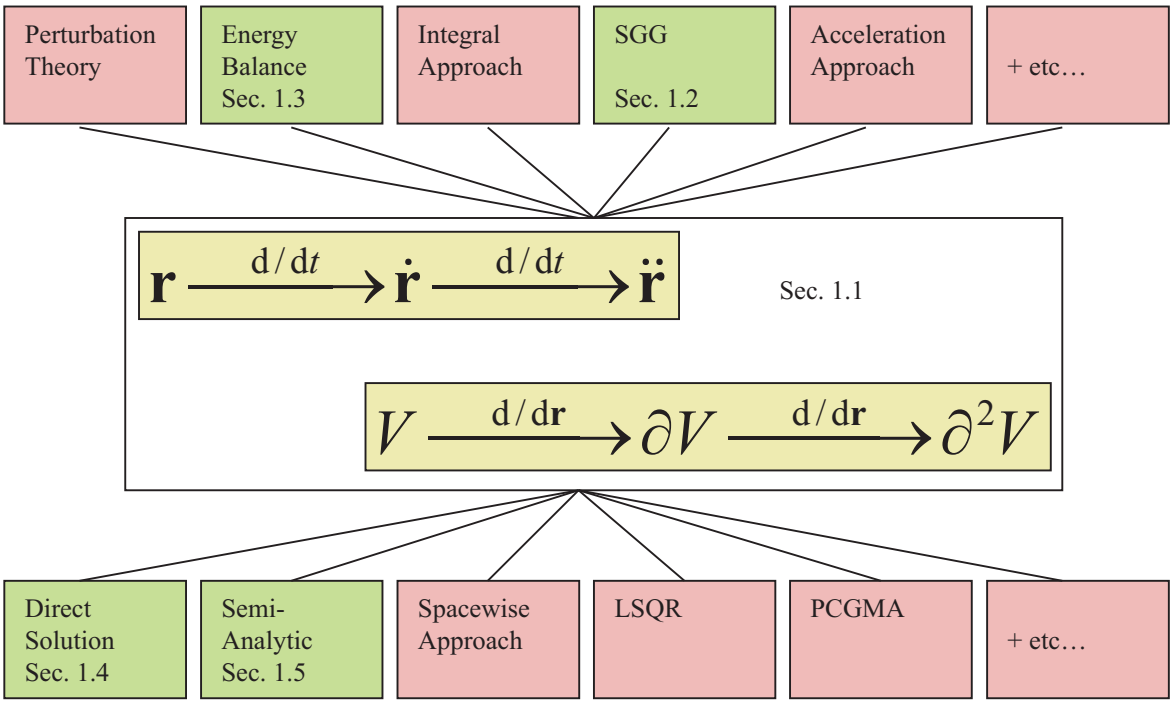

Figure 2.1: Overview of gravity field analysis methods for CHAMP, GRACE, and GOCE. The methods in green are subject of this thesis.

Most of the methods for gravity field analysis from satellite orbits in use were already derived about 40 years ago, but they only became feasible with the continuous GPS tracking on the CHAMP and

GRACE satellites. The methods in the red boxes of figure 2.1 are not subject of this work but are mentioned for completeness. The classical approach of gravity field analysis from satellite orbits is derived from perturbation theory (e.g. Kaula (1966)). The energy balance approach (e.g. Reigber (1969)) which is used to derive potential values from the CHAMP and GOCE orbits in this work can as well be applied to derive potential differences between the two GRACE satellites (cf. Jekeli (1999)). The integral equation approach (e.g. Schneider (1968), Reigber (1969)) has been successfully applied to CHAMP and GRACE data and produced good results (cf. Mayer-Gürr (2006)). Differentiating the CHAMP orbit twice leads to accelerations, which are a functional of the gravity field (Austen and Reubelt (2000)). This method can be applied to the GRACE satellites as well, leading to a one axis gradiometer in space (Sharifi and Keller (2005)).

Apart from the direct least-squares solution and the semi-analytic approach (e.g. Sneeuw (2000)), which are discussed in this work, there are several alternative iterative approaches for the solution of potential coefficients from satellite observations, like the spacewise approach (e.g. Migliaccio (2004)), a least squares method based on a QR factorization (LSQR) (e.g. Baur (2007)) and the preconditioned conjugate gradient multiple adjustment approach (PCGMA) (cf. Schuh (1996)).

2.1 The Gravity Field and its Derivatives

2.1.1 Solution of the First Geodetic Boundary Value Problem

The gravitational potential is a harmonic function outside the gravitating masses, which is expressed by the Laplace equation:

$$\Delta V = \nabla^2 V = \frac{\partial^2 V}{\partial x^2} + \frac{\partial^2 V}{\partial y^2} + \frac{\partial^2 V}{\partial z^2} = 0 \quad . \tag{2.1}$$

This equation can also be written as

$$\Delta V = r^2 \frac{\partial^2 V}{\partial r^2} + 2r \frac{\partial V}{\partial r} + \frac{\partial^2 V}{\partial \theta^2} + \cot\theta \frac{\partial V}{\partial \theta} + \frac{1}{\sin^2\theta} \frac{\partial^2 V}{\partial \lambda^2} = 0 \tag{2.2}$$

in spherical coordinates (θ, λ, r), where $\theta = 90° - \phi$ denotes the so-called co-latitude, λ the longitude and r the geocentric distance. This partial differential equation can be solved by a separation approach, which separates the three arguments in different terms. So each of the terms must be constant and the partial differential equation can be solved as three second-order ordinary differential equations (cf. Kaula (1966)):

$$\begin{aligned} V(\theta,\lambda,r) = &\sum_{l}^{\infty} r^{-(l+1)} \sum_{m}^{l} P_{lm}(\cos\theta) \left[a_{lm}\cos m\lambda + b_{lm} \ \sin m\lambda\right] \\ &+ \sum_{l}^{\infty} r^{l} \sum_{m}^{l} P_{lm}(\cos\theta) \left[a'_{lm}\cos m\lambda + b'_{lm} \ \sin m\lambda\right] , \end{aligned} \tag{2.3}$$

with a_{lm}, b_{lm}, a'_{lm} and b'_{lm} as constant coefficients, and the associated Legendre functions $P_{lm}(\cos\theta)$:

$$P_{lm}(\cos\theta) = \frac{1}{2^l l!}(1-\cos^2\theta)^{m/2} \frac{\mathrm{d}^{l+m}(\cos^2\theta - 1)^l}{\mathrm{d}(\cos\theta)^{l+m}} \quad . \tag{2.4}$$

The coefficients are determined by means of two boundary conditions:

$$\lim_{r\to\infty} V(\theta,\lambda,r) = 0 \tag{2.5}$$

$$V(\theta,\lambda,r=R) = f(\theta,\lambda)\ . \tag{2.6}$$

Condition (2.5) leads to $a'_{lm} = 0$ and $b'_{lm} = 0$. Condition (2.6) is resolved by a coefficient comparison between the coefficients of the new solution A_{lm} and B_{lm} and the coefficients of the boundary function:

$$A_{lm} = R^{-(l+1)}a_{lm} \quad \text{and} \quad B_{lm} = R^{-(l+1)}b_{lm} \quad . \tag{2.7}$$

The coefficients A_{lm} and B_{lm} have the same unit as the potential $\left[\frac{\mathrm{m}^2}{\mathrm{s}^2}\right]$. Therefore a second substitution yields then dimensionless coefficients

$$C_{lm} = \frac{R}{GM}A_{lm} \quad \text{and} \quad S_{lm} = \frac{R}{GM}B_{lm} \quad . \tag{2.8}$$

For numerical reasons it is suitable to use the normalized associated Legendre functions $\bar{P}_{lm}(\cos\theta) = H_{lm}P_{lm}(\cos\theta)$. Hence a third substitution is applied:

$$\bar{C}_{lm} = H_{lm}^{-1}C_{lm} \quad \text{and} \quad \bar{S}_{lm} = H_{lm}^{-1}S_{lm} \quad , \tag{2.9}$$

where

$$H_{lm} = \begin{cases} \sqrt{2l+1} & \text{for} \quad m = 0 \\ \sqrt{2(2l+1)\frac{(l-m)!}{(l+m)!}} & \text{for} \quad m \neq 0 \end{cases} \quad . \tag{2.10}$$

Finally the gravitational potential on the Earth's surface and in the outer space reads as:

$$V(\theta,\lambda,r) = \frac{GM}{R}\sum_{l=0}^{\infty}\left(\frac{R}{r}\right)^{l+1}\sum_{m=0}^{l}\bar{P}_{lm}(\cos\theta)\left[\bar{C}_{lm}\cos m\lambda + \bar{S}_{lm}\sin m\lambda\right] \quad . \tag{2.11}$$

$\bar{C}_{lm}$ and $\bar{S}_{lm}$ are the potential coefficients, which are used to describe a gravity potential model. If r is constant, the potential becomes a function on a spherical surface (e.g the Earth's sphere for $r = R$). Equation (2.11) corresponds to a two-dimensional Fourier series on a spherical surface. The function is periodic in the direction of the longitude λ and the base functions are sines and cosines. In the direction of the co-latitude θ the function is aperiodic and the argument θ runs from 0 to π with the $\bar{P}_{lm}(\cos\theta)$ as base functions. Both sets of base functions together form an infinite set of orthogonal functions and are ordered by degree l and order m. As in practise the series expansion cannot be calculated to infinity, one has to truncate the computation at a maximum degree L, inducing an omission error. As $m \leq l$ and all $\bar{S}_{l0}$ - coefficients can be neglected because of $\sin(0\lambda) = 0$, the number of coefficients is $(L+1)^2$. The closed analytical form of the Legendre functions given in equation (2.4) is unsuitable for numerical computations. The functions and their derivatives can be easily computed by a recurrence relation (see A.2.1).

2.1.2 First and Second Order Derivatives

The potential and its first and second order derivatives w.r.t. the spherical coordinates (r, θ, λ) can be expressed in a similar way by substituting the symbols λ_{ij}, p, α and β with the corresponding expression from table 2.1:

$$V_{ij} = \frac{GM}{R} \sum_{l=0}^{l_{\max}} \lambda_{ij} \left(\frac{R}{r}\right)^{(l+1)} \sum_{m=0}^{l} p \left(\alpha \cos(m\lambda) + \beta \sin(m\lambda)\right) . \tag{2.12}$$

differentiation w.r.t.	λ_{ij}	p	α	β
-	1	$\bar{P}_{lm}$	$\bar{C}_{lm}$	$\bar{S}_{lm}$
r	$-\frac{(l+1)}{r}$	$\bar{P}_{lm}$	$\bar{C}_{lm}$	$\bar{S}_{lm}$
θ	1	$\bar{P'}_{lm}$	$\bar{C}_{lm}$	$\bar{S}_{lm}$
λ	1	$m\bar{P}_{lm}$	$\bar{S}_{lm}$	$-\bar{C}_{lm}$
rr	$\frac{(l+1)(l+2)}{r^2}$	$\bar{P}_{lm}$	$\bar{C}_{lm}$	$\bar{S}_{lm}$
$r\theta$	$-\frac{(l+1)}{r}$	$\bar{P'}_{lm}$	$\bar{C}_{lm}$	$\bar{S}_{lm}$
$r\lambda$	$-\frac{(l+1)}{r}$	$m\bar{P}_{lm}$	$\bar{S}_{lm}$	$-\bar{C}_{lm}$
$\theta\theta$	1	$\bar{P''}_{lm}$	$\bar{C}_{lm}$	$\bar{S}_{lm}$
$\theta\lambda$	1	$m\bar{P'}_{lm}$	$\bar{S}_{lm}$	$-\bar{C}_{lm}$
$\lambda\lambda$	-1	$m^2\bar{P}_{lm}$	$\bar{C}_{lm}$	$\bar{S}_{lm}$

Table 2.1: Substitutes for the symbols λ_{ij}, p, α and β in equation (2.12).

Accelerations: To obtain the gravitational accelerations in cartesian coordinates in the Earth-fixed frame, the first order derivatives in spherical coordinates have to be transformed using the chain rule:

$$\ddot{x}_{\mathrm{e}} = \frac{\partial V}{\partial x} = \frac{\partial V}{\partial r}\frac{\partial r}{\partial x} + \frac{\partial V}{\partial \theta}\frac{\partial \theta}{\partial x} + \frac{\partial V}{\partial \lambda}\frac{\partial \lambda}{\partial x}, \tag{2.13a}$$

$$\ddot{y}_{\mathrm{e}} = \frac{\partial V}{\partial y} = \frac{\partial V}{\partial r}\frac{\partial r}{\partial y} + \frac{\partial V}{\partial \theta}\frac{\partial \theta}{\partial y} + \frac{\partial V}{\partial \lambda}\frac{\partial \lambda}{\partial y}, \tag{2.13b}$$

$$\ddot{z}_{\mathrm{e}} = \frac{\partial V}{\partial z} = \frac{\partial V}{\partial r}\frac{\partial r}{\partial z} + \frac{\partial V}{\partial \theta}\frac{\partial \theta}{\partial z} + \frac{\partial V}{\partial \lambda}\frac{\partial \lambda}{\partial z}, \tag{2.13c}$$

where the partial derivatives can be simply derived from geometry:

$$\partial r/\partial x = \sin\theta \cdot \cos\lambda \tag{2.14a}$$

$$\partial r/\partial y = \sin\theta \cdot \sin\lambda \tag{2.14b}$$

$$\partial r/\partial z = \cos\theta \tag{2.14c}$$

$$\partial \theta/\partial x = \cos\theta \cdot \cos\lambda/r \tag{2.14d}$$

$$\partial \theta/\partial y = \cos\theta \cdot \sin\lambda/r \tag{2.14e}$$

$$\partial \theta/\partial z = -\sin\theta/r \tag{2.14f}$$

$$\partial \lambda/\partial x = -\sin\lambda/(r \cdot \sin\theta) \tag{2.14g}$$

$$\partial \lambda/\partial y = \cos\lambda/(r \cdot \sin\theta) \tag{2.14h}$$

$$\partial \lambda/\partial z = 0. \tag{2.14i}$$

Gravity Tensor: Similarly, the Gravity Tensor can be transformed to cartesian coordinates. As it is normally required in an orbit-related frame, it is first computed in a topocentric auxiliary frame (often referred to as local north-oriented frame (LNOF)), with the z-axis pointing radially away from the Earth's center, the x-axis pointing north, and the y-axis pointing east. It can then be rotated to the frame of interest, e.g. a local orbit reference frame (LORF), which is oriented along the nominal orbit or the gradiometer reference frame (GRF) which represents the actual orientation of the satellite and the gradiometer (cf. section 2.3). For convenience V_{ij} is written for $\frac{\partial^2 V}{\partial i \partial j}$, the components in LNOF are:

$$V_{xx} = \frac{1}{r}V_r + \frac{1}{r^2}V_{\theta\theta} \tag{2.15a}$$

$$V_{xy} = \frac{\cos\theta}{r^2 \sin^2\theta}V_\lambda - \frac{1}{r^2 \sin\theta}V_{\lambda\theta} \tag{2.15b}$$

$$V_{xz} = \frac{1}{r^2}V_\theta - \frac{1}{r}V_{r\theta} \tag{2.15c}$$

$$V_{yy} = \frac{1}{r}V_r + \frac{1}{r^2 \tan\theta}V_\theta + \frac{1}{r^2 \sin^2\theta}V_{\lambda\lambda} \tag{2.15d}$$

$$V_{yz} = \frac{1}{r \sin\theta}V_{r\lambda} - \frac{1}{r^2 \sin\theta}V_\lambda \tag{2.15e}$$

$$V_{xx} = V_{rr} \tag{2.15f}$$

2.1.3 The Potential in Orbital Coordinates

Equation (2.11) is often referred to as "Space-Wise" representation of the gravity field. Alternatively it is expressed as function of Keplerian elements along the orbit. This was first introduced by Kaula (1966) and modified by Sneeuw (2000), and is referred to as "Time-Wise" representation:

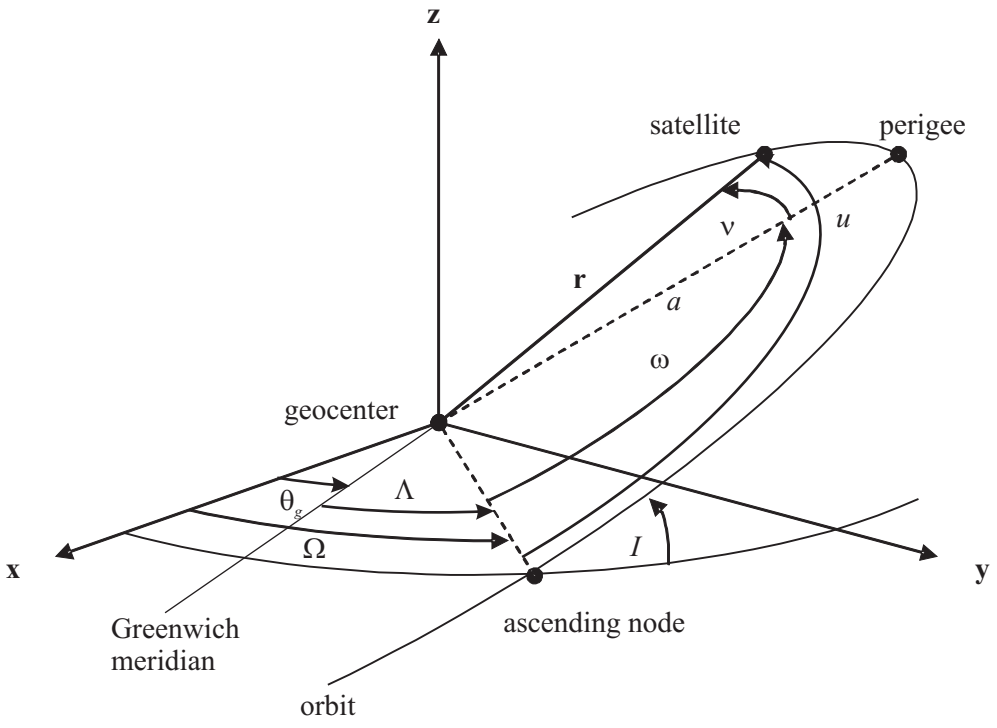

Figure 2.2: Orbit elements.

$$V(r,I,u,\Lambda) = \frac{GM}{R}\sum_{l=0}^{\infty}\left(\frac{R}{r}\right)^{l+1}\sum_{m=0}^{l}\sum_{k=-l,2}^{l}\bar{F}_{lmk}(I)$$
$$[\alpha_{lm}\cos(ku+m\Lambda)+\beta_{lm}\ \sin(ku+m\Lambda)] \quad , \tag{2.16}$$

with

$$\alpha_{lm} = \left[\begin{array}{c}\bar{C}_{lm}\\ -\bar{S}_{lm}\end{array}\right]_{l-m=\text{odd}}^{l-m=\text{even}} \quad \text{and} \quad \beta_{lm} = \left[\begin{array}{c}\bar{S}_{lm}\\ \bar{C}_{lm}\end{array}\right]_{l-m=\text{odd}}^{l-m=\text{even}} \quad . \tag{2.17}$$

The Keplerian elements I, Ω and ω shown in figure 2.2 define the orbital plane. The inclination I is the angle between the orbit plane and the equatorial plane. The angle ω defines the perigee of the ellipse and Ω the right ascension of the ascending node. The true anomaly is the angle between the direction of the perigee and the current position of the satellite. The Greenwich apparent sidereal time (GAST) or Greenwich hour angle is denoted by θ_g.

The expression above only holds for circular orbits. As the perigee in an almost circular orbit is not well defined, the *argument of latitude* $u = \omega + \nu$ is introduced as the sum of the perigee and the true anomaly. In addition the substitution $\Lambda = \Omega - \theta_g$ is made in order to relate the ascending node to the Greenwich meridian and the Earth-fixed frame.

The $\bar{F}_{lmk}(I)$ are called *Inclination Functions*, and the $\bar{F}^*_{lmk}(I)$ *Cross-track Inclination Functions*, which occur by differentiation of the potential in cross-track direction. For their computation cf. Kaula (1966) or Sneeuw (1991); an efficient algorithm is given in A.2.2. The first and second derivatives of the potential are derived in Sneeuw (2000) and can be written in analogy to equation (2.12):

$$V_{ij} = \frac{GM}{R}\sum_{l=0}^{\infty}\left(\frac{R}{r}\right)^{l+1}\sum_{m=0}^{l}\sum_{k}\lambda_{ij} f\,(a\cos(\psi_{mk})+b\sin(\psi_{mk})) \quad , \tag{2.18}$$

with $\psi_{mk} = ku + m\Lambda$. The expressions for λ_{ij}, f, a and b are given in Table 2.2.

differentiation w.r.t.	λ_{ij}	f	a	b
-	1	$\bar{F}_{lmk}(I)$	α_{lm}	β_{lm}
x	$\frac{k}{r}$	$\bar{F}_{lmk}(I)$	β_{lm}	$-\alpha_{lm}$
y	$\frac{1}{r}$	$\bar{F}^*_{lmk}(I)$	α_{lm}	β_{lm}
z	$\frac{-(l+1)}{r}$	$\bar{F}_{lmk}(I)$	α_{lm}	β_{lm}
xx	$\frac{-(k^2+l+1)}{r^2}$	$\bar{F}_{lmk}(I)$	α_{lm}	β_{lm}
yy	$\frac{k^2-(l+1)^2}{r^2}$	$\bar{F}_{lmk}(I)$	α_{lm}	β_{lm}
zz	$\frac{(l+1)(l+2)}{r^2}$	$\bar{F}_{lmk}(I)$	α_{lm}	β_{lm}
xy	$\frac{k}{r^2}$	$\bar{F}^*_{lmk}(I)$	β_{lm}	$-\alpha_{lm}$
xz	$\frac{-k(l+2)}{r^2}$	$\bar{F}_{lmk}(I)$	β_{lm}	$-\alpha_{lm}$
yz	$\frac{-(l+2)}{r^2}$	$\bar{F}^*_{lmk}(I)$	α_{lm}	β_{lm}

Table 2.2: Expressions for the symbols λ_{ij}, f, a and b in equation 2.18

2.2 The Energy Balance Approach

The main observable of hl-SST is the GPS tracking of the LEO, which is used to determine the orbit of the satellite. Because there is no linear relation of the orbit to the spherical harmonic gravity field coefficients, the observation equations have to be linearized. The Energy Balance Approach is a method to derive a time series of disturbing potential values from the satellite orbit based on the Law of Energy Conservation. The law states, that in a conservative force field, the sum of kinetic and potential energy of a body is constant:

$$W_{\text{kin}} + W_{\text{pot}} = \frac{1}{2} m \dot{\mathbf{r}}^2 - mV = H \ , \tag{2.19}$$

where H is the Hamiltonian – the constant total energy in the system. This equation creates a relation between the observed orbit, expressed by the position vector $\mathbf{r}$ (resp. its time derivative $\dot{\mathbf{r}}$) and the gravity potential V. It should be noted that the sign of the potential changes, as potential and potential energy are defined with opposite signs in physics (as used in equ. (2.19)) and geodesy (as defined by equ. (2.5)).

As the orbit positions do not enter the computation directly – but their first time-derivatives, the components of $\dot{\mathbf{r}}$ – their derivation is essential for the method and discussed in detail in section 2.2.1. The Law of Energy Conservation is valid for a conservative potential field in an inertial frame. Both conditions are not fulfilled as the Earth's gravity potential field is rotating and the satellite is affected by non-conservative forces. It will be shown in section 2.2.2 how those effects have to be taken into account. For this purpose two equivalent representations for the computation of the disturbing potential – in the inertial frame and in the Earth-fixed frame – are presented. Finally in section 2.2.3 a consistent error model is derived by error propagation for all processing steps.

2.2.1 Velocity Determination

As the squared velocities enter into the computation – and so do their errors – they play a central role in the Energy Balance Approach, and the determination of orbits and velocities has to be considered thoroughly. Precise orbit determination (POD) is not part of this work (for details cf. Švehla and Rothacher (2004)), but a short overview of orbit determination methods is given in order to put the velocity determination into context.

The classic orbit determination method is *dynamic POD*. It is based on the integration of accelerations (or more precisely specific forces acting on the satellite) which are computed from physical models (e.g. gravity model, atmospheric drag model, solar radiation pressure model etc.). Various parameters like the initial state vector or improvements to the employed physical models are estimated in a least-squares adjustment using the GPS-tracking as observations. This orbit determination method is closely related to the classical method for gravity field analysis, as it is possible to solve – among other model parameters – for the gravity field coefficients. The orbit velocities are a by-product of the orbit integration.

Due to the deficiencies of physical models, the dynamic orbits deviate from the measurements already after a short period of time. In order to improve orbit determination the *reduced dynamic POD* was developed (cf. Yunck et. al (1990) and Wu et al. (1991)). The deterministic model of the dynamic POD is extended by statistical parameters. This gives the integrated orbit more degrees of freedom for a better fit to the data. The resulting orbits have a high accuracy, are very smooth and are less affected by short data gaps, as the orbit integration smoothes measurement noise and bridges data gaps. However the velocities are strongly correlated with the employed models (especially the a priori gravity model), as they are basically obtained by the integration of accelerations determined by these models. It has been shown by Gerlach et al. (2003a) that no significant improvement of the a priori gravity model can be achieved by the Energy Balance Approach using reduced dynamic orbits.

In contrast to the model based methods *kinematic POD* was developed. It is a geometric technique which is purely based on observations (mainly GPS) and uses no a priory models to describe the motion of the satellite. Thus the orbits are better suited to be used with the Energy Balance Approach. Nevertheless they have some disadvantages: they contain more high frequency errors and more data-gaps than reduced dynamic orbits. As each point is computed independently using only the observations of the given epoch, kinematic POD can not provide velocities. Thus velocities have to be derived by numerical differentiation.

Numerical differentiation has the disadvantage that high frequency errors are amplified, which is shown by a spectral analysis of the orbit and its errors: in figure 2.3 the blue curve shows the power spectral density (PSD) of a typical LEO orbit (which was obtained by the simulation of 1 week at 375 km orbit height with 1 s sampling, using only gravitational forces), and the red curve shows the PSD of a white noise orbit error with σ_0 of 1.5 cm, which is a typical error for LEOs (although in reality it is not exactly white). Figure 2.4 shows the PDSs for the derivatives of signal and noise of figure 2.3, namely the velocities (blue curve) and their errors (red curve). The dominant frequency in both the orbit and the velocities (blue curves), is the orbit frequency of $\sim 1.81 \cdot 10^{-4}$ Hz (which corresponds to a revolution period of ~ 5523 s) and its multiples. The signal power decreases towards the higher frequencies. It can be recognized, that the error PSD of the orbit, which is constant over the whole spectrum (fig. 2.3) is amplified proportional to the frequency, which amplifies the high frequent errors w.r.t. the velocity signal. In fact the time derivative in the time domain corresponds to a multiplication of the spectrum with $i\omega$, where ω denotes the angular velocity $\omega = 2\pi f$. The observed signal is the sum of both – signal and error. The signal to noise ratio becomes 1 at the intersection of the curves ($\approx 1.29 \cdot 10^{-2}$ Hz in this example). All higher frequencies should be filtered out with a low-pass filter as there the noise dominates the signal. In section A.1 several numerical differentiation methods are derived which also can be considered as filters. The choice of the optimal differentiation method depends on mission parameters like orbit height, sampling interval and the orbit error and will be discussed using real CHAMP data in section 3.1.

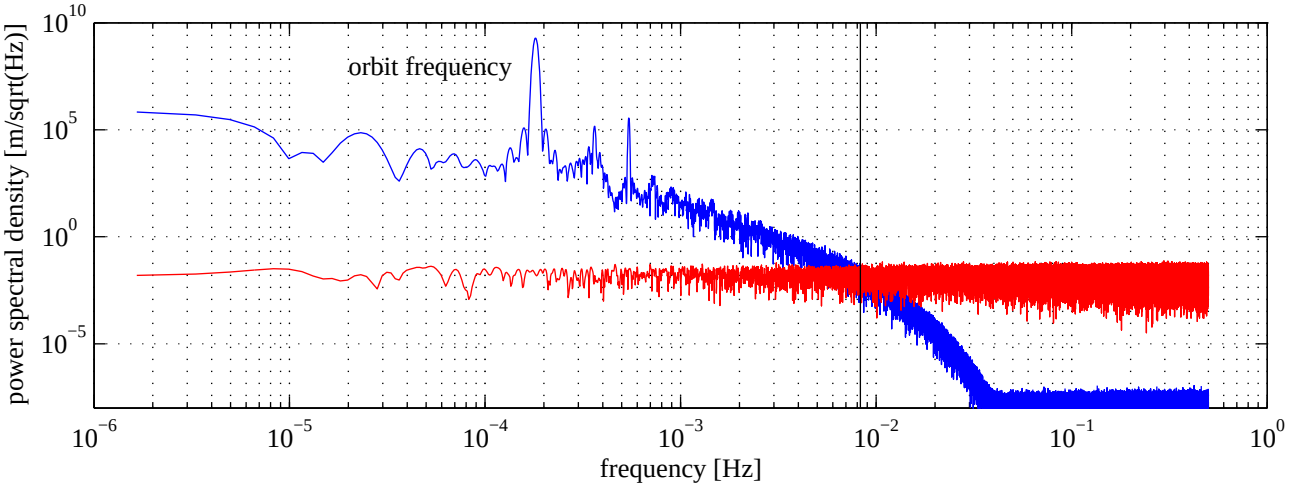

Figure 2.3: Power spectral density of orbit signal and errors.

2.2.2 Energy Integral

The Law of Energy Conservation is valid for a conservative field in an inertial system. As the Earth's potential field is rotating one can either compute it in the Earth-fixed frame and has to account for the rotation of the frame, or one can compute it in an inertial system and has to account for the rotation of the potential. Both alternatives are equivalent and can be derived by an integration of the equation of motion. In addition the satellite is subject to non-conservative forces, which have to be corrected for. This problem is connected to the frame rotation problem, as these corrections are treated differently

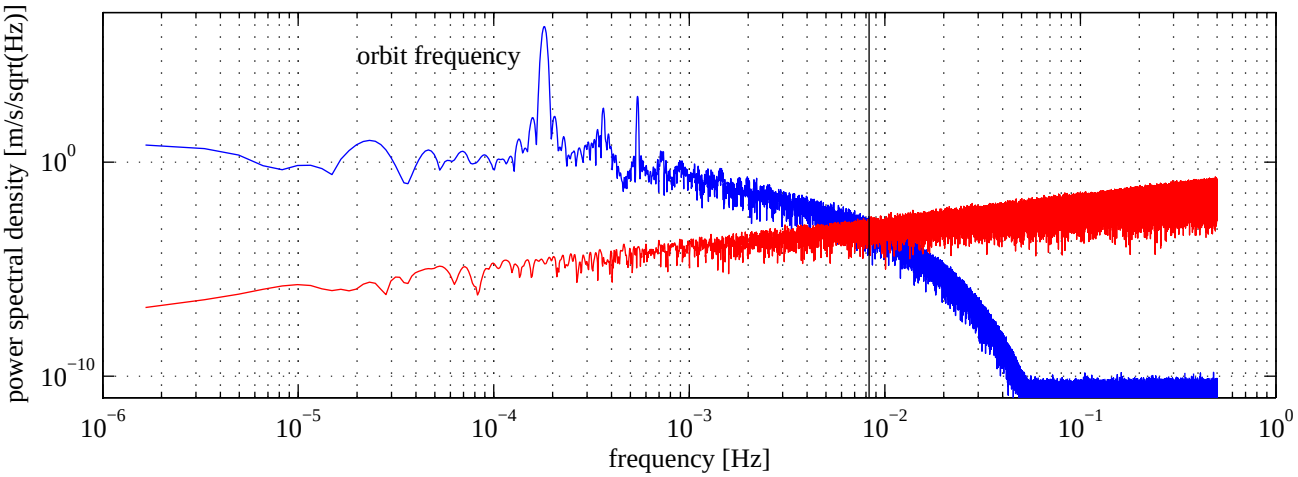

Figure 2.4: Power spectral density of velocity signal and errors.

depending on the frame in which the computation is performed, and can as well be explained by the following derivation.

Newton's second law states (Newton (1687)), that *the rate of change of momentum of a body is proportional to the resultant force acting on the body and is in the same direction*:

$$\mathbf{F} = \frac{\mathrm{d}(m\dot{\mathbf{r}})}{\mathrm{d}t} \ . \tag{2.20}$$

Multiplying this equation by $\dot{\mathbf{r}}$ and integrating over time leads to the energy integral of the satellite's motion (under the assumption that the satellite mass is constant):

$$\int \mathbf{F} \cdot \dot{\mathbf{r}} \, \mathrm{d}t = \frac{1}{2} m \dot{\mathbf{r}}^2 \ . \tag{2.21}$$

The right hand side of this equation is the kinetic energy while the expression on the left hand side describes the work W done by the force $\mathbf{F}$, which equals the integral of the force over the path $\mathrm{d}\mathbf{r}$:

$$W = \int \mathbf{F} \cdot \mathrm{d}\mathbf{r} = \int \mathbf{F} \cdot \dot{\mathbf{r}} \, \mathrm{d}t \ . \tag{2.22}$$

The energy integral is generally path-dependent, but not in a conservative force field, where the work equals the negative difference in potential energy between end and starting point of the motion, or respectively the potential energy in the end point plus an unknown integration constant.:

$$W = -\Delta W_{\mathrm{pot}} = -W_{\mathrm{pot}} + H \ . \tag{2.23}$$

The minus sign indicates that the potential energy is being expended and converted to some other form of energy (kinetic energy in this case). If the satellite would move in a conservative gravity field, inserting this in equation 2.21 would lead to the law of energy conservation (equ. 2.19):

$$H = W_{\mathrm{kin}} + W_{\mathrm{pot}} \ , \tag{2.24}$$

or respectively for unit mass (again applying the sign convention for the gravitational potential V as used in geodesy):

$$C = \frac{1}{2}\dot{\mathbf{r}}^2 - V \; = \frac{1}{2}\dot{\mathbf{r}}^2 - \int \mathbf{a} \cdot \mathrm{d}\mathbf{r} = \frac{1}{2}\dot{\mathbf{r}}^2 - \int \ddot{\mathbf{r}} \cdot \dot{\mathbf{r}} \, \mathrm{d}t \; , \tag{2.25}$$

where C is the Hamiltonian for unit mass and V is the integral of the accelerations $\mathbf{a}$ along the orbit. But as other forces act on the satellite as well, the law of energy conservation is no longer valid, and the additional forces have to be integrated along the orbit. The forces and their corresponding accelerations, can be classified into four categories depending on their source and treatment in the energy balance approach:

- Static gravity: The static gravity field of the Earth, which is defined as the mean field over a certain period of time or at a certain reference epoch, is a conservative potential and the integral of the corresponding accelerations $\mathbf{a}_\mathrm{g}$ along the orbit is path independent.
- Surface forces: The satellite is subject to external forces like air-drag or solar radiation pressure and internal forces from the satellite's propulsion system. All these forces act on the satellite's surface and are non-conservative, which means that they either drain energy from the system by friction or add energy by thrust. In order to maintain the energy balance, the accelerations caused by surface forces $\mathbf{a}_\mathrm{s}$, which are measured by the onboard accelerometer have to be integrated along the orbit and the resulting quantity has to be used as correction.
- Temporal variations and tides: All mass transports in the Earth system (including oceans and atmosphere) cause temporal variations in the Earth's gravity field. Also the direct attraction from other celestial bodies as the moon, the sun and other planets is time variable due to the motion of the bodies w.r.t. the Earth. In addition they cause indirect tidal effects due to the deformation of the Earth. These gravitational effects cannot be considered conservative as the integral along the orbit is path dependent due to the movement of the gravitating masses and have to be teated like the non-conservative surface forces. The accelerations due to temporal variations and tides $\mathbf{a}_\mathrm{t}$ can be computed from models as explained in appendix A.4.
- Fictitious forces: If the computation is done in the Earth fixed frame, fictitious forces which occur only in the rotating frame have to be considered. They can be easily explained by the chain rule of differentiation:

$$\begin{aligned}
\mathbf{r}_\mathrm{e} &= \mathbf{R}^\mathrm{i}{}_\mathrm{e}\mathbf{r}_\mathrm{i} \; , && (2.26)\\
\dot{\mathbf{r}}_\mathrm{e} &= \mathbf{R}^\mathrm{i}{}_\mathrm{e}\dot{\mathbf{r}}_\mathrm{i} + \dot{\mathbf{R}}^\mathrm{i}_\mathrm{e}\mathbf{r}_\mathrm{i} = \mathbf{R}^\mathrm{i}{}_\mathrm{e}\dot{\mathbf{r}}_\mathrm{i} - \boldsymbol{\omega} \times \mathbf{R}^\mathrm{i}{}_\mathrm{e}\mathbf{r}_\mathrm{i} \; , && (2.27)\\
\ddot{\mathbf{r}}_\mathrm{e} &= \mathbf{R}^\mathrm{i}{}_\mathrm{e}\ddot{\mathbf{r}}_\mathrm{i} + 2\,\dot{\mathbf{R}}^\mathrm{i}_\mathrm{e}\dot{\mathbf{r}}_\mathrm{i} + \ddot{\mathbf{R}}^\mathrm{i}_\mathrm{e}\mathbf{r}_\mathrm{i} = \mathbf{R}^\mathrm{i}{}_\mathrm{e}\ddot{\mathbf{r}}_\mathrm{i} - 2\,\boldsymbol{\omega} \times \mathbf{R}^\mathrm{i}{}_\mathrm{e}\dot{\mathbf{r}}_\mathrm{i} - \dot{\boldsymbol{\omega}} \times \mathbf{R}^\mathrm{i}{}_\mathrm{e}\mathbf{r}_\mathrm{i} + \boldsymbol{\omega} \times \left(\boldsymbol{\omega} \times \mathbf{R}^\mathrm{i}{}_\mathrm{e}\mathbf{r}_\mathrm{i}\right) \; , && (2.28)
\end{aligned}$$

  where $\mathbf{R}^\mathrm{i}{}_\mathrm{e}$ is the rotation matrix from the inertial frame (denoted by the index i) to the Earth-fixed frame (denoted by the index e). Its computation at any given epoch is explained in section A.3. While the first term of equation (2.28) just describes the sum of all accelerations in the inertial frame rotated at any instant to the earth-fixed frame, the other terms describe the fictitious forces which are only observed in the rotating earth-fixed frame. The second term is the Coriolis force acting perpendicular to the velocity, the third term is the Euler force, which is caused by the changes in Earth rotation $\dot{\boldsymbol{\omega}}$ and the fourth term is the centrifugal force acting perpendicular to a plane which is spanned by the rotation axis and the position vector.

If the potential is computed in the earth fixed frame, the sum of all accelerations expressed in Earth-fixed coordinates (we denote $\mathbf{a}_\mathrm{e} = \mathbf{R}^\mathrm{i}{}_\mathrm{e}\ddot{\mathbf{r}}_\mathrm{i}$ for not considering the fictitious forces twice) has to be entered in equation (2.25) which leads to:

$$\begin{aligned}
&\int \ddot{\mathbf{r}}_\mathrm{e} \cdot \mathrm{d}\mathbf{r}_\mathrm{e} = && (2.29)\\
&\int \mathbf{a}_\mathrm{ge} \cdot \mathrm{d}\mathbf{r}_\mathrm{e} + \int (\mathbf{a}_\mathrm{se} + \mathbf{a}_\mathrm{te}) \cdot \mathrm{d}\mathbf{r}_\mathrm{e} - 2\int \left(\boldsymbol{\omega} \times \mathbf{R}^\mathrm{i}{}_\mathrm{e}\dot{\mathbf{r}}_\mathrm{i}\right) \cdot \mathrm{d}\mathbf{r}_\mathrm{e} - \int (\dot{\boldsymbol{\omega}} \times \mathbf{r}_\mathrm{e}) \cdot \mathrm{d}\mathbf{r}_\mathrm{e} + \int \boldsymbol{\omega} \times (\boldsymbol{\omega} \times \mathbf{r}_\mathrm{e}) \cdot \mathrm{d}\mathbf{r}_\mathrm{e}
\end{aligned}$$

Substituting $\mathrm{d}\mathbf{r} = \frac{\mathrm{d}\mathbf{r}}{\mathrm{d}t}\mathrm{d}t$ and $\mathbf{R}^{\mathrm{i}}{}_{\mathrm{e}}\dot{\mathbf{r}}_{\mathrm{i}} = \dot{\mathbf{r}}_{\mathrm{e}} + \boldsymbol{\omega} \times \mathbf{R}^{\mathrm{i}}{}_{\mathrm{e}}\mathbf{r}_{\mathrm{i}}$ (cf. equ. 2.27) in the third integral term leads to:

$$\int \ddot{\mathbf{r}}_{\mathrm{e}} \cdot \mathrm{d}\mathbf{r}_{\mathrm{e}} = \tag{2.30}$$
$$\int \mathbf{a}_{\mathrm{ge}} \cdot \mathrm{d}\mathbf{r}_{\mathrm{e}} + \int (\mathbf{a}_{\mathrm{se}} + \mathbf{a}_{\mathrm{te}}) \cdot \mathrm{d}\mathbf{r}_{\mathrm{e}} - 2\int (\boldsymbol{\omega} \times \dot{\mathbf{r}}_{\mathrm{e}}) \cdot \dot{\mathbf{r}}_{\mathrm{e}}\mathrm{d}t - \int (\dot{\boldsymbol{\omega}} \times \mathbf{r}_{\mathrm{e}}) \cdot \mathrm{d}\mathbf{r}_{\mathrm{e}} - \int \boldsymbol{\omega} \times (\boldsymbol{\omega} \times \mathbf{r}_{\mathrm{e}}) \cdot \mathrm{d}\mathbf{r}_{\mathrm{e}}$$

The first integral term on the right hand side is the gravity potential V. The second integral containing the surface forces $\mathbf{a}_{\mathrm{s}}$ and the time variable effects $\mathbf{a}_{\mathrm{t}}$ cannot be solved analytically and has to be computed by numerical integration. The third integral terms becomes zero, as the Coriolis acceleration is perpendicular to the velocity vector. The fourth term contains the Euler accelerations. The changes of the Earth rotation $\dot{\boldsymbol{\omega}}$ are very small and the term can be neglected. Only the centrifugal accelerations need to be integrated analytically along the orbit, which leads to the centrifugal potential:

$$\int \boldsymbol{\omega} \times (\boldsymbol{\omega} \times \mathbf{r}_{\mathrm{e}}) \cdot \mathrm{d}\mathbf{r}_{\mathrm{e}} = -\frac{1}{2}(\boldsymbol{\omega} \times \mathbf{r}_{\mathrm{e}})^2 + C_{\mathrm{c}} \ . \tag{2.31}$$

If all these forces are considered, equation (2.25) ist extended by three terms which account for non-conservative forces:

$$C = \frac{1}{2}\dot{\mathbf{r}}_{\mathrm{e}}^2 - V - \frac{1}{2}(\boldsymbol{\omega} \times \mathbf{r}_{\mathrm{e}})^2 - \int \mathbf{a}_{\mathrm{se}} \cdot \mathrm{d}\mathbf{r}_{\mathrm{e}} - \int \mathbf{a}_{\mathrm{te}} \cdot \mathrm{d}\mathbf{r}_{\mathrm{e}} \ . \tag{2.32}$$

The integration constant C_{c} from equation (2.31) has been included in the global unknown constant. The potential V can be split up in the normal potential U, which is the potential of a reference ellipsoid and the disturbing potential T, which represents the deviations from the reference ellipsoid. It is numerically more stable to use the disturbing potential T for the gravity field determination instead of the full potential V as the values are several orders of magnitude smaller, therefore (2.33) is rewritten as:

$$T = \frac{1}{2}\dot{\mathbf{r}}_{\mathrm{e}}^2 - U - \frac{1}{2}(\boldsymbol{\omega} \times \mathbf{r}_{\mathrm{e}})^2 - \int \mathbf{a}_{\mathrm{se}} \cdot \mathrm{d}\mathbf{r}_{\mathrm{e}} - \int \mathbf{a}_{\mathrm{te}} \cdot \mathrm{d}\mathbf{r}_{\mathrm{e}} - C \ . \tag{2.33}$$

The disturbing potential T is a linear functional of the gravity field coefficients and now enters the gravity field estimation as pseudo-observable. The unknown energy constant can be estimated as an additional parameter in a least squares solution (cf. section 2.4) or has to be determined by using a priori information (cf. Földváry et al. (2004)).

Computation in the Inertial Frame: The entire computation can also be carried out in the inertial frame, using all quantities expressed in inertial coordinates. The advantage is that some of the involved measurements and models are given in the inertial frame (e.g. the orientation of the satellite or the direct tides). In order to derive the disturbing potential in the inertial system, equation (2.27) has to be substituted into equation (2.33) to replace all expressions in the Earth-fixed frame:

$$\frac{1}{2}\dot{\mathbf{r}}_{\mathrm{e}}^2 = \frac{1}{2}\left(\mathbf{R}^{\mathrm{i}}{}_{\mathrm{e}}\dot{\mathbf{r}}_{\mathrm{i}} - \boldsymbol{\omega} \times \mathbf{R}^{\mathrm{i}}{}_{\mathrm{e}}\mathbf{r}_{\mathrm{i}}\right)^2 = \frac{1}{2}\dot{\mathbf{r}}_{\mathrm{i}}^2 - \dot{\mathbf{r}}_{\mathrm{i}} \cdot (\boldsymbol{\omega} \times \mathbf{r}_{\mathrm{i}}) + \frac{1}{2}(\boldsymbol{\omega} \times \mathbf{r}_{\mathrm{e}})^2 \ , \tag{2.34}$$

$$\int \mathbf{a}_{\mathrm{e}} \cdot \mathrm{d}\mathbf{r}_{\mathrm{e}} = \int \mathbf{a}_{\mathrm{e}} \cdot \dot{\mathbf{r}}_{\mathrm{e}}\mathrm{d}t = \int \mathbf{a}_{\mathrm{e}} \cdot \left(\mathbf{R}^{\mathrm{i}}{}_{\mathrm{e}}\dot{\mathbf{r}}_{\mathrm{i}} - \boldsymbol{\omega} \times \mathbf{R}^{\mathrm{i}}{}_{\mathrm{e}}\mathbf{r}_{\mathrm{i}}\right)\mathrm{d}t = \int \mathbf{a}_{\mathrm{i}} \cdot \dot{\mathbf{r}}_{\mathrm{i}}\mathrm{d}t + \int \mathbf{a}_{\mathrm{i}} \cdot (\boldsymbol{\omega} \times \mathbf{r}_{\mathrm{i}})\,\mathrm{d}t \ . \tag{2.35}$$

Inserted into equation 2.33 one obtains:

$$T = \frac{1}{2}\dot{\mathbf{r}}_\mathrm{i}^2 - U + \dot{\mathbf{r}}_\mathrm{i} \cdot (\boldsymbol{\omega} \times \mathbf{r}_\mathrm{i}) - \int (\mathbf{a}_\mathrm{si} + \mathbf{a}_\mathrm{ti}) \cdot \dot{\mathbf{r}}_\mathrm{i} \mathrm{d}t - \int (\mathbf{a}_\mathrm{si} + \mathbf{a}_\mathrm{ti}) \cdot (\boldsymbol{\omega} \times \mathbf{r}_\mathrm{i})\, \mathrm{d}t - C \ , \tag{2.36}$$

where the centrifugal potential has been replaced by the term $\dot{\mathbf{r}}_\mathrm{i}\,(\boldsymbol{\omega} \times \mathbf{r}_\mathrm{i})$. $\mathbf{v}_\mathrm{r} = (\boldsymbol{\omega} \times \mathbf{r}_\mathrm{i})$ is the velocity the point $\mathbf{r}$ would have in the inertial frame if it was fixed in the rotating frame. As the product of two velocities $\dot{\mathbf{r}}_\mathrm{i}\mathbf{v}_\mathrm{r}$ has the form of kinetic energy, the term can be regarded as a contribution of Earth rotation to the overall energy. The same is applied to the non-conservative accelerations, which leads to an additional integral term.

2.2.3 Error Propagation

The disturbing potential values along the orbit – derived from kinematic positions – cannot be regarded as independent in-situ measurements. Already kinematic orbit positions are correlated even though they are estimated independently. Neighboring points use a similar GPS constellation and contain similar systematic effects. If one regards a full variance/covariance matrix of GPS positions (cf. fig. 3.16), it is apparent, that there are correlations larger than 0.5 over long arcs. The correlations only get weaker if there are significant changes in the GPS satellite constellation (e.g one satellite descends and another one is taken into the computation), or vanish in case of data gaps. In addition, colored noise is introduced by the velocity derivation, which can be regarded as FIR-filter. This should be considered in an error propagation.

If $\boldsymbol{\Sigma}_{xx}$ is the full variance/covariance matrix of a vector of statistical quantities $\mathbf{x}$, the error information can be propagated to another vector of statistical quantities $\mathbf{y}$ by the relation (cf. Niemeier (2002)):

$$\boldsymbol{\Sigma}_{yy} = \mathbf{A}\boldsymbol{\Sigma}_{xx}\mathbf{A}^\mathrm{T} \ , \tag{2.37}$$

where $\mathbf{A}$ is the Jacobi matrix of partial derivatives of the elements of $\mathbf{y}$ w.r.t. the elements of $\mathbf{x}$.

The disturbing potential T is derived from the orbit positions $\mathbf{r}$ via the velocities $\dot{\mathbf{r}}$. Hence the error propagation from positions to potential values consists of two steps:

$$\mathbf{P}_{TT}^{-1} = \boldsymbol{\Sigma}_{TT} = \mathbf{A}_W \mathbf{A}_{\dot{r}} \boldsymbol{\Sigma}_{rr} \mathbf{A}_{\dot{r}}^\mathrm{T} \mathbf{A}_W^\mathrm{T} \ . \tag{2.38}$$

The variance/covariance matrix of the potential values $\boldsymbol{\Sigma}_{TT}$ is the inverse of the weight matrix $\mathbf{P}_{TT}$ that enters the adjustment as described in section 2.4.

The variance/covariance matrix of the positions $\boldsymbol{\Sigma}_{rr}$ is a result of the orbit determination. It is the inverse of the normal matrix of the orbit adjustment scaled with a variance factor. The dimension of the full matrix of an arc of n samples is $3n \times 3n$, as each orbit position consists of 3 components.

In a first step, the variance/covariance matrix of the velocities is computed. Therefore the Jacobi matrix of partial derivatives of the velocity w.r.t. the positions $\mathbf{A}_{\dot{r}}$ has to be applied. If a FIR-filter described in section A.1 is used, the partial derivatives correspond to the filter coefficients. If for example the 5-point differentiation (equ. A.6)

$$\dot{x}_i = \frac{x_{i-2} - 8x_{i-1} + 8x_{i+1} - x_{i+2}}{12h} \ , \tag{2.39}$$

is used, the matrix reads:

$$\mathbf{A}_{\dot{r}} = \frac{1}{12h}\begin{pmatrix}
1 & 0 & 0 & -8 & 0 & 0 & 0 & 0 & 0 & 8 & 0 & 0 & -1 & \cdots & 0 & 0 & 0 & 0 & 0 \\
0 & 1 & 0 & 0 & -8 & 0 & 0 & 0 & 0 & 0 & 8 & 0 & 0 & \cdots & 0 & 0 & 0 & 0 & 0 \\
0 & 0 & 1 & 0 & 0 & -8 & 0 & 0 & 0 & 0 & 0 & 8 & 0 & \cdots & 0 & 0 & 0 & 0 & 0 \\
0 & 0 & 0 & 1 & 0 & 0 & -8 & 0 & 0 & 0 & 0 & 0 & 8 & \cdots & 0 & 0 & 0 & 0 & 0 \\
0 & 0 & 0 & 0 & 1 & 0 & 0 & -8 & 0 & 0 & 0 & 0 & 0 & \cdots & 0 & 0 & 0 & 0 & 0 \\
0 & 0 & 0 & 0 & 0 & 1 & 0 & 0 & -8 & 0 & 0 & 0 & 0 & \cdots & 0 & 0 & 0 & 0 & 0 \\
0 & 0 & 0 & 0 & 0 & 0 & 1 & 0 & 0 & -8 & 0 & 0 & 0 & \cdots & 0 & 0 & 0 & 0 & 0 \\
0 & 0 & 0 & 0 & 0 & 0 & 0 & 1 & 0 & 0 & -8 & 0 & 0 & \cdots & 0 & 0 & 0 & 0 & 0 \\
\vdots & \vdots & \vdots & \vdots & \vdots & \vdots & \vdots & \vdots & \vdots & \vdots & \vdots & \vdots & \vdots & \ddots & \vdots & \vdots & \vdots & \vdots & \vdots \\
0 & 0 & 0 & 0 & 0 & 0 & 0 & 0 & 0 & 0 & 0 & 0 & 0 & \cdots & -1 & 0 & 0 & 0 & 0 \\
0 & 0 & 0 & 0 & 0 & 0 & 0 & 0 & 0 & 0 & 0 & 0 & 0 & \cdots & 0 & -1 & 0 & 0 & 0 \\
0 & 0 & 0 & 0 & 0 & 0 & 0 & 0 & 0 & 0 & 0 & 0 & 0 & \cdots & 0 & 0 & -1 & 0 & 0 \\
0 & 0 & 0 & 0 & 0 & 0 & 0 & 0 & 0 & 0 & 0 & 0 & 0 & \cdots & 8 & 0 & 0 & -1 & 0 \\
0 & 0 & 0 & 0 & 0 & 0 & 0 & 0 & 0 & 0 & 0 & 0 & 0 & \cdots & 0 & 8 & 0 & 0 & -1
\end{pmatrix} \tag{2.40}$$

The dimension of the matrix is $(3n-12) \times 3n$, as the first and last two positions of an arc have to be truncated. In a second step the Jacobi matrix of partial derivatives of the kinetic energy w.r.t. the velocity has to be applied:

$$\mathbf{A}_W = \frac{1}{12h}\begin{pmatrix}
\dot{x}_3 & \dot{y}_3 & \dot{z}_3 & 0 & 0 & 0 & 0 & 0 & 0 & \cdots & 0 & 0 & 0 \\
0 & 0 & 0 & \dot{x}_4 & \dot{y}_4 & \dot{z}_4 & 0 & 0 & 0 & \cdots & 0 & 0 & 0 \\
0 & 0 & 0 & 0 & 0 & 0 & \dot{x}_5 & \dot{y}_5 & \dot{z}_5 & \cdots & 0 & 0 & 0 \\
\vdots & \vdots & \vdots & \vdots & \vdots & \vdots & \vdots & \vdots & \ddots & \vdots & \vdots & \vdots & \\
0 & 0 & 0 & 0 & 0 & 0 & 0 & 0 & 0 & \cdots & \dot{x}_{n-2} & \dot{y}_{n-2} & \dot{z}_{n-2}
\end{pmatrix}. \tag{2.41}$$

The dimension of this matrix is $(n-4) \times (3n-12)$. The resulting variance/covariance matrix has the dimension $(n-4) \times (n-4)$. As both the $\mathbf{A}_{\dot{r}}$ an the $\mathbf{A}_W$ matrices are sparse, they can be handled very efficiently.

Practical Considerations: Using a variance/covariance matrix for a complete satellite mission with several million observations would use too much memory. It has to be simplified in a reasonable way. The memory use has to be reduced to a manageable level while as much as possible of the covariance information has to be preserved. Possible alternatives to a full $\mathbf{\Sigma}_{rr}$ matrix are:

- $\mathbf{\Sigma}_{rr} = \mathbf{I}$: All correlations between the positions and components are neglected. This requires no memory at all.
- $\mathbf{\Sigma}_{rr} = \mathbf{\Sigma}_{33}$: Only the 3×3 matrices for the components of one position are used. Correlations between different positions are neglected.
- $\mathbf{\Sigma}_{rr} = \mathbf{\Sigma}_{\text{band}}$: Only a small diagonal band of the full matrix is saved. This seems logic, as the velocity derivation will amplify the band structure of the variance covariance matrix. But artificially cutting out a band will destroy the semi-positive definiteness of the variance/covariance matrix.
- $\mathbf{\Sigma}_{rr} = \mathbf{\Sigma}_{\text{block}}$: The orbit data is cut into several short arcs. All correlations between those arcs will be neglected but all information within one arc will be preserved. This is probably the best compromise between memory usage and preservation of information. In average a GPS constellation is observed 20 min before the constellation changes. Storing full blocks of 20 min length up to an hour would result in a manageable data volume (which is dependent on the sampling rate). Using data gaps as natural separation between arcs is useful, as the correlation is lost anyway.

2.3 Satellite Gravity Gradiometry

The GOCE-mission will be the first satellite mission to carry a gravity gradiometer to space. The gradiometer will consist of 6 accelerometers which are pairwise arranged on 3 axes orthogonal at the center of mass of the satellite. The axes of the single accelerometers will be (in the ideal case) aligned with the gradiometer axes, which define the gradiometer reference frame (GRF). Each accelerometer has one axis with reduced accuracy, due to the calibration on Earth, which is displayed in figure 2.5 by a shorter sidelength.

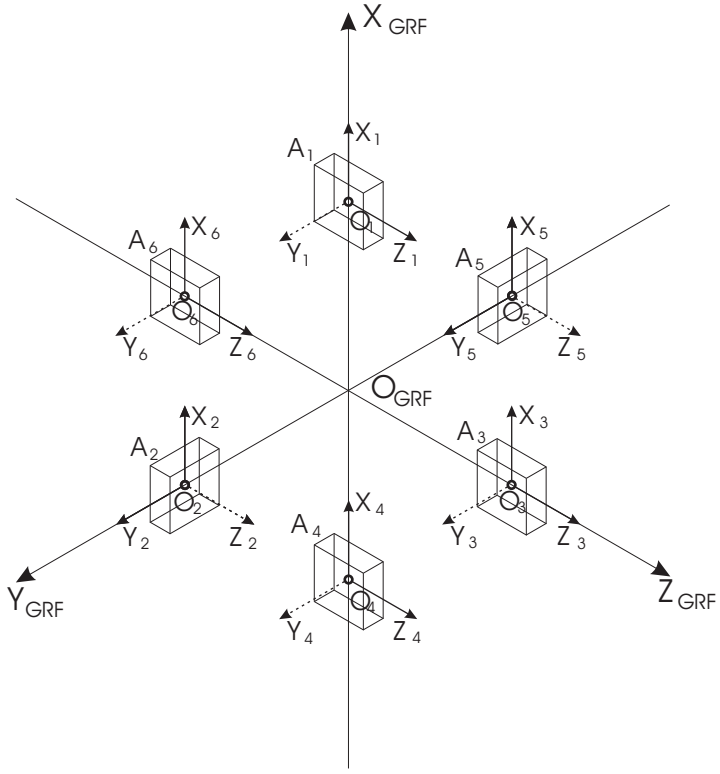

Figure 2.5: Gradiometer configuration.

The acceleration observed by a single accelerometer is given by

$$\mathbf{a} = -\nabla^2 V \cdot \mathbf{r} + \dot{\boldsymbol{\omega}} \times \mathbf{r} + \boldsymbol{\omega} \times (\boldsymbol{\omega} \times \mathbf{r}) + \mathbf{a}_{\text{non}} \ , \tag{2.42}$$

where $\mathbf{r}$ is the position vector of the accelerometer origin in the GRF. $\mathbf{a}$ is not only influenced by gravitational forces, but also by the fictitious Euler and centrifugal forces caused by the rotation of the satellite and by external non-conservative forces $\mathbf{a}_{\text{non}}$ like air drag and solar radiation pressure. These external forces are determined by averaging the accelerations of the two accelerometers of one pair. Basically there is some redundancy, as each component is measured by each pair, so that altogether 9 so-called *common mode* accelerations are measured, but 3 of them are measured by the weaker accelerometer axes and should not be used. The common mode accelerations are computed in real time on-board and serve as input for the drag-free-control system (DFACS) to compensate in flight direction the external forces in the measurement bandwidth with ion-thrusters. Residual accelerations are eliminated when taking the *differential mode* accelerations:

$$\frac{1}{L} \begin{pmatrix} a_{x1} - a_{x4} & a_{y1} - a_{y4} & a_{z1} - a_{z4} \\ a_{x2} - a_{x5} & a_{y2} - a_{y5} & a_{z2} - a_{z5} \\ a_{x3} - a_{x6} & a_{y3} - a_{y6} & a_{z3} - a_{z6} \end{pmatrix}$$

$$= \begin{pmatrix} V_{xx} & V_{xy} & V_{xz} \\ V_{xy} & V_{yy} & V_{yz} \\ V_{xz} & V_{yz} & V_{zz} \end{pmatrix} + \begin{pmatrix} 0 & \dot{\omega}_z & -\dot{\omega}_y \\ -\dot{\omega}_z & 0 & \dot{\omega}_x \\ \dot{\omega}_y & -\dot{\omega}_x & 0 \end{pmatrix} + \begin{pmatrix} -\omega_y^2 - \omega_z^2 & \omega_x\omega_y & \omega_x\omega_z \\ \omega_x\omega_y & -\omega_x^2 - \omega_z^2 & \omega_y\omega_z \\ \omega_x\omega_z & \omega_y\omega_z & -\omega_x^2 - \omega_y^2 \end{pmatrix}, \quad (2.43)$$

or in matrix form:

$$\boldsymbol{\Gamma} = \mathbf{V} + \dot{\boldsymbol{\Omega}} + \boldsymbol{\Omega}\boldsymbol{\Omega} \; . \quad (2.44)$$

This is the fundamental equation of satellite gradiometry. It contains three terms, the tensor of second derivatives of the gravity potential $\mathbf{V}$, the permutation tensor $\dot{\boldsymbol{\Omega}}$ of the angular accelerations and a product of the permutation tensor $\boldsymbol{\Omega}$ of the angular velocities with itself. As $\mathbf{V}$ and $\boldsymbol{\Omega}\boldsymbol{\Omega}$ are symmetric and $\dot{\boldsymbol{\Omega}}$ is anti-symmetric, the latter can easily be isolated by: $\dot{\boldsymbol{\Omega}} = \frac{1}{2}\left(\boldsymbol{\Gamma} + \boldsymbol{\Gamma}^{\mathrm{T}}\right)$, which yields the angular rates of the satellites motion. The angular velocities cannot be obtained directly and have to be computed by integration of the angular accelerations together with attitude data from the star trackers in a Kalman filter process. This *angular rate reconstruction* is done by the GOCE payload data segment (PDS), and the level 1B data which is available for gravity field determination contains the tensor of second derivatives of the gravitational potential $\mathbf{V}$.

The expected accuracy of the observed gravity gradients is below $10^{-2}\,\mathrm{E}$ ($1\,\mathrm{E} = 10^{-9}\,\mathrm{s}^{-2}$) in the measurement bandwidth (MBW: 5 mHz – 100 mHz). Due to the configuration of the accelerometers as shown in figure 2.5 only the V_{xx}, V_{yy}, V_{zz} and the $V_{xz} = V_{zx}$ components of the gravity tensor will achieve this level of accuracy. The accuracy of the other components is expected to be one order of magnitude less.

Figure 2.6 shows the power spectral density (PSD) of the expected errors of the diagonal components. The precision of below $10^{-2}\,\mathrm{E}$ is only achievable inside the MBW. Towards the low frequencies (below 5 mHz) the error behavior increases proportional with the inverse frequency. In this spectral domain support from the SST observations is necessary. The error increases towards high frequencies (above 100 mHz). This spectral behavior of the observation noise has to be taken into account by filtering (e.g. Schuh (1996)). Using the semi-analytical approach, the filtering can be applied in the spectral domain (see sec. 2.5).

Temporal Gravity Field Changes: The measured gradients do not only contain the static part of the gravity field – whose determination is the primary goal of GOCE – but also the time variable part. Hence for the determination of the static part the gradients have to be corrected for those effects. The effects that have to be considered – namely tides and changes due to mass variations in the Earth system – are basically the same as for the accelerations mentioned in section 2.2.2, with the difference, that some of the small effects which can be neglected on acceleration level, like mass variations in atmosphere and ocean, become more important on gradient level. Their exact computation is described in section A.4.

Frame Transformation of the Gravity Tensor: The equations to compute the elements of the gravity tensor by spherical harmonic synthesis given in section 2.1, as well as the observation equations to be discussed in section 2.4 are defined in the topocentric frame LNOF, while the measured gradients are given in the gradiometer reference frame (GRF). Hence the measured gradients should be transformed to the LNOF for gravity field computation. As some of the tensor components have reduced accuracy (see below), they would also deteriorate the components with high accuracy. Thus the observation equations have to be rotated to the system, where the measurement is taking place. The orientation of the satellite w.r.t. the inertial reference frame (IRF) is measured by star trackers and given by quaternions. As the LNOF is connected to an earth-fixed frame (ERF) via the geographic coordinates

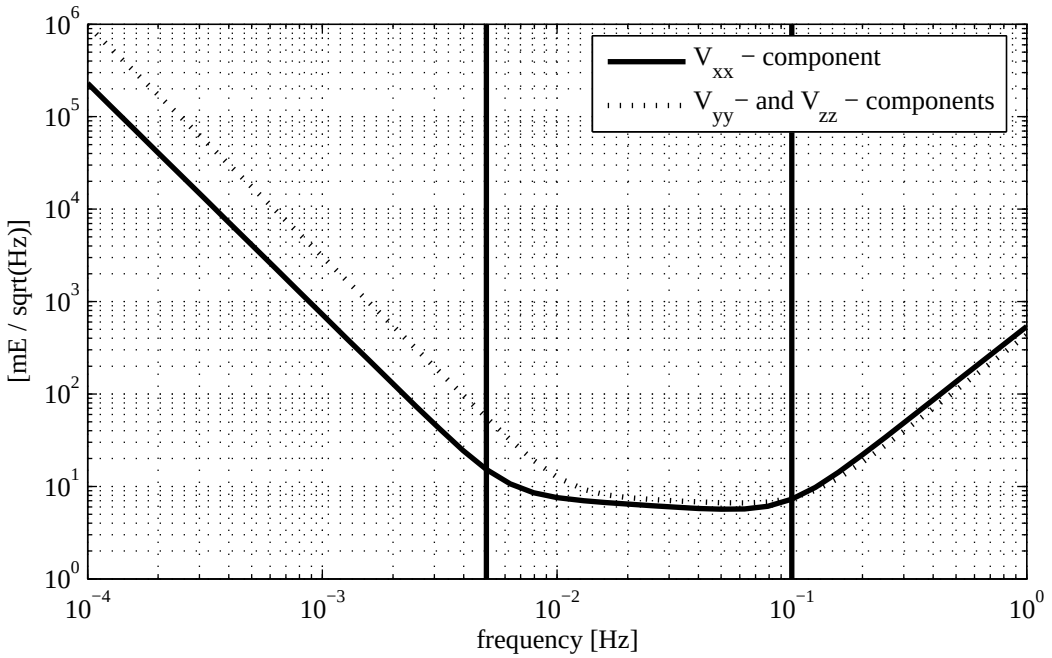

Figure 2.6: Power spectral density of the expected gradiometer errors.

θ and λ, the tensor can be rotated to the ERF first, then to the IRF and finally to the GRF. Note that in order to rotate a tensor, the rotation matrix has to be applied from left, and its transpose from right.

$$\mathbf{V}_{\mathrm{GRF}} = \mathbf{R}^{\mathrm{LNOF}}_{\mathrm{GRF}}\ \mathbf{V}_{\mathrm{LNOF}}\ \mathbf{R}^{\mathrm{GRF}}_{\mathrm{LNOF}}\ , \tag{2.45}$$

where

$$\mathbf{R}^{\mathrm{LNOF}}_{\mathrm{GRF}} = \mathbf{R}^{\mathrm{IRF}}_{\mathrm{GRF}}\ \mathbf{R}^{\mathrm{ERF}}_{\mathrm{IRF}}\ \mathbf{R}^{\mathrm{LNOF}}_{\mathrm{ERF}}\ . \tag{2.46}$$

The transformation between the topocentric and the geocentric frame can be computed by

$$\mathbf{R}^{\mathrm{LNOF}}_{\mathrm{ERF}} = \mathbf{P}_1\ \mathbf{R}_2(90^\circ - \phi)\ \mathbf{R}_3(-\lambda) = \begin{pmatrix} -\cos\theta\cos\lambda & -\cos\theta\sin\lambda & \sin\theta \\ -\sin\lambda & \cos\lambda & 0 \\ \sin\theta\cos\lambda & \sin\theta\sin\lambda & \cos\theta \end{pmatrix}\ , \tag{2.47}$$

where $\mathbf{P}_1$ is the reflection about the x-axis, as the LNOF is a left hand system. The transformation between ERF and IRF consists of the transformations due to the motion of the celestial pole (precession and nutation) $\mathbf{Q}(t)$, the Earth rotation $\mathbf{R}(t)$ and polar motion $\mathbf{W}(t)$:

$$\mathbf{R}^{\mathrm{ERF}}_{\mathrm{IRF}} = \mathbf{Q}(t)\ \mathbf{R}(t)\ \mathbf{W}(t)\ . \tag{2.48}$$

The details of the computation are listed in section A.3. The rotation from the IRF to the satellite fixed GRF is derived from the orientation which is observed by the on-board star sensors and given in quaternions:

$$\mathbf{R}^{\mathrm{IRF}}_{\mathrm{GRF}} = \begin{pmatrix} q_0^2+q_1^2-q_2^2-q_3^2 & 2(q_1q_2-q_0q_3) & 2(q_1q_3+q_0q_2) \\ 2(q_1q_2+q_0q_3) & q_0^2-q_1^2+q_2^2-q_3^2 & 2(q_2q_3-q_0q_1) \\ 2(q_1q_3-q_0q_2) & 2(q_2q_3+q_0q_1) & q_0^2-q_1^2-q_2^2+q_3^2 \end{pmatrix}\ . \tag{2.49}$$

Quaternions are an extension to complex numbers which are often used to describe rotations (e.g. Wertz (1988)). They consist of only 4 elements in contrast to the 9 elements of a rotation matrix (actually only 3 elements are independent, as the norm of a rotation quaternion is defined as 1). Compared to Euler or Cardan rotation angles they have the advantage of being free of singularities.

2.4 Direct Solution

2.4.1 Least-Squares Adjustment

In order to derive u unknown parameters $\mathbf{x}$ from a set of n observations $\mathbf{l}$ containing measurement errors, which form an overdetermined system ($n > u$), the method of least squares adjustment is used. A functional model of observation equations has to be set up expressing the measurements as functions of the unknown parameters: $\mathbf{l} = f(\mathbf{x}) + \boldsymbol{\epsilon}$, where $\boldsymbol{\epsilon}$ is the vector of measurement errors. The model can then be linearized and written as a single vector equation:

$$\mathbf{l} + \mathbf{v} = \mathbf{A}\mathbf{x}, \tag{2.50}$$

where

- $\mathbf{l}$ is the vector of observations,
- $\mathbf{x}$ is the vector of unknown parameters and
- $\mathbf{v}$ are the corrections making the system of equations consistent.

The linearization is done by deriving the observation equations w.r.t. the unknown parameters. So the design-matrix $\mathbf{A}$ is the Jacobi-matrix of the system of equations with n observations and u unknowns :

$$\mathbf{A} = \frac{\partial f(\mathbf{x})}{\partial \mathbf{x}} = \begin{bmatrix} \frac{\partial f_1(\mathbf{x})}{\partial x_1} & \frac{\partial f_1(\mathbf{x})}{\partial x_2} & \cdots & \frac{\partial f_1(\mathbf{x})}{\partial x_u} \\ \frac{\partial f_2(\mathbf{x})}{\partial x_1} & \frac{\partial f_2(\mathbf{x})}{\partial x_2} & \cdots & \frac{\partial f_2(\mathbf{x})}{\partial x_u} \\ \vdots & \vdots & \ddots & \vdots \\ \frac{\partial f_n(\mathbf{x})}{\partial x_1} & \frac{\partial f_n(\mathbf{x})}{\partial x_2} & \cdots & \frac{\partial f_n(\mathbf{x})}{\partial x_u} \end{bmatrix} . \tag{2.51}$$

As the measurements may also be correlated the full variance/covariance information has to be taken into account by the variance/covariance matrix of the observations $\boldsymbol{\Sigma}_{ll}$:

$$\boldsymbol{\Sigma}_{ll} = \begin{bmatrix} \sigma_1^2 & \sigma_{12} & \cdots & \sigma_{1n} \\ \sigma_{21} & \sigma_2^2 & \cdots & \sigma_{1n} \\ \vdots & \vdots & \ddots & \vdots \\ \sigma_{n1} & \sigma_{n2} & \cdots & \sigma_n^2 \end{bmatrix} . \tag{2.52}$$

The aim of the least squares adjustment is to estimate the parameters $\mathbf{x}$ such, that the sum of squares of the corrections weighted by $\mathbf{P} = \boldsymbol{\Sigma}_{ll}^{-1}$, is minimized:

$$\mathbf{v}^{\mathrm{T}}\mathbf{P}\mathbf{v} = (\mathbf{A}\mathbf{x} - \mathbf{l})^{\mathrm{T}}\,\mathbf{P}\,(\mathbf{A}\mathbf{x} - \mathbf{l}) = \min \ . \tag{2.53}$$

The solution for the estimated parameters $\hat{\mathbf{x}}$ is (cf. Niemeier (2002)):

$$\hat{\mathbf{x}} = \left(\mathbf{A}^{\mathrm{T}}\mathbf{P}\mathbf{A}\right)^{-1}\mathbf{A}^{\mathrm{T}}\mathbf{P}\mathbf{l} = \mathbf{N}^{-1}\mathbf{n} \ , \tag{2.54}$$

where $\mathbf{N} = \mathbf{A}^{\mathrm{T}}\mathbf{P}\mathbf{A}$ is called normal equation matrix, and $\mathbf{n} = \mathbf{A}^{\mathrm{T}}\mathbf{P}\mathbf{l}$ the right hand side of the normal equation $\mathbf{N}\hat{\mathbf{x}} = \mathbf{n}$.

In the case of gravity field analysis the unknown parameters are the spherical harmonic potential coefficients $\bar{C}_{lm}$ and $\bar{S}_{lm}$. Using functionals of the potential as (pseudo-)observations, like the disturbing potential from the energy balance method, accelerations from the acceleration approach or the components of the gravity tensor from SGG, the observation equations are already linear and the elements of $\mathbf{A}$ can be derived using the quantities from table 2.1:

$$\left.\begin{matrix} \frac{\partial V_{ij}}{\partial \alpha} \\ \frac{\partial V_{ij}}{\partial \beta} \end{matrix}\right\} = \frac{GM}{R}\lambda_{ij}\left(\frac{R}{r}\right)^{l+1} p \left\{ \begin{matrix} \cos(m\lambda) \\ \sin(m\lambda) \end{matrix}\right. \quad . \tag{2.55}$$

Quality Assessment: In order to asses the quality of the observations and the solution, the residuals after adjustment

$$\hat{\mathbf{v}} = \mathbf{A}\hat{\mathbf{x}} - \mathbf{l} \tag{2.56}$$

have to be computed. The residuals can be used to detect outliers in the observations, and a PSD of the residuals can give conclusions about the spectral error behavior of the observations. The a posteriori variance factor is computed by:

$$\hat{\sigma}_0^2 = \frac{\hat{\mathbf{v}}^{\mathrm{T}}\mathbf{P}\hat{\mathbf{v}}}{n-u} \; . \tag{2.57}$$

For large data sets the Jacobi-matrix $\mathbf{A}$ can be very large and may no longer be available in memory after the adjustment. To avoid a recomputation, the a posteriori variance factor can alternatively be estimated by:

$$\hat{\sigma}_0^2 = \frac{\mathbf{l}^{\mathrm{T}}\mathbf{P}\mathbf{l} - \mathbf{n}^{\mathrm{T}}\hat{\mathbf{x}}}{n-u} \; . \tag{2.58}$$

As the normal equation matrix $\mathbf{N}$ is only determined by the inner geometry of the data distribution (but not by the observations themselves which only enter on the right hand side of the system of normal equations $\mathbf{n}$), its inverse can be used to determine, whether the data distribution is well suited or ill-posed for the estimation of the potential coefficients. The variance factor is used to scale the variance/covariance matrix of the coefficients:

$$\mathbf{\Sigma}_{\hat{\mathbf{x}}\hat{\mathbf{x}}} = \hat{\sigma}_0^2\mathbf{N}^{-\mathbf{1}} \; . \tag{2.59}$$

The square root of the diagonal of $\mathbf{\Sigma}_{\hat{\mathbf{x}}\hat{\mathbf{x}}}$ contains the standard deviation of the potential coefficients $\sigma(\bar{C}_{lm})$ and $\sigma(\bar{S}_{lm})$, which are the formal error measures. By normalizing the inverse of the normal equation matrix, one obtains the correlation matrix $\mathbf{C}$ of the potential coefficients:

$$\mathbf{C}_{ij} = \frac{\mathbf{N}_{ij}^{-1}}{\sqrt{\mathbf{N}_{ii}^{-1}\mathbf{N}_{jj}^{-1}}}. \tag{2.60}$$

The correlation between two coefficients $\mathbf{C}_{ij}$, is computed by dividing the covariance by the square root of the corresponding variances of those coefficients. Hence the correlation matrix should ideally be $\mathbf{I}$. Otherwise coefficients are correlated and cannot be estimated independently.

In order to obtain a global image of the quality of the solution, a variance/covariance propagation to geoid heights, vertical deflections or other functionals of the potential, on a global grid can be computed using:

$$\mathbf{M} = \mathbf{B}\boldsymbol{\Sigma}_{\hat{\mathbf{x}}\hat{\mathbf{x}}}\mathbf{B}^{\mathrm{T}} \ , \tag{2.61}$$

where the diagonal of $\mathbf{M}$ contains the formal propagated error variances of the functional at the grid points, and the off-diagonal elements contain the error covariance between these points. The Jacobi matrix $\mathbf{B}$ contains in this case the partial derivatives of the functional at the grid points w.r.t. the potential coefficients. For geoid heights this reads:

$$\left.\begin{array}{c} \frac{\partial N(\theta,\lambda,r)}{\partial \bar{C}_{lm}} \\ \frac{\partial N(\theta,\lambda,r)}{\partial \bar{S}_{lm}} \end{array}\right\} = R\left(\frac{R}{r}\right)^{l+1} \bar{P}_{lm}(\cos\theta) \left\{\begin{array}{c} \cos(m\lambda) \\ \sin(m\lambda) \end{array}\right. \ . \tag{2.62}$$

2.4.2 Computational Aspects

Parallelization: The Jacobi matrix $\mathbf{A}$ can become too large to fit into the computer memory at once. Its number of rows equals the number of samples, which can reach several millions for satellite missions of several months or years with a sampling rate of down to one second and several observation types. The number of columns equals the number of potential coefficients, which is $(L+1)^2$. One method to deal with a matrix of this size is to cut the satellite orbit in smaller arcs, as proposed by Wermuth (2001) – at the cost of losing all covariance information between the arcs. This method is ideal for parallelization, as the arcs and the computational workload can be distributed over several computer nodes. Each node can independently process an arc and set up the corresponding contribution to the normal equations, requiring only a minimum of communication between the nodes. Finally the partial systems of normal equations have to be collected and solved on a single node. The normal matrix becomes:

$$\begin{aligned} \mathbf{N} &= \mathbf{A}^{\mathrm{T}}\mathbf{P}\mathbf{A} = \begin{pmatrix} \mathbf{A}_1^{\mathrm{T}} & \mathbf{A}_2^{\mathrm{T}} & ... & \mathbf{A}_n^{\mathrm{T}} \end{pmatrix} \begin{pmatrix} \mathbf{P}_1 & 0 & \cdots & 0 \\ 0 & \mathbf{P}_2 & \cdots & 0 \\ \vdots & \vdots & \ddots & \vdots \\ 0 & 0 & \cdots & \mathbf{P}_n \end{pmatrix} \begin{pmatrix} \mathbf{A}_1 \\ \mathbf{A}_2 \\ \vdots \\ \mathbf{A}_n \end{pmatrix} \\ &= \mathbf{A}_1^{\mathrm{T}}\mathbf{P}_1\mathbf{A}_1 + \mathbf{A}_2^{\mathrm{T}}\mathbf{P}_2\mathbf{A}_2 + ... + \mathbf{A}_n^{\mathrm{T}}\mathbf{P}_n\mathbf{A}_n = \mathbf{N}_1 + \mathbf{N}_2 + ... + \mathbf{N}_n \quad , \end{aligned} \tag{2.63}$$

and similarly:

$$\begin{aligned} \mathbf{n} &= \mathbf{A}^{\mathrm{T}}\mathbf{P}\mathbf{l} = \begin{pmatrix} \mathbf{A}_1^{\mathrm{T}} & \mathbf{A}_2^{\mathrm{T}} & ... & \mathbf{A}_n^{\mathrm{T}} \end{pmatrix} \begin{pmatrix} \mathbf{P}_1 & 0 & \cdots & 0 \\ 0 & \mathbf{P}_2 & \cdots & 0 \\ \vdots & \vdots & \ddots & \vdots \\ 0 & 0 & \cdots & \mathbf{P}_n \end{pmatrix} \begin{pmatrix} \mathbf{l}_1 \\ \mathbf{l}_2 \\ \vdots \\ \mathbf{l}_n \end{pmatrix} \\ &= \mathbf{A}_1^{\mathrm{T}}\mathbf{P}_1\mathbf{l}_1 + \mathbf{A}_2^{\mathrm{T}}\mathbf{P}_2\mathbf{l}_2 + ... + \mathbf{A}_n^{\mathrm{T}}\mathbf{P}_n\mathbf{l}_n = \mathbf{n}_1 + \mathbf{n}_2 + ... + \mathbf{n}_n \quad . \end{aligned} \tag{2.64}$$

If also the memory requirements of the normal matrix $\mathbf{N}$ exceed the available memory of one node, it has to be distributed over several nodes – at the cost that parts of the $\mathbf{A}$-matrix have to be computed by several nodes. This is described in detail in Plank (2004).

Regularization: In gravity field analysis from satellite missions, the normal matrix is often ill-posed. This implies that the solution is weakly determined because of the downward continuation and the lack of data in the polar region for satellites with low inclination. The system of equations can be stabilized by introducing a priori information. A common method used in mathematics is the *Tikhonov Regularization*, which tries to find a compromise between minimizing the error $\mathbf{v}^{\mathrm{T}}\mathbf{P}\mathbf{v}$ and minimizing the parameter norm $\mathbf{x}^{\mathrm{T}}\mathbf{x}$:

$$\mathbf{v}^{\mathrm{T}}\mathbf{P}\mathbf{v} + \alpha^2\mathbf{x}^{\mathrm{T}}\mathbf{x} = (\mathbf{A}\mathbf{x} - \mathbf{l})^{\mathrm{T}}\,\mathbf{P}\,(\mathbf{A}\mathbf{x} - \mathbf{l}) + \alpha^2\mathbf{x}^{\mathrm{T}}\mathbf{x} = \min \ . \tag{2.65}$$

This can be interpreted as adding one observation equation per unknown parameter to the system of equations. They are constrained to their expectation value of $E\{\mathbf{x}\} = 0$ and given the freedom to obtain values around the expectation value with the dispersion σ_x. This additional equations are weighted with the standard deviation of the observations σ_b, which leads to the extended equation:

$$\hat{\mathbf{x}} = \left(\mathbf{A}^{\mathrm{T}}\mathbf{P}\mathbf{A} + \alpha^2\mathbf{I}\right)^{-1}\mathbf{A}^{\mathrm{T}}\mathbf{P}\mathbf{l} = \mathbf{N}^{-1}\mathbf{n} \ , \tag{2.66}$$

with the Tikhonov parameter $\alpha = \sigma_b/\sigma_x$. In order to determine the standard deviation of the unknown parameters σ_x a priori information is necessary. Equation (2.65) is based on the assumption, that all unknown parameters have the same statistical attributes. This is not true for the gravity field coefficients. Kaula's rule of thumb (Kaula (1966)) states, that the coefficients of the same degree l have an expectation value $E\{\mathbf{x}_l\} = 0$ and a degree variance of $\sigma_l^2 \approx 160 \cdot 10^{-12}/l^3$. The degree variance is defined as

$$\sigma_l^2 = \sum_{m=0}^{l}\left(\bar{C}_{lm}{}^2 + \bar{S}_{lm}{}^2\right) . \tag{2.67}$$

The standard deviation of coefficients of a certain degree l is:

$$\sigma_x(l) = \sqrt{\frac{\sigma_l^2}{2l+1}} \approx \pm\frac{10^{-5}}{l^2} \ . \tag{2.68}$$

Using this a priori information equation 2.66 reads as:

$$\hat{\mathbf{x}} = \left(\mathbf{A}^{\mathrm{T}}\mathbf{P}\mathbf{A} + \alpha^2\mathbf{R}\right)^{-1}\mathbf{A}^{\mathrm{T}}\mathbf{P}\mathbf{l} \ , \tag{2.69}$$

where $\alpha = \sigma_b$. The standard deviation of the coefficients has been incorporated into the regularization matrix. $\mathbf{R}$ is a diagonal matrix with $1/\sigma_x^2(l)$ of the corresponding coefficient on its diagonal.

This method is often referred to as *Kaula Regularization*. Alternatively the degree variances from an a priori model instead of Kaula's rule of thumb may be used. If one wants to derive a solution which is completely independent of a priori knowledge, an alternative algorithm like the *Spherical Cap Regularization* introduced in Metzler (2007) should be employed.

Elimination of Additional Parameters Sometimes it is necessary to estimate additional parameters together with the gravity field coefficients, like the unknown energy constant described in section 2.2 or accelerometer and gradiometer instrument parameters. If many of those additional parameters are needed, like an energy constant for each of the small arcs described above, the system of normal equations can become too large to be solved efficiently. Instead the arc-specific parameters can be eliminated from the normal equations before the inversion. If one divides the solution vector $\mathbf{x}$ into the parameters $\mathbf{x}_1$

which should be solved for and the parameters $\mathbf{x}_2$ which should be eliminated, the normal matrix $\mathbf{N}$ and the right hand-side of the system of normal equations $\mathbf{n}$ can be written as:

$$\mathbf{N} = \begin{pmatrix} \mathbf{A}_1^{\mathrm{T}} \\ \mathbf{A}_2^{\mathrm{T}} \end{pmatrix} \mathbf{P} \begin{pmatrix} \mathbf{A}_1 & \mathbf{A}_2 \end{pmatrix} = \begin{pmatrix} \mathbf{A}_1^{\mathrm{T}}\mathbf{P}\mathbf{A}_1 & \mathbf{A}_1^{\mathrm{T}}\mathbf{P}\mathbf{A}_2 \\ \mathbf{A}_2^{\mathrm{T}}\mathbf{P}\mathbf{A}_1 & \mathbf{A}_2^{\mathrm{T}}\mathbf{P}\mathbf{A}_2 \end{pmatrix} = \begin{pmatrix} \mathbf{N}_{11} & \mathbf{N}_{12} \\ \mathbf{N}_{21} & \mathbf{N}_{22} \end{pmatrix} , \tag{2.70}$$

$$\mathbf{n} = \begin{pmatrix} \mathbf{A}_1^{\mathrm{T}} \\ \mathbf{A}_2^{\mathrm{T}} \end{pmatrix} \mathbf{P}\mathbf{l} = \begin{pmatrix} \mathbf{A}_1^{\mathrm{T}}\mathbf{P}\mathbf{l} & \mathbf{A}_2^{\mathrm{T}}\mathbf{P}\mathbf{l} \end{pmatrix} = \begin{pmatrix} \mathbf{n}_1 \\ \mathbf{n}_2 \end{pmatrix} . \tag{2.71}$$

So the normal equations read (cf. Niemeier (2002)):

$$\begin{pmatrix} \mathbf{N}_{11} & \mathbf{N}_{12} \\ \mathbf{N}_{21} & \mathbf{N}_{22} \end{pmatrix} \begin{pmatrix} \hat{\mathbf{x}}_1 \\ \hat{\mathbf{x}}_2 \end{pmatrix} = \begin{pmatrix} \mathbf{n}_1 \\ \mathbf{n}_2 \end{pmatrix} . \tag{2.72}$$

If one solves the second equation of the system (2.72) for $\hat{\mathbf{x}}_2$:

$$\hat{\mathbf{x}}_2 = \mathbf{N}_{22}^{-1}\mathbf{n}_2 - \mathbf{N}_{22}^{-1}\mathbf{N}_{21}\hat{\mathbf{x}}_1, \tag{2.73}$$

substitutes it into the first equation of (2.72) and solves for $\hat{\mathbf{x}}_1$ one obtains a version of the adjustment model described by equation 2.54 where the additional parameters have been eliminated:

$$\hat{\mathbf{x}}_1 = \left(\mathbf{N}_{11} - \mathbf{N}_{12}\mathbf{N}_{22}^{-1}\mathbf{N}_{21}\right)^{-1} \left(\mathbf{n}_1 - \mathbf{N}_{12}\mathbf{N}_{22}^{-1}\mathbf{n}_2\right) . \tag{2.74}$$

The eliminated parameters $\hat{\mathbf{x}}_2$ can be reconstructed by a back-substitution of the parameters $\hat{\mathbf{x}}_1$ into equation 2.73.

Contribution Analysis and Variance Component Estimation: As shown above, the normal matrix can be composed as sum of several independent normal matrices from different sets of measurements: $\mathbf{N} = \mathbf{N}_1 + \mathbf{N}_2 + \cdots + \mathbf{N}_n$. These sets can stem from different observation types, like disturbing potential from the energy balance approach or different components of the tensor, or just different arcs of one observation type as described above. They can have different statistical properties and different influence on the potential coefficients. The regularization matrix $\alpha^2\mathbf{R}$ can also be considered as one of the contributions. The influence of a partial data set can be determined by a contribution analysis proposed by Schwintzer (1990). The products of the inverse normal matrix with the partial normal matrices sum up to a unit matrix:

$$\mathbf{N}^{-1}\mathbf{N} = \sum_{i=1}^{n} \mathbf{N}^{-1}\mathbf{N}_i = \mathbf{I} . \tag{2.75}$$

The diagonal of $\mathbf{N}^{-1}\mathbf{N}_i$ contains values between 0 and 1, which show the relative contribution of the partial data set to the coefficients. Here again the normal matrix is only determined by the geometry of the data distribution, but not the actual data. Thus the contribution analysis can only tell, whether a component is well suited for the determination of certain coefficients, and how big the influence of a priori information is. In order to derive weighting factors σ_i, a variance component analysis has to be carried out. Similar to equation (2.57), the variance factor is the weighted norm of the residuals of the partial data set, divided by the redundancy. Koch and Kusche (2001) define the redundancy of a partial data set as difference between the number of observations of that data set n_i and the trace of the contribution matrix $\mathbf{N}^{-1}\mathbf{N}_i$. This (non-integer) number can be interpreted in the way, that the number of parameters that are solved by a partial data set is the sum of all partial contributions on the diagonal of the contribution matrix. Hence the variance factor for one component reads:

$$\hat{\sigma}_i^2 = \frac{\hat{\mathbf{v}}_i^{\mathrm{T}} \mathbf{P}_i \hat{\mathbf{v}}_i}{n_i - \mathbf{N}^{-1}\mathbf{N}_i} \ . \tag{2.76}$$

These variance factors can now be used to improve the weighting between the partial data sets in an iterative process like proposed in Niemeier (2002). Variance factors will be estimated after each iteration and replace the previous variance factors in the next iteration until convergence is achieved.

2.5 Semi-Analytical Solution

As the direct solution described in section 2.4 requires large computer resources it may for certain considerations be advisable to make simplifications to reduce the computational effort and the computation time. The Semi-Analytical approach is based on simplifying assumptions which speed up the whole process of gravity field analysis at the cost of accuracy of the solution (e.g. Sneeuw (2000)). It is often used in pre-mission analysis and will be used as quick-look tool for the processing of GOCE data (see ch. 4).

Based on the assumption of a circular orbit (r = const.) with constant inclination I, equation (2.18) can be rewritten as a two dimensional Fourier series:

$$V_{ij}(u,\Lambda) = \sum_{m=0}^{L} \sum_{k=-L}^{L} A_{mk}^{ij} \cos(\psi_{mk}) + B_{mk}^{ij} \ \sin(\psi_{mk}) \ , \tag{2.77}$$

with $\psi_{mk} = ku + m\Lambda$. The Fourier coefficients A_{mk}^{ij} and B_{mk}^{ij} are the so-called *lumped-coefficients* A_{mk}^{ij} and B_{mk}^{ij}, which are linear combinations of the potential coefficients:

$$\left.\begin{matrix} A_{mk}^{ij} \\ B_{mk}^{ij} \end{matrix}\right\} = \sum_{l=0}^{L} \frac{GM}{R} \left(\frac{R}{r}\right)^{l+1} \lambda_{lk}^{ij} \, f \left\{\begin{matrix} a_{lm}^{ij} \\ b_{lm}^{ij} \end{matrix}\right. \ , \tag{2.78}$$

where the auxiliary symbols a_{lm}^{ij} and b_{lm}^{ij} contain the potential coefficients $\bar{C}_{lm}$ and $\bar{S}_{lm}$ depending on observation type and the parity of $(l-m)$ according to table 2.2 and equation (2.17). Similarly f stands for the inclination function or the cross-track inclination function. The link between the lumped coefficients and the potential coefficients are the constant transfer coefficients H_{lmk}^{ij}:

$$H_{lmk}^{ij} = \frac{GM}{R} \left(\frac{R}{r}\right)^{l+1} \lambda_{lk}^{ij} \, f \left\{\begin{matrix} a_{lm}^{ij} \\ b_{lm}^{ij} \end{matrix}\right. \ . \tag{2.79}$$

The semi-analytical solution consists of two steps. The first step is the computation of the lumped-coefficients A_{mk}^{ij} and B_{mk}^{ij} by FFT-techniques. They can be obtained again by two different approaches: the 1D-FFT approach (see sec. 2.5.2) and the 2D-FFT approach (see sec. 2.5.1), which is also known as *Torus-Approach*.

The second step is the adjustment of potential coefficients from the lumped-coefficients as pseudo-observables, which leads to a block-diagonal system of normal equations, that can be solved very efficiently. This step is independent of the way the lumped coefficients were obtained (cf. sec. 2.5.3).

The assumption of a circular orbit introduces errors, as a real orbit is perturbed by gravitational and external forces. This will lead to a degraded solution compared to a direct solution. The degradation can be to some extent overcome by an iterative processing strategy, which is explained in section 2.5.4.

2.5.1 2D-FFT Approach

In equation (2.77) the orbit is only dependent on two variables u and Λ. The argument of latitude $u = \omega + \nu$ is the angle between the ascending node and the satellite position in the orbital plane, $\Lambda = \Omega - \theta_g$ is the longitude of the ascending node (cf. fig. 2.2). They both range periodically from 0° to 360° forming a torus, which is the spatial domain of the 2D-Fourier Transform. The orbit can be transformed to the (u, Λ) domain via the Keplerian elements. It can be imagined to be wrapped around a torus. The measurement values can then be interpolated to a regular grid on the torus surface, as shown in Fig. 2.7.

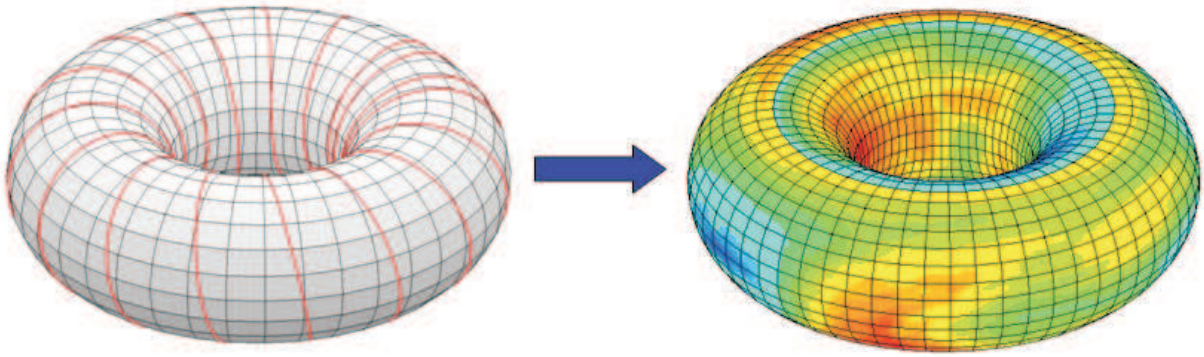

Figure 2.7: Interpolation on a torus.

In addition to the problem, that a real orbit does not have a constant orbit height and observations are evaluated at a *wrong* location, the interpolation from irregular distributed data to a regular grid is an additional error source as well. Hence it is important to choose an interpolation method which minimizes the interpolation error. The method will be chosen by means of results with real data from the CHAMP mission in section 3.3 and with simulated GOCE data in section 4.2.

Furthermore following this approach the GOCE-SGG observations are implicitly assumed to be in the local orbit reference frame (LORF), which means that the x-axis is pointing in flight direction, the z-axis radially outwards and the y-axis is completing the triad. Due to the GOCE-mission design, the actual orientation of satellite and gradiometer – and thus the observed gravity tensor – will differ from the nominal orientation by several degrees (cf. fig. 4.5). It is not possible to simply rotate the tensor to the LORF as the tensor elements with lower accuracy would dilute the more precise ones. As a result, the observations are assumed to be in a slightly different frame, which enters another small error.

A 2D-FFT of the torus grid yields the complex coefficients C_{km}^{ij} (where the indices ij denote the functional which is used). They can be converted to the lumped coefficients A_{mk}^{ij} and B_{mk}^{ij} with the following transformation:

$$
\begin{aligned}
V_{ij}(u,\Lambda) &= \sum_{m=0}^{L}\sum_{k=-L}^{L} A_{mk}^{ij}\cos(\psi_{mk}) + B_{mk}^{ij}\ \sin(\psi_{mk}) \\
&= \sum_{m=0}^{L}\sum_{k=-L}^{L} A_{mk}^{ij}\frac{e^{i\psi_{mk}}+e^{-i\psi_{mk}}}{2} + B_{mk}^{ij}(-i)\frac{e^{i\psi_{mk}}+e^{-i\psi_{mk}}}{2} \\
&= \sum_{m=0}^{L}\sum_{k=-L}^{L} \frac{A_{mk}^{ij}-iB_{mk}^{ij}}{2}e^{i\psi_{mk}} + \frac{A_{mk}^{ij}+iB_{mk}^{ij}}{2}e^{-i\psi_{mk}} \\
&= \sum_{m=0}^{L}\sum_{k=-L}^{L} \frac{A_{mk}^{ij}-iB_{mk}^{ij}}{2}e^{i\psi_{mk}} + \sum_{m=-L}^{0}\sum_{k=-L}^{L} \frac{A_{m|k|}^{ij}-iB_{m|k|}^{ij}}{2}e^{i\psi_{mk}} \\
&= \sum_{m=-L}^{L}\sum_{k=-L}^{L} C_{mk}^{ij}e^{i\psi_{mk}} \quad . \qquad (2.80)
\end{aligned}
$$

It follows, that $A_{mk}^{ij} = 2\Re C_{mk}^{ij}$ and $B_{mk}^{ij} = -2\Im C_{mk}^{ij}$. According to the Nyquist theorem, which states that the highest frequency which can be accurately represented is less than half of the sampling rate, the number of grid points must be at least $(2L \times 2L)$ or the maximum spacing between the grid points be $2 \cdot \frac{360^\circ}{L}$ in order to have a sufficient resolution for a gravity field analysis up to degree/order L.

2.5.2 1D-FFT Approach

As an alternative to the 2D-FFT it is also possible to obtain the lumped coefficients by a 1D-FFT of the measurement series along the orbit. From signal processing theory it is known, that in order to obtain a discrete spectrum it is necessary to have a periodic signal and the line spacing is $\Delta f = 1/T$, where T is the period. To obtain a periodic measurement series, the orbit must be periodic, which means that its groundtrack must close in itself after β revolutions in α nodal days. A nodal day is the interval between two meridian passes of the ascending node. This implies that the ratio of the rates of the orbital coordinates (u, Λ) must match the ratio of revolutions per nodal day:

$$
-\frac{\dot{u}}{\dot{\Lambda}} = \frac{\beta}{\alpha} \quad , \qquad (2.81)
$$

where (cf. Kaula (1966)):

$$
\dot{u} = \dot{\omega} + \dot{\nu} = n + \frac{3}{2}nJ_2\left(\frac{R}{r}\right)^2\left[4\cos^2 I - 1\right] \ , \qquad (2.82)
$$

and

$$
\dot{\Lambda} = \dot{\Omega} - \dot{\theta}_{\mathrm{g}} = -\frac{3}{2}nJ_2\left(\frac{R}{r}\right)^2\cos I - \omega_E \ . \qquad (2.83)
$$

The angular velocity $\dot{u}$ can be interpreted as the mean motion of the satellite $n = \sqrt{GM/r^3}$ corrected for a small J_2 perturbation, while $\dot{\Lambda}$ is simply the combined effect of the Earth rotation ω_E and the J_2-induced precession of the ascending node. It is always negative as the Earth rotation is in any case faster than the nodal precession – hence the negative sign in equation 2.81.

A 1D-FFT of the observation time series produces the one-dimensional Fourier coefficients A_n and B_n, which can be mapped to the two-dimensional lumped coefficients A_{mk} and B_{mk}. According to Sneeuw

(2000), the gravitational potential up to degree and order L creates a signal along the orbit, which has the spectral lines $\dot{\psi}_{mk} = k\dot{u} + m\dot{\Lambda}$ with the spectral resolution $\Delta\dot{\psi} = \dot{u}/\beta$ and the frequency of a certain spectral line as defined by $\dot{\psi}_n = n\Delta\dot{\psi}$. Using the relation in equation 2.81 the 1D and 2D spectra can be related to each other:

$$\dot{\psi}_{mk} = k\dot{u} + m\dot{\Lambda} = \dot{u}\left(k + m\frac{\dot{\Lambda}}{\dot{u}}\right) = \dot{u}\left(k - m\frac{\alpha}{\beta}\right) = \frac{\dot{u}}{\beta}\left(k\beta - m\alpha\right) = \Delta\dot{\psi}\left(k\beta - m\alpha\right) \ . \tag{2.84}$$

So the mapping between the two spectra is defined by the relation:

$$n = k\beta - m\alpha \ , \tag{2.85}$$

which is only unique if α and β have no common denominator. A perfect repeat orbit with a constant repeat-ratio β/α is of course unrealistic and an imperfection of the periodicity condition is an additional error source compared to the 2D-FFT approach. Nevertheless it was shown in Pail and Wermuth (2003) that a non-closure of up to one degree at the equator and data-gaps of up to 30% do not degrade the final solution seriously but are primarily slowing down the rate of convergence of an iterative solution.

2.5.3 Block-Wise Adjustment

Once the lumped coefficients A^{ij}_{mk} and B^{ij}_{mk} are obtained – either by the 1D-FFT or the 2D-FFT approach – they can be converted to the potential coefficients $\bar{C}_{lm}$ and $\bar{S}_{lm}$ by a transformation which is basically an inversion of equation 2.78. It can be regarded as a spectral mapping from the torus-domain to the spherical domain and can be written as least-squares adjustment:

$$\begin{bmatrix} \bar{C}_{lm} \\ \bar{S}_{lm} \end{bmatrix} = \left(\mathbf{H}^{\mathrm{T}}_{lmk}\mathbf{P}_{\psi}\mathbf{H}_{\mathbf{lmk}} + \alpha^2\mathbf{R}\right)^{-1}\mathbf{H}^{\mathrm{T}}_{lmk}\mathbf{P}_{\psi}\begin{bmatrix} A_{mk} \\ B_{mk} \end{bmatrix} \quad , \tag{2.86}$$

where the potential coefficients are the unknown parameters and the lumped coefficients enter as pseudo-observations. The regularization matrix $\mathbf{R}$ is obtained the same way as described in section 2.4. The design matrix $\mathbf{H}_{lmk}$ is composed of the corresponding transfer coefficients. As can be seen in equation 2.78 only lumped coefficients and potential coefficients of the same order m are connected by the transfer coefficients H_{lmk}. Hence the normal matrix becomes block-diagonal and the whole adjustment resolves into independent and much smaller systems of normal equations. Furthermore in each m-block only coefficients with the same parity of l are connected as by definition all $H_{lmk} = 0$ where $(l - k)$ is odd (see definition of inclination functions $\bar{F}_{lmk}(I)$ in section A.2.2). So by using the appropriate ordering of coefficients each m-blocks resolves again into two blocks, where the normal matrix contains at most $(L+1)/2 \times (L+1)/2$ elements. This can be solved very efficiently.

A further advantage of the semi-analytical approach compared to a direct solution is, that filters can be applied in the spectral domain. The residuals after the adjustment (see below) can be taken as approximation for the the true errors of the observations. Hence the power spectral density (PSD) of the residuals is an approximation for the true error PSD. Using the mapping $n = k\beta - m\alpha$, an error estimate for the lumped coefficients A^{ij}_{mk} and B^{ij}_{mk} can be easily found. The data is implicitly filtered by simply entering the reciprocal value of the PSD of the corresponding frequency ψ_{mk} to the diagonal of the weight matrix $\mathbf{P}_{\psi}$. It was shown by Pail et al. (2004) in a simulation study, that the estimate for the true error PSD improves with every iteration and the final estimate deviates by only a few percent.

2.5.4 Iterative Quick-Look Processing

As mentioned above, all deviations from the assumed perfect circular orbit – variations in orbit height and inclination, misalignment of the gravity tensor, non-closure of the repeat orbit and data gaps in case of the 1D-FFT approach – will lead to a degraded solution. This degradation can be overcome to a certain extent – depending on the deviations – by an iterative strategy as shown in figure 2.8.

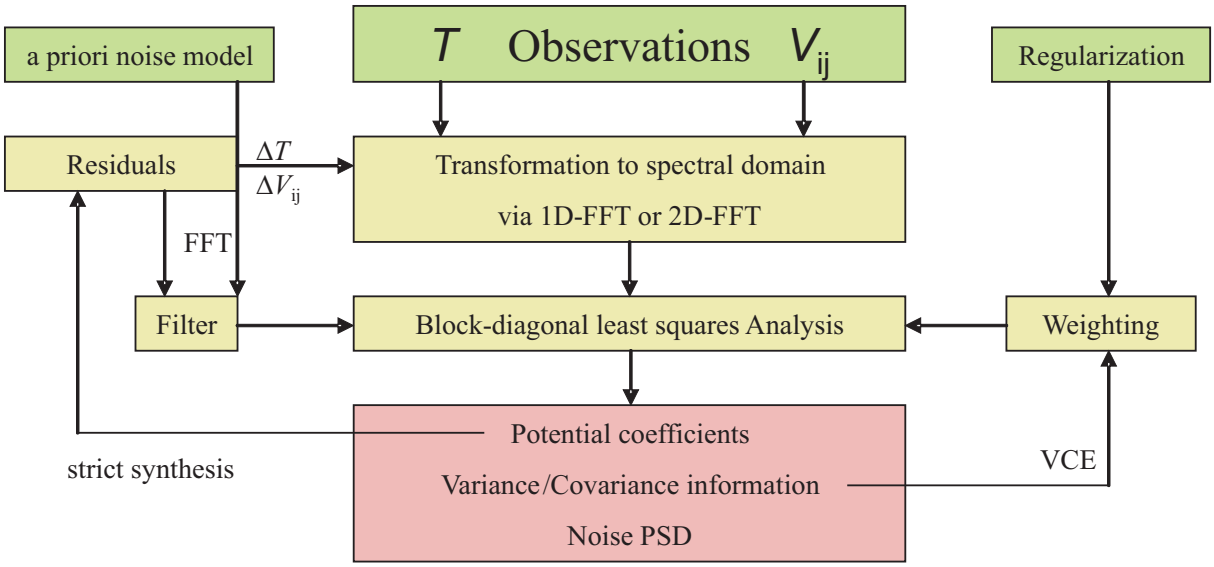

Figure 2.8: Iterative processing scheme.

The set of potential coefficients $\bar{C}_{lm}$ and $\bar{S}_{lm}$ from the initial solution is entered into a strict spherical harmonic synthesis. This means that theoretical values for the observations T and V_{ij} are computed by equation 2.12 at the exact location of the orbit and in case of SGG-observations, the tensor is rotated to its true alignment in the GRF. The residuals ΔT and ΔV_{ij}, which are the difference between the original observations and the theoretical values, enter the whole process again. First they are converted to lumped coefficients ΔA_{mk}^{ij} and ΔB_{mk}^{ij} and then changes to the potential coefficients $\Delta\bar{C}_{lm}$ and $\Delta\bar{S}_{lm}$ are estimated. They are added to the coefficients obtained in the previous iteration, and the iteration is repeated until convergence is achieved, which means that the $\Delta\bar{C}_{lm}$ and $\Delta\bar{S}_{lm}$ stay below a certain threshold, where their impact on the solution can be neglected. Examples will be shown in sections 3.3 and 4.1.

3 CHAMP Gravity Field Analysis

The CHAMP gravity field analysis consists of the two main parts pointed out in chapter 2, namely a linearization step and a solution step. In this work the linearization is done by computing a time series of disturbing potential values along the orbit using the energy balance approach, which is described in section 3.1. The solution, namely the computation of spherical harmonic potential coefficients from this time series can be done either in a direct least squares adjustment as described in section 3.2 or by an iterative approach. Although the disadvantages of the direct solution, like large requirements in computation time and computer memory, are not as severe as for the GOCE-mission (due to the lower resolution and lower sampling rate), the application of the semi-analytical approach on CHAMP-data is realized in section 3.3, as valuable conclusions can be drawn for the preparation of the GOCE gravity field analysis. To assess the quality of the gravity field solution, the results are validated in section 3.4 by a comparison with other gravity field solutions and with external data.

3.1 Energy Balance Approach

3.1.1 Data Preparation

For this study 2 years of CHAMP data from day 70/2002 to day 70/2004 have been used. The main data sets are the orbits and the onboard instrument data. Reduced-dynamic and kinematic orbit solutions computed by Švehla and Rothacher (2004) have been used at the given sampling rate of 30 s. The instrument data in the CH-OG-2-ACC+ product provided by GFZ (cf. Förste (2002)) contains accelerations from the onboard accelerometer in the satellite fixed frame and quaternions measured by the star-trackers, which describe the rotation from the satellite fixed frame to the inertial frame. Both data sets are given at a 10 s sampling; thus they have to be downsampled to 30 s to match the orbit data.

The orbit altitude varies between 420 km and 370 km at the beginning of the data period and slowly descends (see fig. 3.1). The band structure in the figure is caused by the height variation during each revolution due to the eccentricity. Two maneuvers lifted the satellite and during the second maneuver the eccentricity was modified, which results in a smaller height variation during each revolution. At the end of the two-years period, the satellite descended to about 370 km orbit height.

Figure 3.2 shows the differences between the two orbit types for DOY 198/2002. It can be seen, that the difference contains many jumps, outliers and short data gaps which have their origin mainly in the kinematic orbit. The reduced-dynamic orbit is much smoother and contains no data-gaps except for 21 days of data which are completely missing (which is about 2.9% of the data), while the kinematic orbit contains many short and various longer gaps (which is about 5.9% of the data). This is due to the fact, that during periods with bad GPS observations or even complete signal losses, the reduced-dynamic orbit is simply continued by the integration of modeled forces (c.f. sec. 2.2). Therefore the reduced-dynamic orbit can be used as a reference orbit for outlier detection in the kinematic orbit. Whenever the difference between those orbits exceeds a certain threshold (e.g. 3σ), the kinematic position is flagged as outlier. In case of a phase break a jump in the difference of the two orbits occurs. The kinematic orbit is consistent before and after the jump, but the velocity must not be derived over the jump, as it would get a wrong value. So the jump has to be flagged, and the orbit is cut into two arcs. This strict outlier detection results in 38.3% of the kinematic orbit being flagged. This is a large loss of redundancy

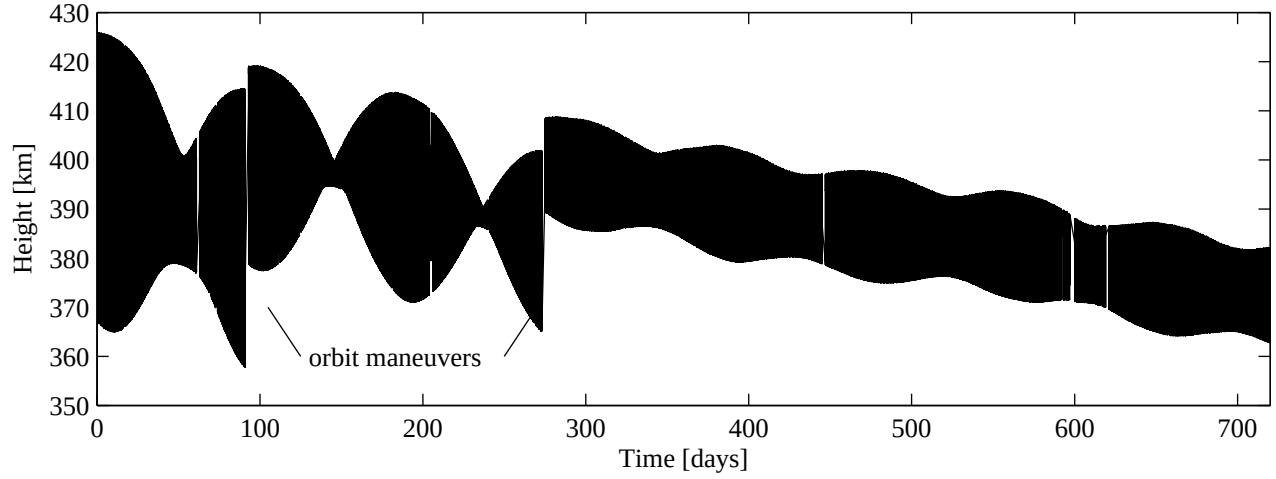

Figure 3.1: Orbit height.

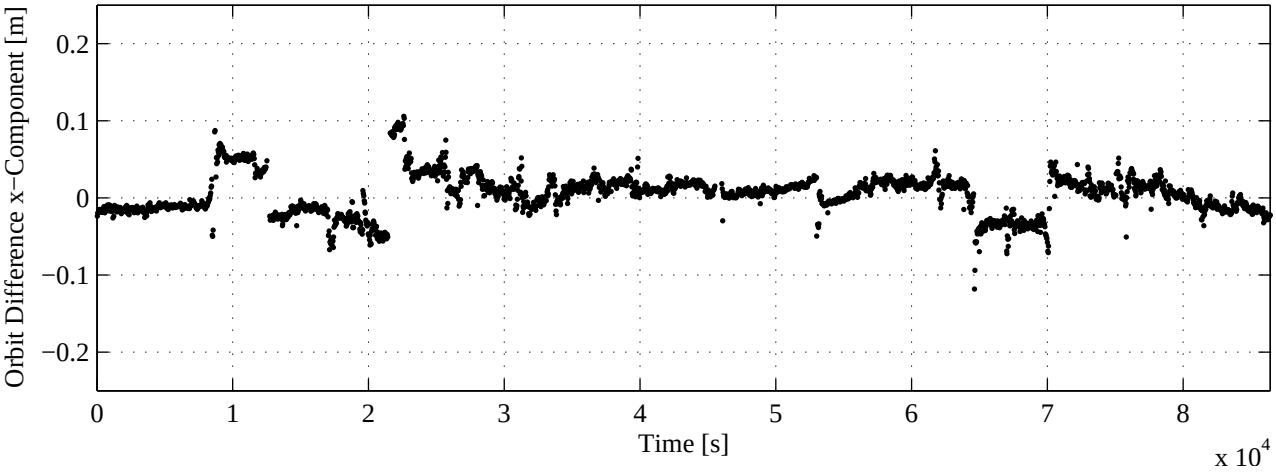

Figure 3.2: Difference between reduced-dynamic and kinematic orbit (x-component) for DOY 198/2002.

and continuity, which could possibly be avoided by a manual outlier detection, but this procedure was designed to work automated on large data sets.

The star-tracker and accelerometer data are given at 10 s sampling and contain about 4.8% of gaps. The specified accuracy for the accelerations is $3 \cdot 10^{-9}\,\mathrm{m/s^2}$ for the along-track and cross-track axis and $3 \cdot 10^{-8}\,\mathrm{m/s^2}$ for the radial axis. When the accelerations are rotated to the inertial system using the quaternions obtained by the star-trackers, the component with lower accuracy will impair the good ones. The accelerations are downsampled to 30 s to match the orbit sampling rate using a lowpass FIR filter. Downsampling by simply taking every third value would correspond to a multiplication of the data with a series of Dirac impulses, and thus to a convolution of the spectrum with a series of Dirac-impulses, which could lead to undesired aliasing effects. So a fourth-order lowpass FIR filter with a cutoff frequency of 30s was designed using the MATLAB function `fir1`:

$$a_i = 0.01688334a_{i-2} + 0.227925079a_{i-1} + 0.51038316a_i + 0.227925079a_{i+1} + 0.01688334a_{i+2}\ . \quad (3.1)$$

As a negative side-effect the percentage of data gaps would increase to about 7.2% due to the warm-up phase of the filter. To compensate this, the short gaps of up to 100 s are closed by a Newton-Gregory interpolation (cf. sec. A.1) before the filter is applied. This reduces the gaps to about 4.5% of the data,

mainly eliminating the majority of very short gaps which are responsible for a strong fragmentation of the data set. It was found out in an empirical test that for a gap length of 100s the interpolation error using a 8-point Newton-Gregory interpolation with 4 points on each side of the gap, is well below the $3 \cdot 10^{-8}\,\mathrm{m/s^2}$ accuracy of the radial accelerometer axis.

The nominal orientation of the satellite is along the flight path, which means that the spacecraft-fixed reference frame coincides with the local orbit reference frame (LORF), and its x-axis points in the direction of the velocity vector. In reality the spacecraft fixed frame deviates from the nominal orbit frame, as external forces also cause angular accelerations on the satellite. The attitude control tries to keep the deviation below a certain threshold by firing thrusters to keep the satellite aligned. The thrusters are placed in six pairs to generate positive and negative rotational accelerations around all three axes, and thus allow for a quite precise attitude control. It can be seen in figure 3.3 that the deviation from the nominal attitude rarely exceeds 2°. It becomes also clear, that many thruster pulses coincide with the peaks in the deviation angle, which shows, that thrusters are fired to align the satellite back closer to its nominal orientation.

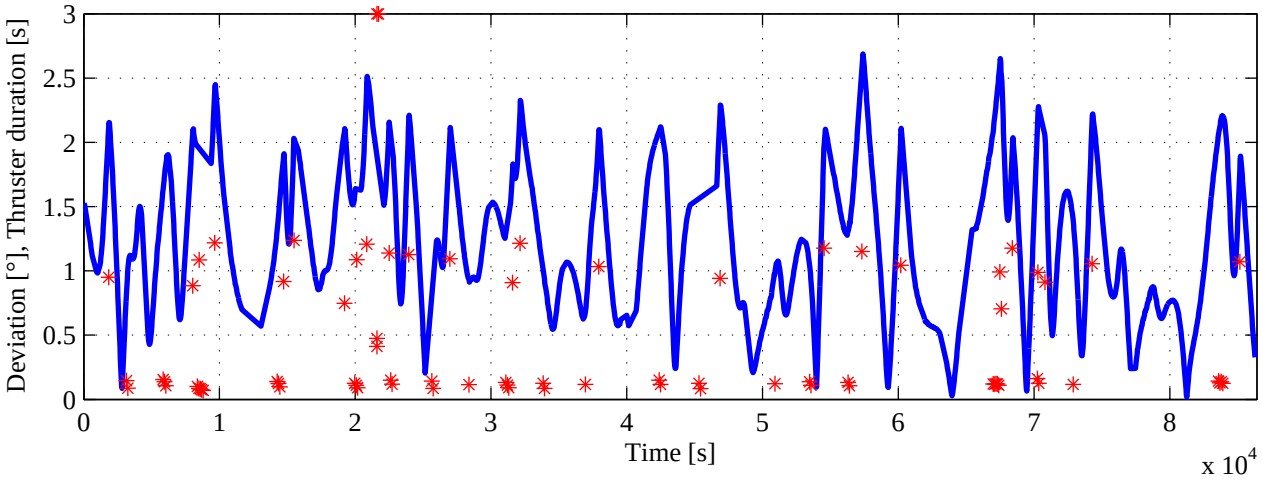

Figure 3.3: Deviation from nominal attitude (blue) and thruster pulses (stars) for DoY 198/2002.

3.1.2 Velocity Computation

In order to asses which of the velocity computation methods described in section A.1 is best suited for the derivation of velocities from kinematic CHAMP orbits, they are tested on a simulated orbit, for which velocities are exactly known. The simulation is done for a one-day CHAMP-like orbit, containing only gravitational forces from an a priori field up to degree and order 360. The positions and velocities are error free. The tested differentiation methods are the FIR-filters, which are derived from interpolating polynomials over an odd number of samples in section A.1. As discussed in section A.1 a polynomial of the order (n-1) is necessary to describe n samples. Due to the symmetry of the problem all even orders are canceled out and a polynomial of the order (n-2) is sufficient. If the order of the polynomial is lower than n-2, it is over-determined and the derived filter starts smoothing the signal. In tables 3.1, 3.2 and 3.3 the results for non-smoothing filters are listed on the diagonal, the smoothing ones are listed below.

The derived velocities can be compared to the simulated velocities to determine the error of the derivation. In a rough approximation one can state, that the velocities should have an RMS error of 0.5 mm/s or better to meet the pre-mission requirement of a geoid error of several decimeters. Error propagation yields the potential error $\delta T = \dot{\mathbf{r}}_0 \cdot \delta\dot{\mathbf{r}}$. Assuming a mean velocity $\dot{\mathbf{r}}_0$ of 7650 m/s and a velocity error $\delta\dot{\mathbf{r}}$ of 0.5 mm/s, the error of the disturbing potential δT is $3.825\,\mathrm{m^2s^2}$, which corresponds to a geoid error of about 40 cm at satellite height. Therefore velocity computation methods which cannot meet the requirement of 0.5 mm/s should be ruled out.

The errors from the non-smoothing methods are shown in figure 3.4, and the RMS error for all tested methods is displayed in table 3.1. It can be seen, that first-order filters are not suitable for velocity derivations, as the error is way above the required 0.5 mm/s. Obviously a first-order polynomial is not suited to approximate the orbit over 30s during which the satellite moves more than 200 km. The error for the third-order polynomial is already below 0.1 mm/s but the error curve shows a strong periodic signal with the orbit revolution frequency. This shows, that also a third-order polynomial is not good enough to approximate the dominant oscillation in the orbit. So at least a polynomial of fifth-order is necessary for the velocity derivation. As can be seen in table 3.1 the accuracy of the non-smoothing methods (which are on the diagonal of the table) is increasing with polynomial order. The smoothing methods (which can be found below the diagonal) perform the worse, the stronger the applied smoothing is.

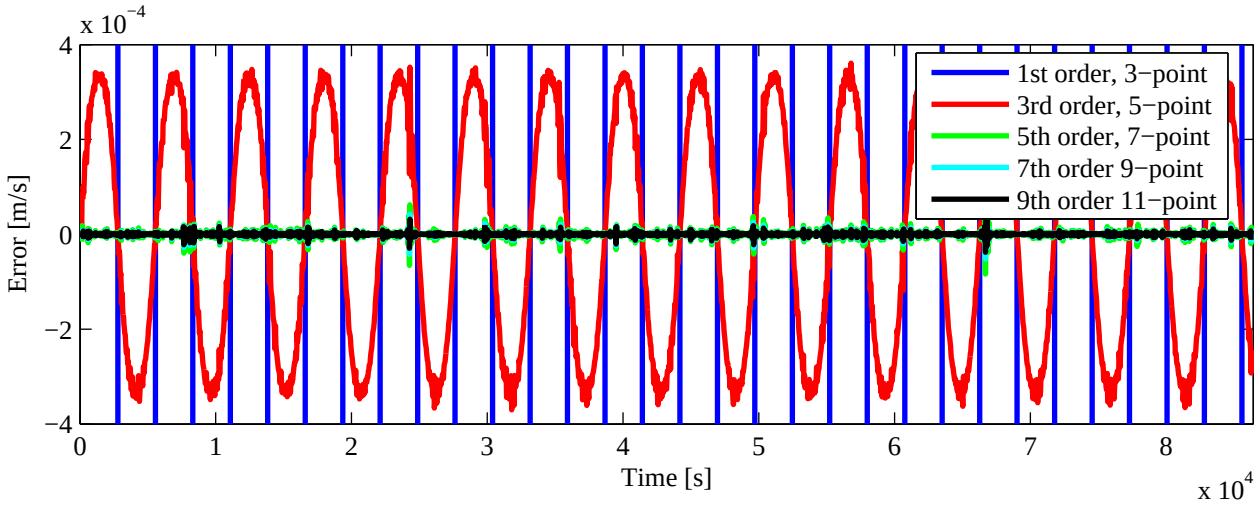

Figure 3.4: Size of errors of several non-smoothing velocity computation methods (error-free orbits).

Table 3.1: RMS errors [mm/s] of the derived velocities. Non-smoothing methods are on the diagonal, smoothing methods below.

points order	1^{st}	3^{rd}	5^{th}	7^{th}	9^{th}	11^{th}
3	224.244					
5	762.318	0.050				
7	1569.119	0.312	0.0009			
9	2644.267	0.993	0.0046	0.0005		
11	3987.249	2.380	0.0119	0.0026	0.0004	
13	5597.425	4.826	0.0234	0.0067	0.0017	0.0003

It can be seen that for an error-free simulation no smoothing is required. Therefore the test was repeated taking a white noise error of $\sigma = 1.5$ cm per component added to the positions, which is assumed to be the error-level of the kinematic orbit obtained by comparisons with other orbit types (cf. Švehla and Rothacher (2004)). The result, which can be seen in table 3.2 and for some selected methods in figure 3.5, shows that for the case with noise, the smoothing methods perform better than the non-smoothing ones, and the one which uses a fifth-order polynomial over 11 points performs best.

Of course white noise does not really reflect the true error behavior of kinematic orbits. Thus a third test was carried out, in which kinematic positions of one selected day of the real CHAMP-data are derived and compared to the velocities of the reduced dynamic orbit, which serves as a reference as it is considered less noisy. However it should be kept in mind, that the reduced dynamic velocities

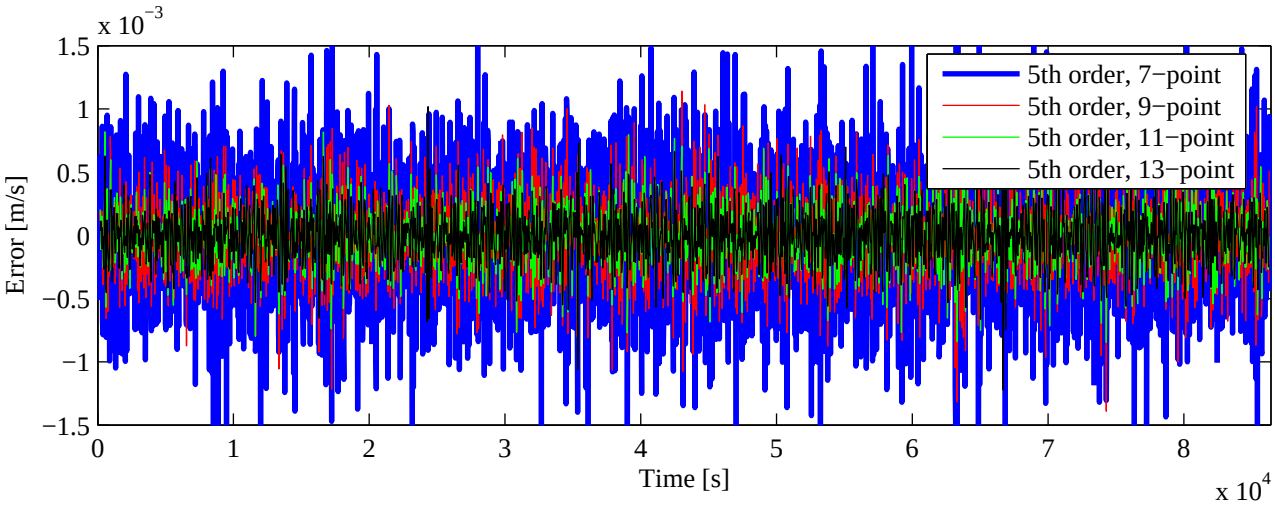

Figure 3.5: Errors of several fifth-order velocity derivation methods (white noise case).

Table 3.2: RMS errors [mm/s] of the derived velocities with white noise added to the positions.

points order	1^{st}	3^{rd}	5^{th}	7^{th}	9^{th}	11^{th}
3	224.245					
5	762.318	0.475				
7	1569.120	0.404	0.536			
9	2644.267	1.008	0.324	0.577		
11	3987.250	2.382	0.229	0.374	0.606	
13	5597.425	4.827	0.175	0.274	0.413	0.627

from numerical integration are as well based on polynomials which are fitted to the observations. The resulting errors are displayed in table 3.3. Also in this test the smoothing methods perform better than the non-smoothing ones, and again the fifth-order polynomials perform best.

Table 3.3: RMS differences [mm/s] of the derived kinematic velocities with reduced dynamic velocities.

points order	1^{st}	3^{rd}	5^{th}	7^{th}	9^{th}	11^{th}
3	746.758					
5	2538.885	0.257				
7	5226.486	1.138	0.195			
9	8808.545	3.600	0.148	0.205		
11	13283.592	8.619	0.127	0.160	0.212	
13	18649.695	17.475	0.125	0.137	0.169	0.218

But the RMS error is not a conclusive criterion as it is only one number for the whole error spectrum. It was mentioned above, that the velocity derivation with polynomials corresponds to a convolution of a filter expression with the orbit time series in the time domain. In the frequency domain it is a multiplication of the spectrum of the filter with the spectrum of the orbit. Thus the magnitude frequency response – which specifies the amplitude gain that the filter provides at each frequency – of different filters is compared in figure 3.6. It can be seen, that the magnitude frequency response of all

polynomial filters is very close to the $i\,\omega$-line for low frequencies, but it starts to drop rapidly at a certain cut-off frequency. The non-smoothing filters have a higher cut-off frequency and the transition to the stop-band is steeper. The higher the polynomial degree is, the higher is the cut-off frequency and the closer the filter gets to an $i\,\omega$-behavior. The over-determined polynomial methods have a much lower cut-off frequency and a slower drop. After the first drop there are some oscillations in the frequency response, which are called stop-band ripple. The larger the over-determination is, the lower is the cut-off frequency and the more oscillations can be counted in the stop band.

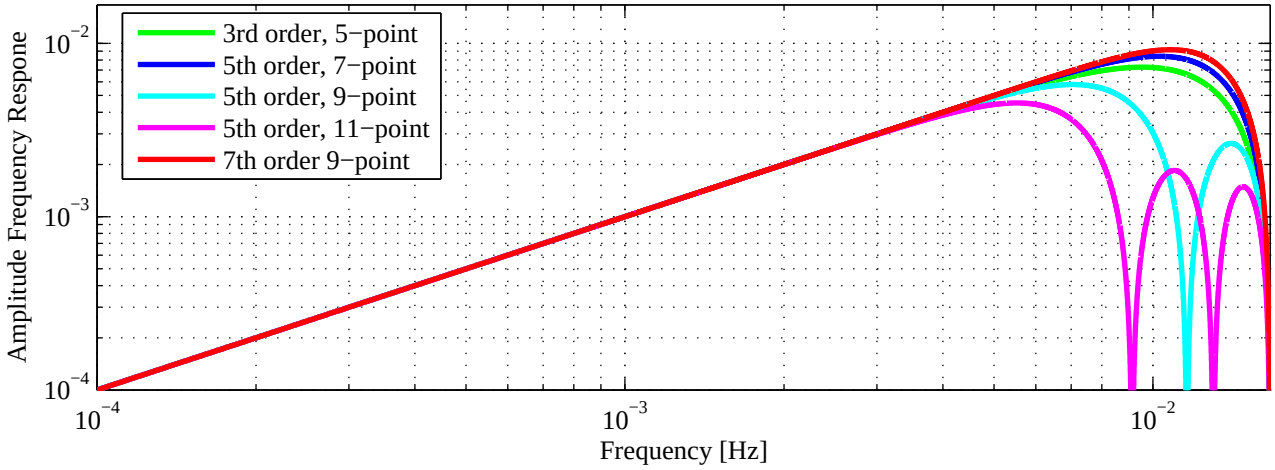

Figure 3.6: Magnitude frequency response of polynomial differentiators.

In order to determine the optimal cut-off frequency the PSDs of the kinematic orbit and their error should be compared. But as the *true* orbit is unknown, the orbit error and the error PSD cannot be computed. According to Švehla and Rothacher (2004) and Jäggi et al. (2006), kinematic positions are not independent but show correlations of up to 30 – 40 minutes, which is the time that CHAMP tracks a single GPS satellite and estimated phase ambiguities are valid. Adjacent epochs share the same systematic effects, as a similar GPS constellation is observed. So the best empirical estimate of an error PSD of the kinematic orbit, for wavelengths of 30 minutes and shorter, can be obtained by comparing it to the reduced-dynamic orbit and computing the PSD from the difference between the two orbits, as the reduced-dynamic orbit is considered to have a very small error in these high frequencies.

Figure 3.7 shows the signal of an error-free simulated CHAMP-like orbit (blue curve) and an empirical estimate of the error of the kinematic orbit (red curve). The intersection of the two curves, which marks the frequency, where the signal-to-noise ratio becomes 1 is at about $9 \cdot 10^{-3}$ Hz. So the aim should be to have a cut-off close to this frequency in order to preserve the signal on the one hand and to filter out the noise on the other hand. If this is compared to the magnitude frequency response of the different filters in figure 3.6, one can clearly see, that the cut-off frequency of the over-determined methods is too low and orbit signal is filtered out, which will result in a loss of high-frequency gravity field signal. So the non-smoothing methods seem to be better suited for gravity field determination - even though the RMS error is larger – as the spectral distribution of the error is better. Thus judging from both criteria the fifth-order polynomial derivation over 7 points is chosen for velocity derivation. This will be confirmed by the results of the gravity field analysis in section 3.2 but is only valid for this particular mission scenario. A variation in orbit height (and thus signal strength), orbit error level or sampling interval will shift the optimal cut-off frequency and may lead to a different conclusion.

3.1.3 Modeling of Disturbing Potential

The potential of the kinetic energy $W_{\text{kin}} = 1/2\,\dot{\mathbf{r}}^2$ is computed from the velocities and displayed in figure 3.8 (blue curve). For comparison, also the normal potential U computed from the parameters

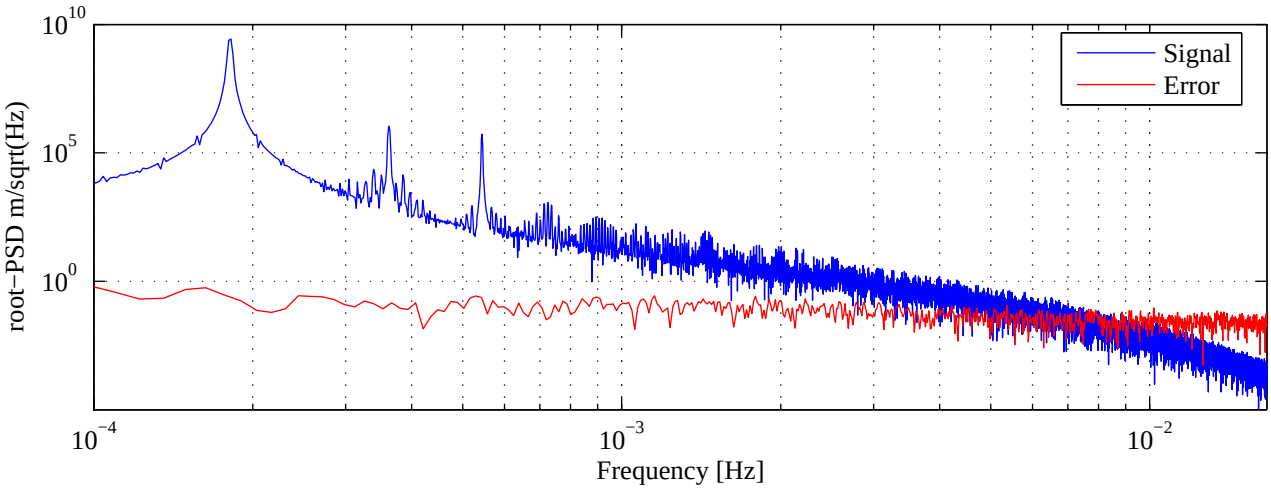

Figure 3.7: PSD of simulated kinematic orbits and their estimated errors.

of the WGS84 ellipsoid is displayed (red curve). Both show a similar behavior but with an apparently different slope. In addition, they are strongly anti-correlated to the orbit height (cf. fig. 3.1), as both the normal potential and kinetic energy increase when the satellite loses height and potential energy.

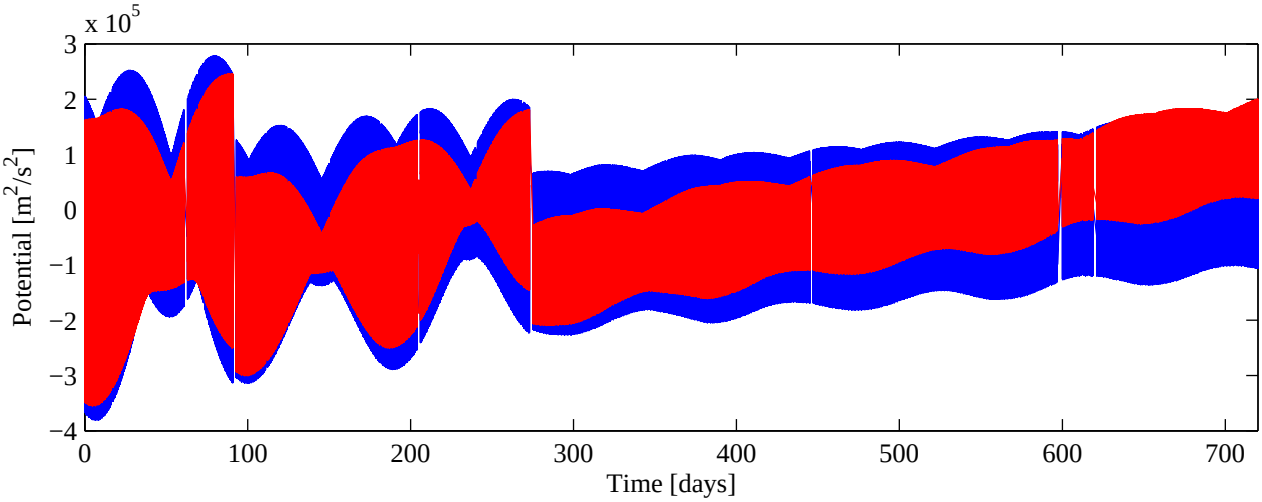

Figure 3.8: Kinetic potential (blue) and normal potential (red).

If one computes the difference between the two potentials, the slope becomes clear, which is superimposed by an oscillation with orbit frequency (cf. fig. 3.9 (blue curve)). This oscillation of about $1.2 \cdot 10^5\,\mathrm{m}^2/\mathrm{s}^2$ comes from the centrifugal potential, which is displayed by the red curve.

The equation:

$$T = \frac{1}{2}\dot{\mathbf{r}}_\mathrm{e}^2 - U - \frac{1}{2}\left(\boldsymbol{\omega} \times \mathbf{r}_\mathrm{e}\right)^2 - C \tag{3.2}$$

would be valid for a rotating conservative potential without external or non-conservative forces. The disturbing potential T displayed in figure 3.10 (blue curve) clearly shows a loss of energy. Comparing the red curve, which shows the measured accelerations integrated along the orbit, the loss of energy can be explained to a large extent. Due to the non-conservative surface forces $\mathbf{a}_\mathrm{s}$ (like atmospheric friction) the satellite is slowed down and kinetic energy is converted to heat. Although the curves are very similar, the two orbit maneuvers, which add energy to the system by lifting the satellite to a higher altitude, are not modeled correctly (probably due to the accelerations caused by the thrusters exceeding

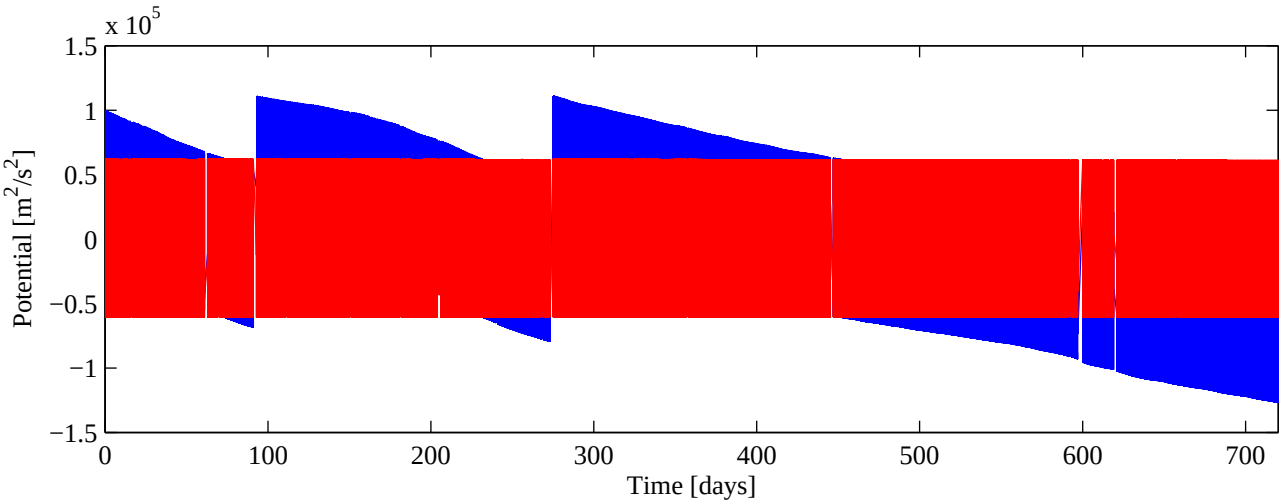

Figure 3.9: $T = 1/2\,\dot{\mathbf{r}}_e^2 - U$ *(blue) and* $W_{\text{cent}} = 1/2(\boldsymbol{\omega} \times \mathbf{r}_e)^2$ *(red).*

the usual measurement range). In addition, the slope of the two curves differs slightly especially during the second half of the displayed period.

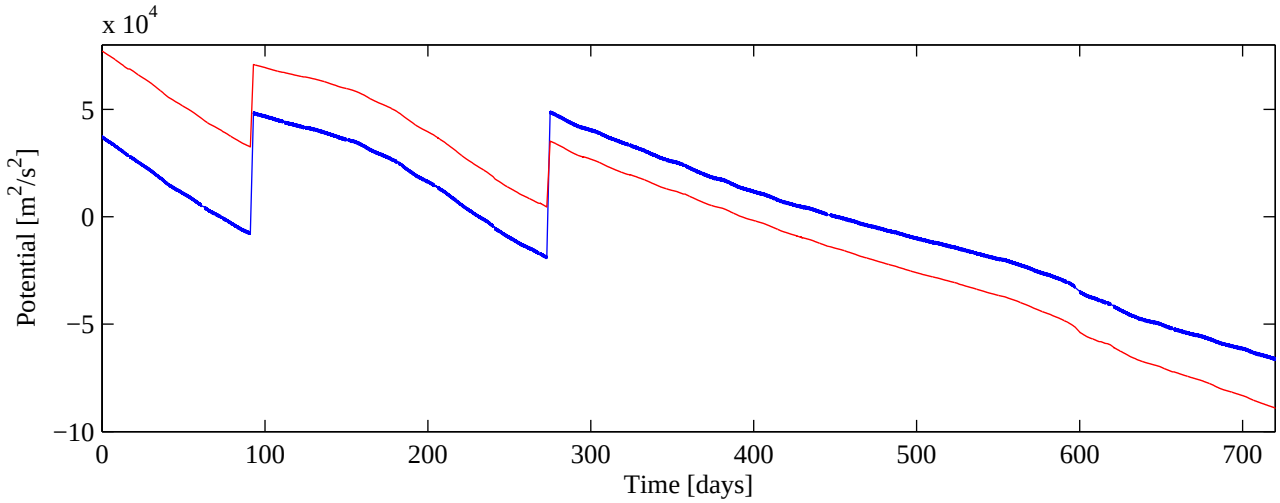

Figure 3.10: $T = 1/2\dot{\mathbf{r}}_e^2 - U - 1/2(\boldsymbol{\omega} \times \mathbf{r}_e)^2$ *(blue) and* $W_s = \int \mathbf{a}_{se} \cdot d\mathbf{r}_e$ *(red).*

After subtracting the integrated measured accelerations from the disturbing potential, one can see that the remaining time series is (apart from jumps and drifts) superimposed by a signal of two frequencies (see fig. 3.11 blue curve). This signal can be identified as the integrated tidal accelerations displayed in the red curve. The signal with shorter wavelength ($\sim$ 12 days) is caused by the direct tides of the moon and the longer one ($\sim$ 120 days) is caused by the direct tides of the sun. The frequencies do not match the revolution periods of the celestial bodies, which is due to the fact, that the resulting signal is a superposition of the revolution period, Earth rotation and satellite revolution period.

Now that all model effects have been accounted for the disturbing potential time series still contains jumps and drifts, as can be seen in figure 3.12. The jumps occur basically after each data gap. When either the information about the satellites position or the external accelerations is missing (or both), the loss of energy due to friction cannot be computed and a new energy constant C has to be introduced for each segment of continuous data.

Table 3.4 summarizes the signal sizes of the various quantities. If the signals are compared to the residuals after adjustment (cf. sec. 3.2), one can see that starting from a potential signal of $2.9{\cdot}10^7\,\mathrm{m}^2/\mathrm{s}^2$ the gravity signal could be extracted with an accuracy of $\sigma = 1.1\,\mathrm{m}^2/\mathrm{s}^2$.

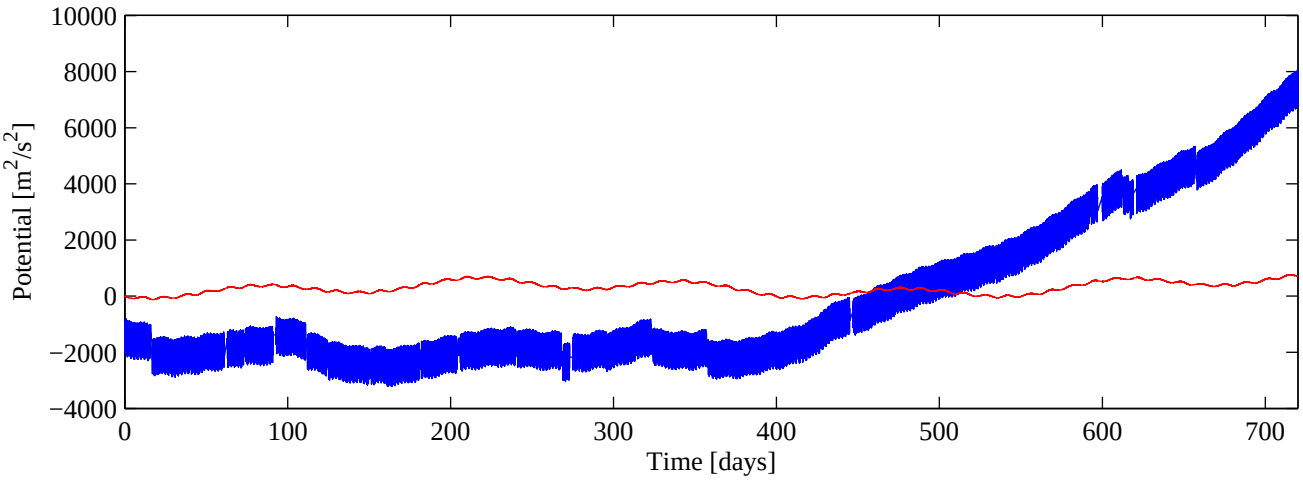

Figure 3.11: $T = 1/2\,\dot{\mathbf{r}}_e^2 - U - 1/2(\boldsymbol{\omega} \times \mathbf{r}_e)^2 - \int \mathbf{a}_{se} \cdot d\mathbf{r}_e$ *(blue) and* $W_t = \int \mathbf{a}_{te} \cdot d\mathbf{r}_e$ *(red).*

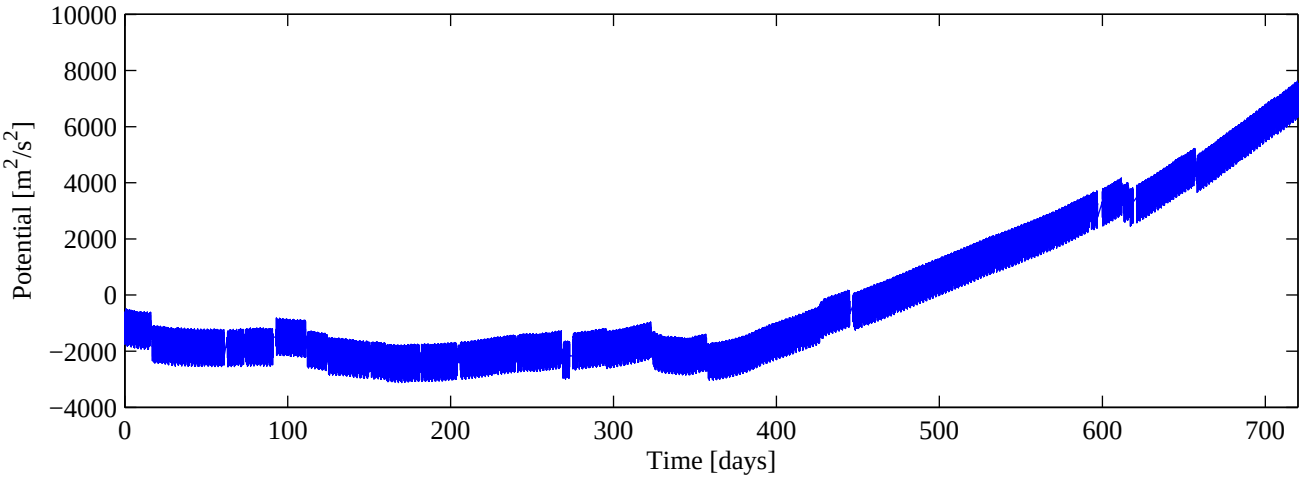

Figure 3.12: $T = 1/2\,\dot{\mathbf{r}}_e^{\,2} - U - 1/2(\boldsymbol{\omega} \times \mathbf{r}_e)^2 - \int (\mathbf{a}_{se} + \mathbf{a}_{te}) \cdot d\mathbf{r}_e$.

Table 3.4: Potential sizes of various effects.

effect		signal
kinetic energy	$1/2\dot{\mathbf{r}}^2$	$2.9 \cdot 10^7 \pm 3 \cdot 10^5\,\mathrm{m}^2/\mathrm{s}^2$
normal potential	U	$5.8 \cdot 10^7 \pm 3 \cdot 10^5\,\mathrm{m}^2/\mathrm{s}^2$
unknown constant	C	$2.9 \cdot 10^7\,\mathrm{m}^2/\mathrm{s}^2$
centrifugal potential	$(\boldsymbol{\omega} \times \mathbf{r}_e)^2$	$\pm 5 \cdot 10^4\,\mathrm{m}^2/\mathrm{s}^2$
surface forces	$\int \mathbf{a}_{se} \cdot \mathrm{d}\mathbf{r}_e$	$\pm 1 \cdot 10^5\,\mathrm{m}^2/\mathrm{s}^2$
temporal variations	$\int \mathbf{a}_{te} \cdot \mathrm{d}\mathbf{r}_e$	$400\,\mathrm{m}^2/\mathrm{s}^2$
systematic instr. errors		$8000\,\mathrm{m}^2/\mathrm{s}^2$
disturbing potential	T	$1000\,\mathrm{m}^2/\mathrm{s}^2$
residuals	σ_0	$1.1\,\mathrm{m}^2/\mathrm{s}^2$

3.1.4 Treatment of Systematic Effects

As can be seen in figure 3.12 there are not only jumps in the energy constant after data gaps, but also drifts in the potential time series, which change after data gaps. This points to uncompensated

accelerometer errors which sum up by integration. It is also likely that some of the events which cause a data gap (like software updates or reboots) change the accelerometer characteristics and are responsible for a changing drift behavior. Two different calibration methods are discussed here. One possibility is to use an a priori model in order to determine the long wavelength error signal in the disturbing potential and to correct for it. If the goal is to derive a gravity field without any a priori gravity field information, an alternative is to estimate additional accelerometer calibration parameters in the adjustment.

Long Wavelength Errors: The idea behind this method is a remove restore technique. From a known gravity model (e.g. EGM96) a disturbing potential time series is computed along the orbit by spherical harmonic synthesis (equ. 2.11) and subtracted from the actual potential time series derived by the energy balance approach. Then the long wavelength signal is removed from the difference either by filtering or by estimating a long wavelength polynomial. After that the potential from the a priori series is added back. It should be noted, that this procedure is carried out for each segment of continuous data separately and has to be interrupted at data gaps. But by relating the potential time series to a known gravity field, the unknown energy constant H and the unknown jumps after data gaps are implicitly removed. Additionally the potential is constrained to the reference frame of the a priori model, as the coefficients of degrees $l = 0$ and $l = 1$ obtain values close to zero.

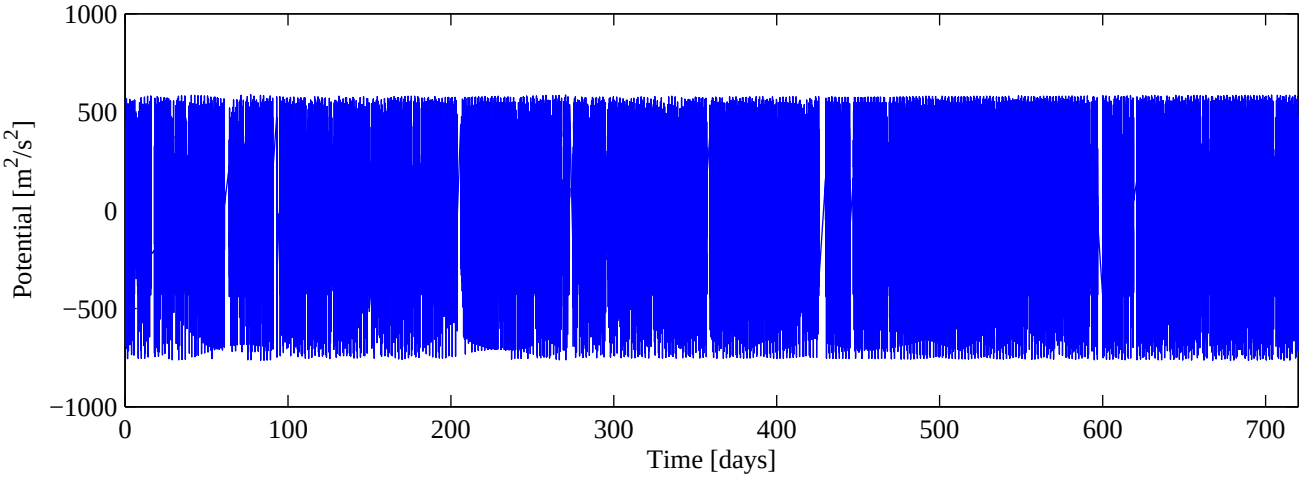

Figure 3.13: Disturbing potential T.

It was determined empirically, that the best solution is obtained, when a polynomial of seventh order is fit to a moving window of about 300 samples ($\sim$ 2.5 hours). Unfortunately using a polynomial of this order will influence wavelengths that are shorter than one orbit revolution ($\sim$ 1.5 hours) an thus the solution of gravity field coefficients of low degree and order. The fact that the disturbing potential will be influenced by the choice of the a priori model (regardless whether this effect is desired or not) is best shown by comparing the resulting disturbing potential time series in case different a priori models were used. The difference between using EGM96 and EIGEN-GL04C, both up to degree and order 360 is shown in Figure 3.14.

Additional Parameters: In order to estimate accelerometer parameters, a separate bias b and scale factor s is assumed for each accelerometer axis:

$$\mathbf{a}_{\mathrm{sc}} = \begin{pmatrix} s_1 \\ s_2 \\ s_3 \end{pmatrix} + \begin{pmatrix} b_1 a_1 \\ b_2 a_2 \\ b_3 a_3 \end{pmatrix} . \tag{3.3}$$

If this is rotated from the spacecraft system (denoted by the index "sc") to the inertial frame and entered into equation 2.36:

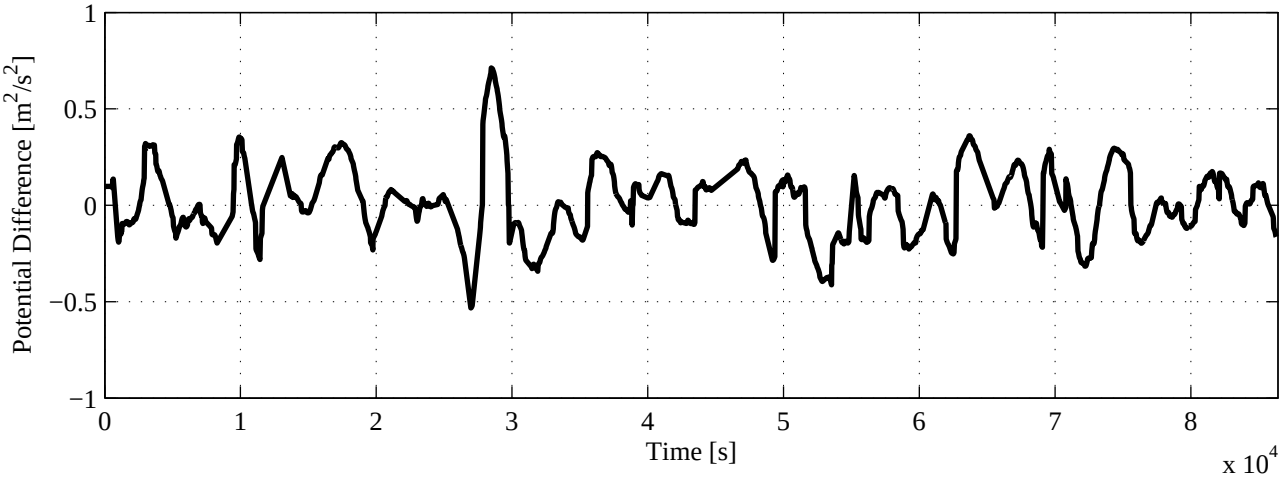

Figure 3.14: Potential difference when using different a priori models for removal of long wavelength errors for DOY 198/2002.

$$V_{\text{non}} = \int_t \mathbf{R}^{\text{sc}}_{\text{i}} \mathbf{a}_{\text{sc}} \cdot \dot{\mathbf{r}}_{\text{i}} \mathrm{d}t + \int_t \mathbf{R}^{\text{sc}}_{\text{i}} \mathbf{a}_{\text{sc}} \cdot (\omega \times \mathbf{r}_{\text{i}})\, \mathrm{d}t \ . \tag{3.4}$$

one can derive the partial derivatives of the disturbing potential w.r.t. the accelerometer parameters:

$$\frac{\partial T}{\partial b_i} = \int (R_{1,i}\dot{x} + R_{2,i}\dot{x} + R_{3,i}\dot{x})\, \mathrm{d}t + \int (R_{1,i}(\omega_2 z - \omega_3 y) + R_{2,i}(\omega_3 x - \omega_1 z) + R_{3,i}(\omega_1 y - \omega_2 x))\, \mathrm{d}t \tag{3.5}$$

and

$$\frac{\partial T}{\partial s_i} = \int (R_{1,i}\dot{x} + R_{2,i}\dot{x} + R_{3,i}\dot{x})\, a_{\text{sc},i} \mathrm{d}t + \int (R_{1,i}(\omega_2 z - \omega_3 y) + R_{2,i}(\omega_3 x - \omega_1 z) + R_{3,i}(\omega_1 y - \omega_2 x))\, a_{\text{sc},i} \mathrm{d}t \ . \tag{3.6}$$

In both equations the first term is the dominant part. The partial derivatives w.r.t. the bias are basically the integral over a scalar product between the unit vectors of the accelerometer axes with the satellites velocity vector. As mentioned before, the x-axis of the accelerometer is aligned close to the velocity vector (cf. fig. 3.3), the norm of the velocity is multiplied with a number close to 1 for the x-bias and a small number for the y- and z- biases. This is reflected in figure 3.15, which shows that the partial derivative w.r.t. the x-bias is almost linear over continuous arcs, and the other components are smaller. This leads to the conclusion, that on the one hand the energy balance approach is not very sensitive to the y- and z-axes of the accelerometer and their errors. This is positive as the z-axis, which has already degraded accuracy, is known to have a hardware problem and delivers even more inaccurate measurements (cf. Förste (2002)). On the other hand the biases of those two components are hard to determine in a least squares adjustment as they are weakly defined, and they obtain unrealistically large values as they compensate other unknown effects.

If one looks at the correlation matrix of the 3 biases and the 3 scale factors in table 3.5, it becomes apparent, that like in many other geodetic applications, bias and scale factor are highly correlated (or anti-correlated) and thus not easily separable. The system of normal equations becomes ill-conditioned if one tries to estimate all six parameters. As the x-bias is the only parameter, which can be estimated in a meaningful way – and its influence on the disturbing potential is almost linear over short arcs – the following strategy has proven to be practicable. The orbit is cut into short arcs (meaning shorter

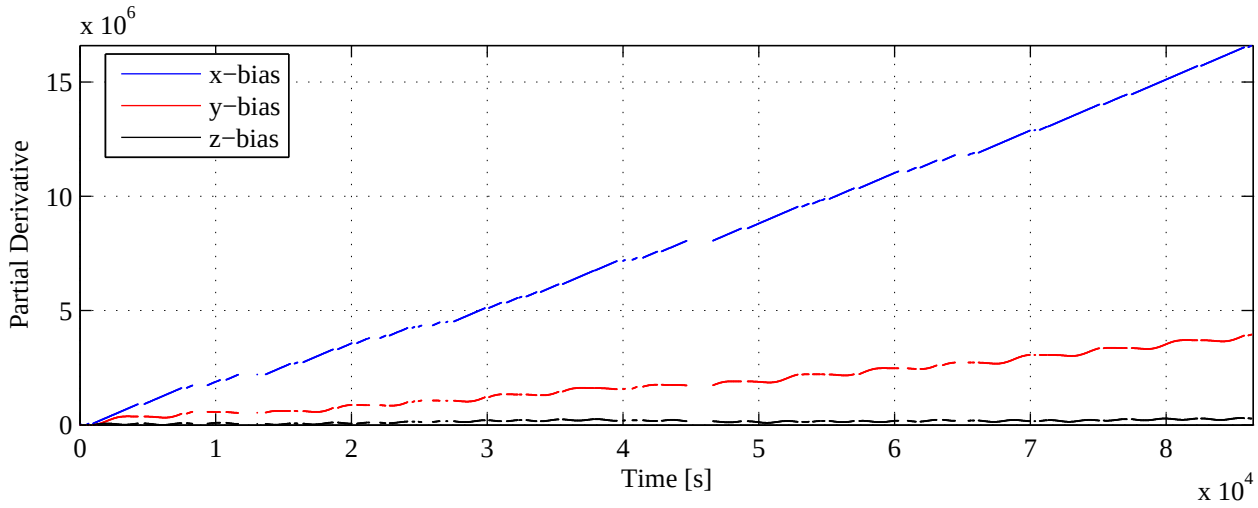

Figure 3.15: Partial derivative of disturbing potential T w.r.t. the accelerometer biases.

than one orbit revolution) and an offset and a linear drift parameter in the disturbing potential are estimated. The offset compensates the unknown jumps in the energy constant after data gaps, the linear drift parameter compensates integrated errors form the x-axis of the accelerometer.

Table 3.5: Correlation matrix of bias and scale factor parameters.

	x-bias	y-bias	z-bias	x-scale	y-scale	z-scale
x-bias	1.00	0.68	0.17	-0.99	0.78	-0.92
y-bias	0.68	1.00	0.34	-0.70	0.98	-0.44
z-bias	0.17	0.34	1.00	-0.22	0.32	0.16
x-scale	-0.99	-0.70	-0.22	1.00	-0.79	0.90
x-scale	0.78	0.98	0.32	-0.79	1.00	-0.55
z-scale	-0.92	-0.44	0.16	0.90	-0.55	1.00

3.2 Direct Solution

The second part of the CHAMP gravity field analysis is the estimation of spherical harmonic gravity field coefficients from the disturbing potential values computed in the previous section by a least-squares adjustment. The adjustment process was discussed in section 2.4 and expressed as (cf. equ. 2.69):

$$\hat{\mathbf{x}} = \left(\mathbf{A}^{\mathrm{T}}\mathbf{P}\mathbf{A} + \alpha^2\mathbf{R}\right)^{-1}\mathbf{A}^{\mathrm{T}}\mathbf{P}\mathbf{l}\,, \tag{3.7}$$

where the time series of disturbing potential values T enters as vector of (pseudo-) observations $\mathbf{l}$, and the vector of unknowns $\hat{\mathbf{x}}$ contains the potential coefficients which are to be estimated.

System of Normal-Equations: The assembly and solution of the normal equations results in large requirements on computation time and memory due to the large number of observations, o, and unknowns, u, but is manageable on a standard PC by employing highly optimized algebraic routines. The computation is done on a standard PC with a 3 GHz CPU and 1 GByte of main memory in reasonable time. The design-matrix $\mathbf{A}$ has $o \cdot u$, with $o \approx 1.2$ million and $u = (L_{\max} + 1)^2$, elements which occupy

8 bytes of memory each. For a maximum degree of $L_{\max} = 100$ the matrix would require more than 90 GByte which by far exceeds the available main memory. This means, that the design matrix cannot be kept completely in memory and has to be divided into blocks as described in section 2.4.2. The normal equation matrix $\mathbf{N}$ has $(L_{\max}+1)^4$ elements. As it is advantageous to completely keep it in the memory, the maximum degree is limited to about $L_{\max} = 100$, which is fairly sufficient for a CHAMP-only gravity field analysis as will be shown.

The largest requirement in terms of computation time is the assembly of the matrix of normal equations $\mathbf{N} = \mathbf{A}^{\mathrm{T}}\mathbf{P}\mathbf{A}$. The multiplication of a matrix with its transposed can very efficiently be carried out by the BLAS (binary linear algebraic subroutines (Lawson et al. (1979))) routine `dsyrk`. In order to make use of the routine, the weight matrix $\mathbf{P}$ has to be Cholesky factorized with the BLAS routine `dpotrf`: $\mathbf{P} = \mathbf{U}^{\mathrm{T}}\mathbf{U}$, and the system of normal equations can be transformed:

$$\hat{\mathbf{x}} = \left(\mathbf{A}^{\mathrm{T}}\mathbf{U}^{\mathrm{T}}\mathbf{U}\mathbf{A} + \alpha^2\mathbf{R}\right)^{-1}\mathbf{A}^{\mathrm{T}}\mathbf{U}^{\mathrm{T}}\mathbf{U}\mathbf{l} = \left(\tilde{\mathbf{A}}^{\mathrm{T}}\tilde{\mathbf{A}} + \alpha^2\mathbf{R}\right)^{-1}\tilde{\mathbf{A}}^{\mathrm{T}}\tilde{\mathbf{l}}\,. \tag{3.8}$$

In case additional accelerometer parameters are estimated (cf. sec. 3.1), 2 additional parameters have to be estimated per arc. It has been found out empirically, that short arcs of at most one hour (or resp. 120 samples) should be used. Hence more than 46000 additional parameters for the more than 23000 arcs are added to the unknown parameters. The normal equation matrix $\mathbf{N}$ would become too large to be completely kept in memory. Therefore the additional parameters have to be eliminated from the system as described in section 2.4.2. As the design matrix $\mathbf{A}$ has to be divided into blocks anyway, it is very convenient to set up one block for each of the short arcs, with exactly 2 parameters to be eliminated.

Weight-Matrix P (Stochastic Model): As described in section 2.2.3 the variance/covariance information has to be propagated from the orbit positions to the disturbing potential values using equation 2.38. The orbit used for this work only contains the 3×3 variance/covariance matrices $\mathbf{\Sigma}_{33}$, which describe the variance/covariance between the 3 components of each position. As a test the full variance/covariance information $\mathbf{Q}_{\mathrm{block}}$ is included exemplarily for one week in half-daily blocks with one hour of overlap. The variance/covariance matrix for the first half of day 198/2002 is shown in figure 3.16. It can be seen, that two parts of this data set are completely independent, as there are two quadratic sub-matrices on the diagonal and the rectangular off-diagonal blocks only contain zeros. The larger of the two again is separated in two blocks with a low correlation between them. Those new blocks always occur when a new arc is set up in the POD or some discontinuity happens like a signal break or a change in the GPS constellation. A look at the correlation matrix in figure 3.17 (here only for the x-axis) shows an even more block-like structure. There are blocks of considerable correlation (> 0.5) over half an hour with almost no correlation to adjacent blocks. This is about the average time, that the satellite observes the same constellation of GPS satellites. These correlations should be considered and would give a very good tool to select short arcs reasonably well if the information was available for the whole data set. But as the variance/covariance information of the orbits has not been available for the whole time span, the full error propagation could not be performed. The use of the $\mathbf{\Sigma}_{33}$ information did deteriorate the solution, which has to be further investigated. Hence the error propagation was neglected and a unit matrix was assumed as weight matrix: $\mathbf{P} = \mathbf{I}$.

Solution: As a first test to find out the optimal maximum degree $L_{\max}$, several solutions were computed for $L_{\max} = 20$, 40, 60, 80 and 100. The requirements of computer resources are displayed in table 3.6. The results are compared to the EIGEN-GL04C model (cf. Förste et al. (2006)) as reference and the degree RMS differences between the solutions and the reference model are shown in figure 3.18. This test is of course not an absolute quality measure. But as the EIGEN-GL04C model – which is a combination of GRACE and surface data – is supposed to be more accurate than any CHAMP-only solution over all wavelengths, it can be considered as an independent tool for a quick quality check (in contrast to a full external validation given in section 3.4).

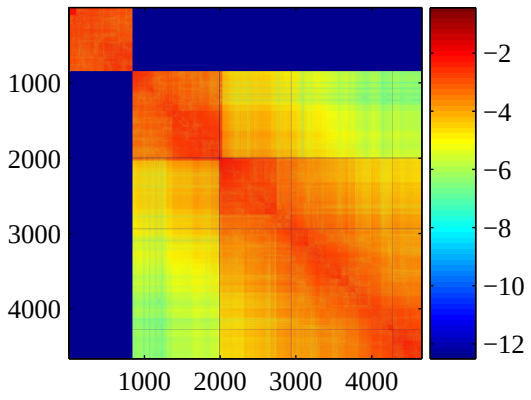

Figure 3.16: Full variance/covariance matrix for 12h Orbit [m^2] (with logarithmic colorbar).

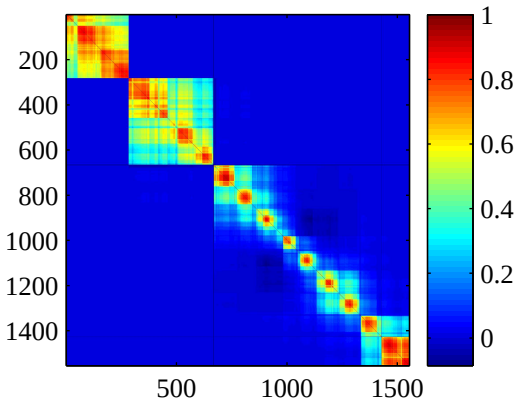

Figure 3.17: Correlation matrix for the x-Component of 12h Orbit.

Table 3.6: Requirements to computation time and memory.

$L_{\max}$	20	40	60	80	100
computation time t [s]	389	1918	6928	19356	34855
memory usage of $\mathbf{N}$ [MByte]	1.4	22	105	328	794

From this plot several conclusions can be drawn. First of all it is apparent, that the degree RMS difference intersects Kaula's rule of thumb, which gives a degree RMS value for the coefficients of the same degree, at about degree 70. The difference between the solution and the reference model becomes larger than the standard deviation at this point. As the reference model is supposed to be much more accurate, one can draw the conclusion, that the signal to noise ratio of the solution becomes larger than one, and the estimated coefficients do – on average – not hold meaningful gravity field information above degree 70.

It is also apparent, that solutions with lower maximum degree show larger differences to the reference model than solutions with higher maximum degree. The highest two degrees of each solution show especially large differences. This indicates, that the signal which is omitted by truncating the series expansion leaks into the lower coefficients and deteriorates the solution.

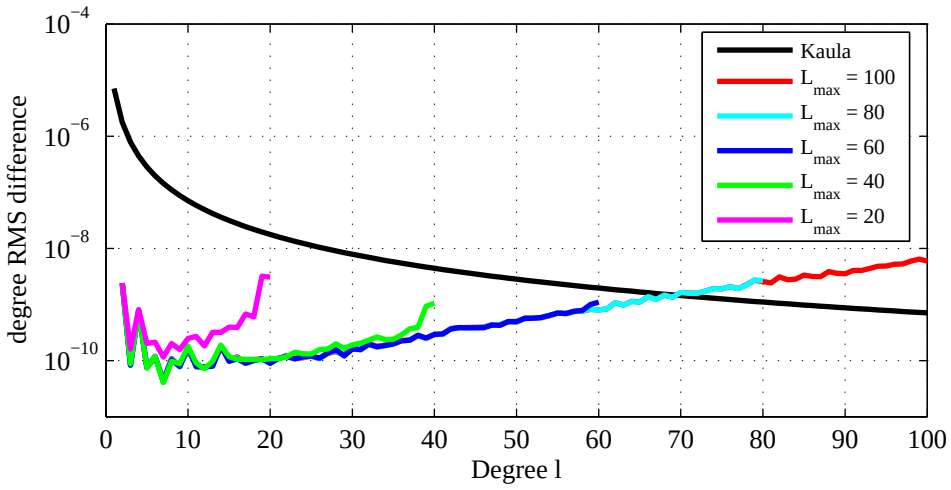

Figure 3.18: Degree RMS difference to reference model for different solutions.

From these two observations the somehow contradictory conditions arise, that on the one hand the solution should be limited to degree 70 and on the other hand the maximum degree $L_{\max}$ should be as high as possible to minimize the effect of leakage. As a compromise, it was chosen as strategy for all following computations, that the adjustment is solved for coefficients up to degree $L_{\max} = 80$ but only coefficients up to degree 70 are used for comparisons, validation and geoid computation. It is in theory possible to truncate a gravity field solution at any degree, as the base functions of the spherical harmonic series expansion are orthogonal in case of a regular data distribution. In order to prove that this is also a valid strategy in this particular case a look on the system of normal equations is necessary, which reflects the geometry of the data distribution. Figure 3.19 shows the inverse of the normal matrix $\mathbf{\Sigma}_{\hat{x}\hat{x}} = \mathbf{N}^{-1}$ of the solution with $L_{\max} = 80$.

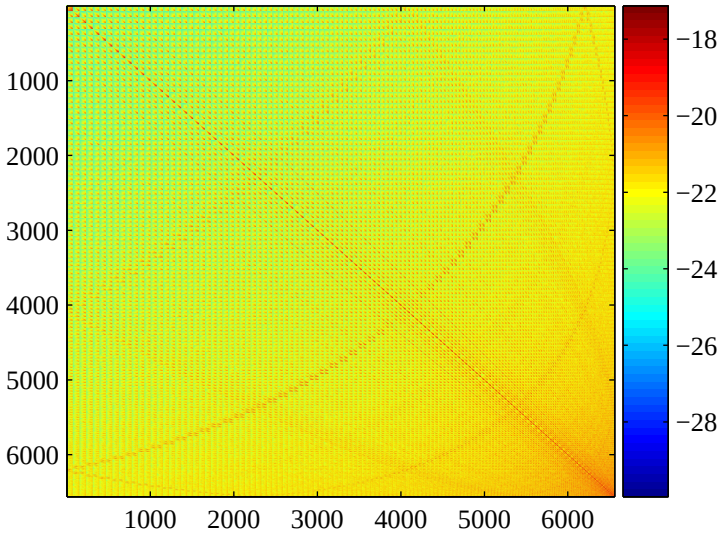

Figure 3.19: Variance/Covariance matrix of the gravity field solution.

The inverse normal matrix shows, apart from a dominant diagonal, only correlations in the mid degrees, which reflect orbit resonances at around degree and order 32. After normalizing the matrix according to equation 2.60 it becomes apparent, that those correlations do not play an important role. Figure 3.20 shows three zoomed parts of the correlation matrix $\mathbf{C}$: the coefficients of low orders m= 0 and 1, the middle part of the matrix with orders from m= 30 to 33 and the high orders between $m = 60$ and 80. Apart from a few exceptions the correlations off the diagonal stay below $\mp$ 0.1, which shows that the coefficients can be determined almost independently. As there are no especially strong correlations at around degree 70, the solution can be truncated without problems. The exceptions are, that the zonal coefficients of order m=0 are correlated, any coefficient is anti-correlated to its direct neighbor (≈ -0.3) and coefficients of the highest two degrees of the same order are also weakly correlated (≈ 0.2). The latter explains the weak determination of the highest two degrees, as apparently they are not well determined. But this problem is avoided by truncating the solution.

Comparison of the Results: As mentioned in section 3.1, the remaining systematic effects in the disturbing potential have been treated with two alternative approaches: one tries to calibrate long wavelength errors by the use of an a priori model, the other estimates bias and drift parameters over short arcs. Figure 3.21 shows, that the approach to estimate additional parameters performs worse than the long wavelength approach, if compared to the EIGEN-GL04C model. The differences are largest between spherical harmonic degree $l = 5$ and $l = 40$. Both solutions show large errors in the very low degrees with $l < 5$. Especially the $\bar{C}_{20}$ and $\bar{C}_{40}$ show very large errors which neither of the two approaches can compensate. These errors cannot be explained and should be further investigated. As

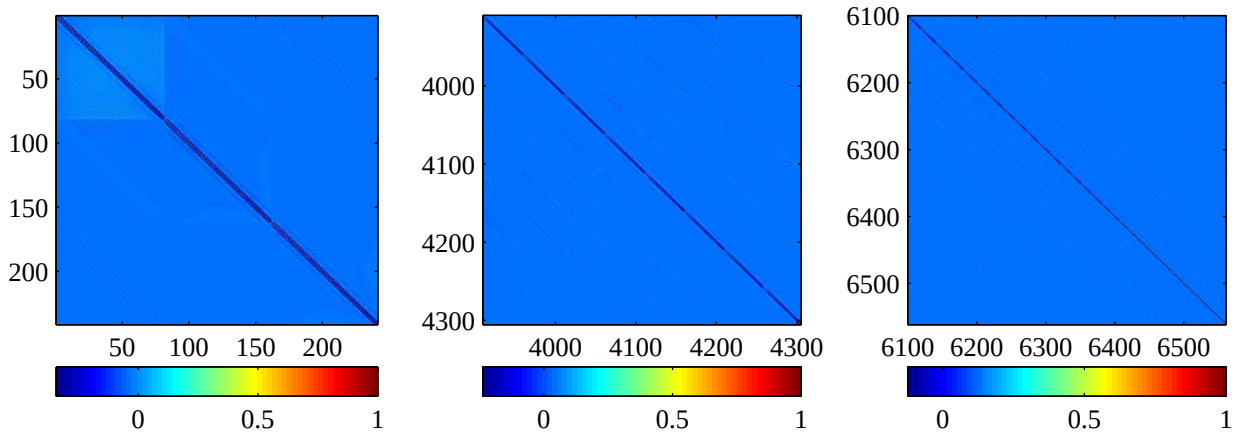

Figure 3.20: Details of the correlation matrix $\mathbf{C}$. *Blocks corresponding to orders* $m = [0; 1]$ *(left),* $m = [30, ..., 33]$ *(center) and* $m = [60, ..., 80]$ *(right).*

the general performance of the model using the long wavelength error compensation is better, it will be used in all further comparisons.

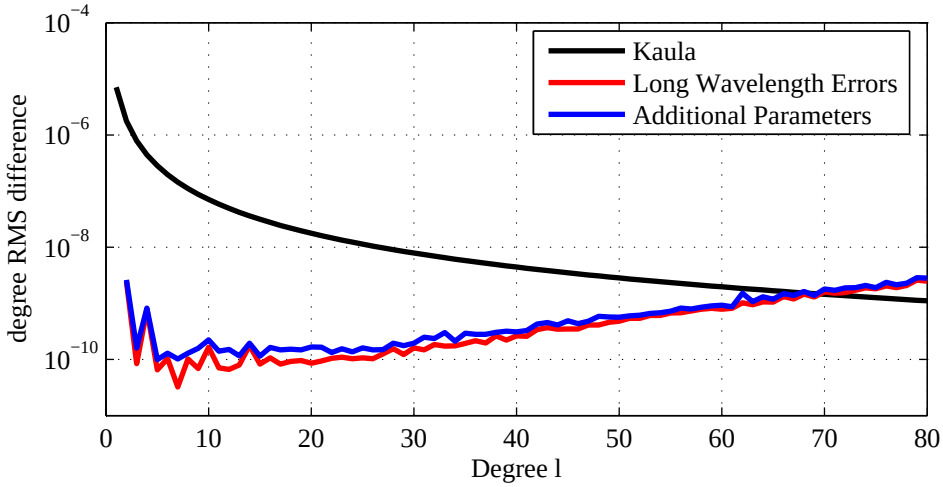

Figure 3.21: Degree RMS difference to reference model using different calibration methods.

It was derived in section 3.1, that non-smoothing methods for velocity derivation should theoretically perform better for the CHAMP data set. In order to validate this, five different solutions were computed, and the comparison to the reference model shows substantial differences (see fig. 3.22). The non-smoothing methods (blue and red curve) produce better results than the smoothing ones – although the residuals after adjustment are smaller for smoothing methods. This seems like a contradiction but can be explained: the smoothing methods produce a potential series along the orbit for which the adjustment finds a better fitting solution but is obviously further from reality, as gravity field signal has been smoothed out. This empirical test perfectly confirms the theoretical reflections in section 3.1.

Formal Error Analysis and Error Propagation: In order to perform a formal error analysis, the a posteriori variance factor σ_0^2 has to be computed from the residuals using equation 2.57 and the inverse normal equation matrix has to be scaled with σ_0^2 to obtain the variance/covariance matrix. The residuals are shown in figure 3.23. The resulting a posteriori variance factor is $\sigma_0^2 = 1.205\,\mathrm{m}^4/\mathrm{s}^4$. Respectively the standard deviation of the disturbing potential values at satellite altitude is $\sigma_0 = 1.098\,\mathrm{m}^2/\mathrm{s}^2$. This

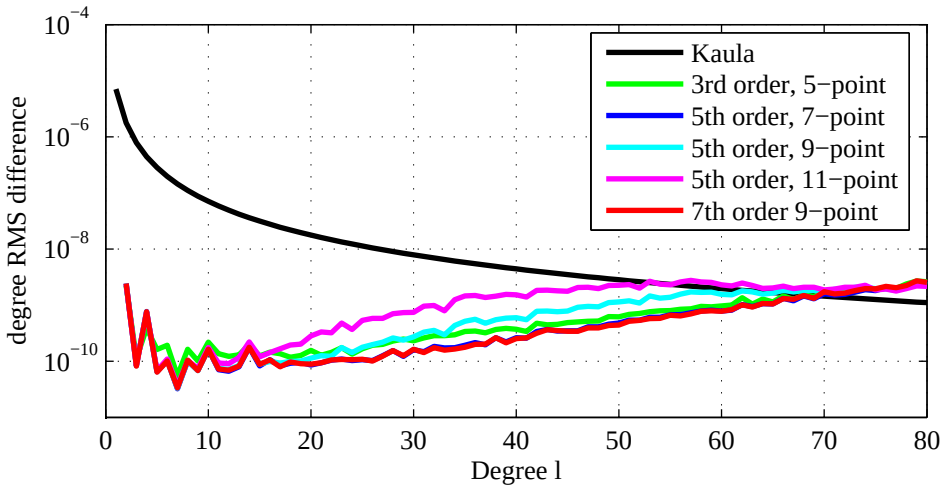

Figure 3.22: Degree RMS difference to reference model using different velocity derivation methods.

can be converted to an estimate of the velocity error by error propagation. Using $\sigma_{\dot{\mathbf{r}}} = \sigma_T / \dot{\mathbf{r}}_0$ one obtains a velocity error of $\sigma_{\dot{\mathbf{r}}} = 1.4\,\mathrm{mm/s}$.

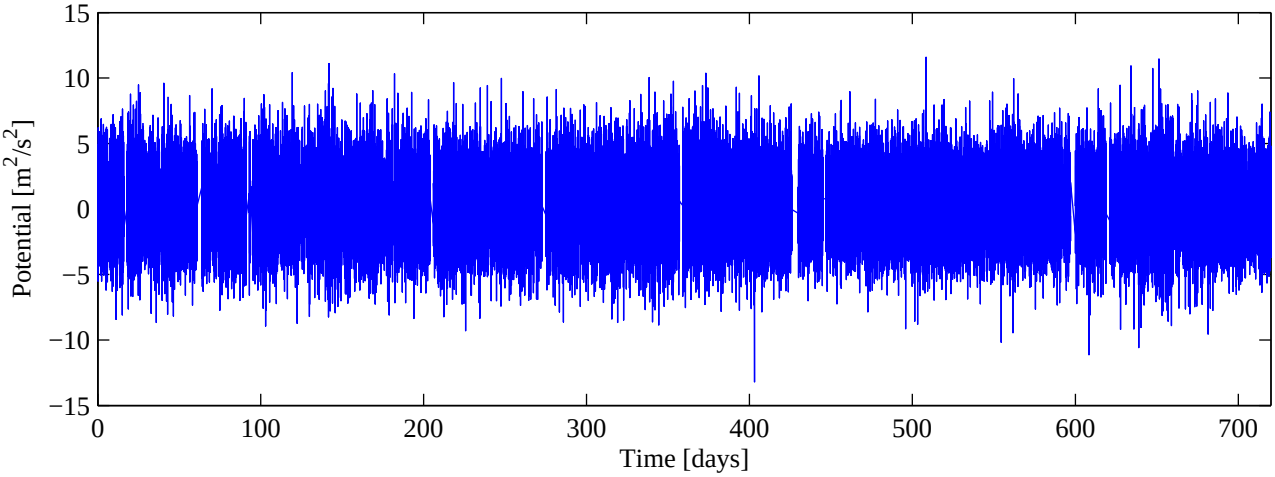

Figure 3.23: Residuals after adjustment.

The diagonal of the variance/covariance matrix holds the formal variances of the coefficients. The corresponding standard deviations of the coefficients are shown in figure 3.24. The error is rising towards coefficients of higher degree and order. The error distribution is very regular. The standard deviation per degree is shown in figure 3.25 and compared to Kaulas rule of thumb. It can be seen, that the formal error is slightly more optimistic than the comparison to the reference model shows – especially for the low degrees. Nevertheless, also the formal error curve intersects the Kaula curve at about degree 70. It is common to calibrate the errors by comparison of sub-set solutions (cf. e.g. Reigber et al. (2005)). This means, that several solutions are computed from different partial data sets, and the variation of the resulting coefficients is used to derive a scale factor for the errors per spherical harmonic degree. It should be noted that this is not an absolute method to determine the coefficient error but more an empirical guess. The green curve in figure 3.24 shows that the calibrated errors match the difference to the reference quite well – except for degrees 2 and 4, which has to be further investigated.

The formal errors can be displayed to cumulative geoid errors as shown in figure 3.26. Here again the difference to the reference model is slightly larger than the formal errors, which can mainly be attributed to the $\bar{C}_{20}$ and $\bar{C}_{40}$ coefficients. The cumulative geoid height error is 27 cm at degree 70.

The comparison with the EGM96 model (which is considered the best pre-CHAMP model) shows an improvement of up to degree $l = 60$. Above that the terrestrial gravity information which is included in EGM96 dominates.

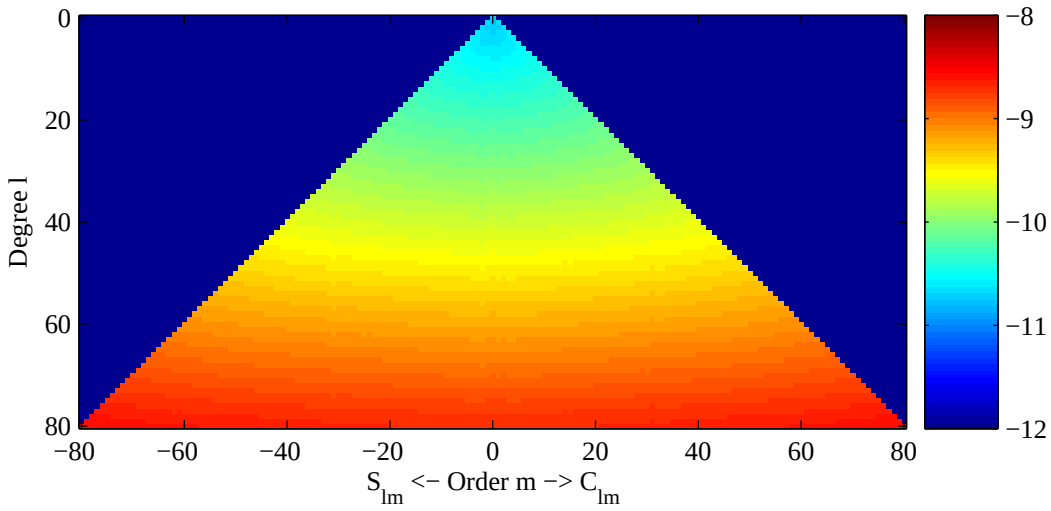

Figure 3.24: Formal coefficient errors.

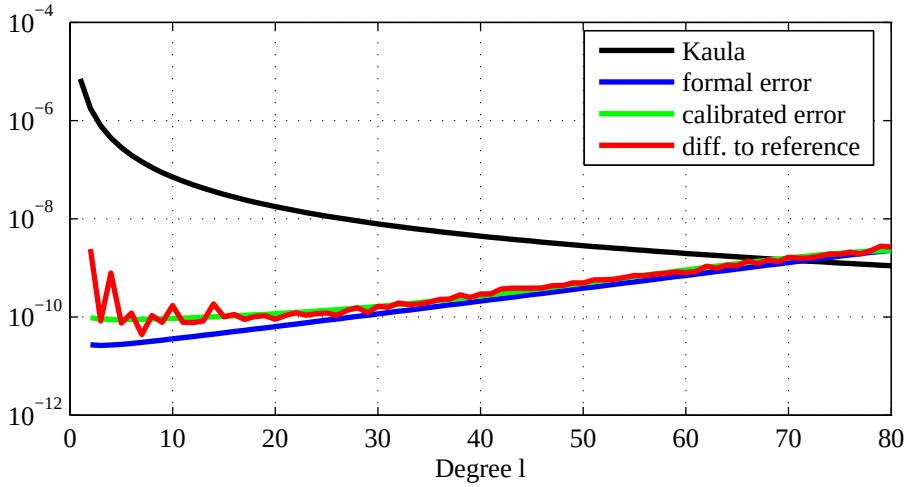

Figure 3.25: Formal coefficient errors per degree.

Finally the variance/covariance matrix up to degree 70 is used to compute a full error propagation to determine formal geoid height errors on a global grid, which is displayed in figure 3.27. Apparently the quality of the solution is better at higher latitudes ($\sim 10\,\text{cm}$) than at the equator ($\sim 33\,\text{cm}$) (except for a very small polar gap), as the data density is much higher near the poles due to the inclination of the satellite orbit of almost 90. The error plot shows a strong pattern of stripes in North-South alignment, which reflect the satellite tracks.

Variance Component Estimation: For the short arc approach a variance component estimation can be performed in order to improve the results of the global solution. Each of the 23000 short arcs can be regarded as a partial data set. A variance factor σ_i is computed for each arc to give it its individual weight according to the quality of the partial data. These variance factors are used in an iterative procedure and improved during each iteration until convergence is achieved.

The strict computation of the variance factors would be a very demanding task, as it involves the

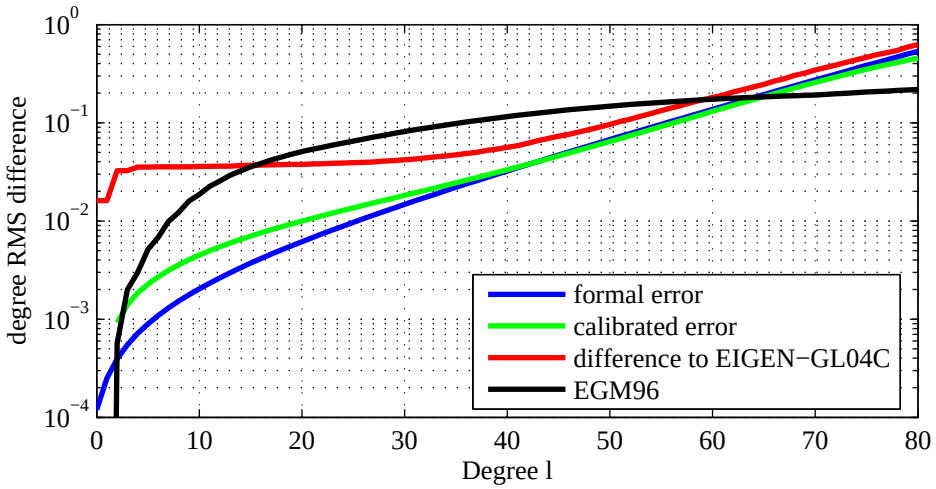

Figure 3.26: Cumulative geoid height errors [m].

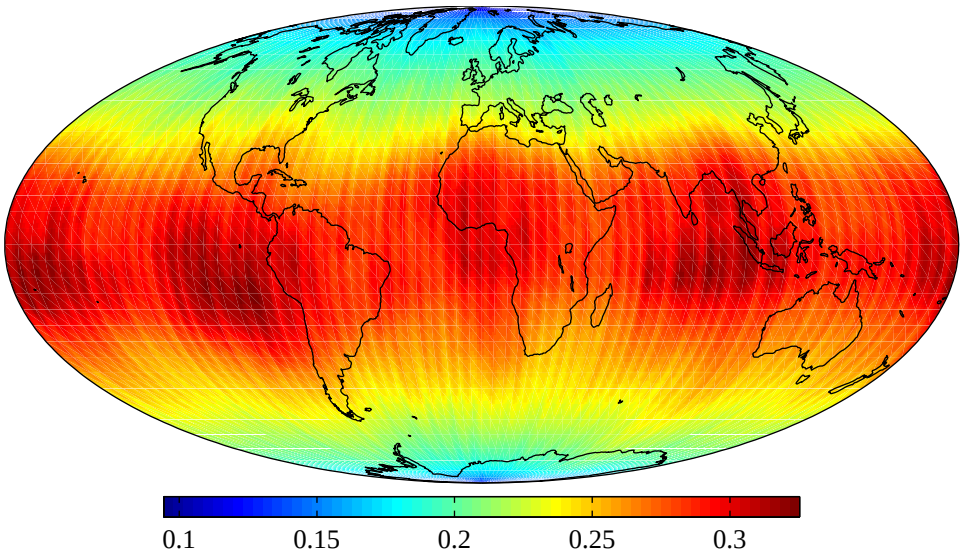

Figure 3.27: Propagated geoid height errors [m].

computation of the trace of the product of two matrices with $(L_{\max}+1)^4$ elements for each of the 23000 arcs. This can be simplified by the assumption, that all the arcs solve for an equal share of the unknown coefficients. Equation 2.76 is simplified to:

$$\hat{\sigma}_i^2 = \frac{\hat{\mathbf{v}}_i^{\mathrm{T}} \mathbf{P}_i \hat{\mathbf{v}}_i}{n_i - u/a} \,. \tag{3.9}$$

where a is the number of arcs.

The variance factors which were found after the 2nd iteration are shown in figure 3.28. It can be seen, that only few outliers were found, which exceed $3\sigma \approx 3.3\,\mathrm{m}^2/\mathrm{s}^2$. However the overall quality of the first 750 arcs seems to be slightly worse than the rest of the data, which might be explained by an improvement in the processing of GPS data. The overall quality of the solution could only be marginally improved from a global geoid height difference to the reference model of X to Y. This shows,

that the strict data preprocessing did not leave many arcs of particularly bad quality which had to be down-weighted.

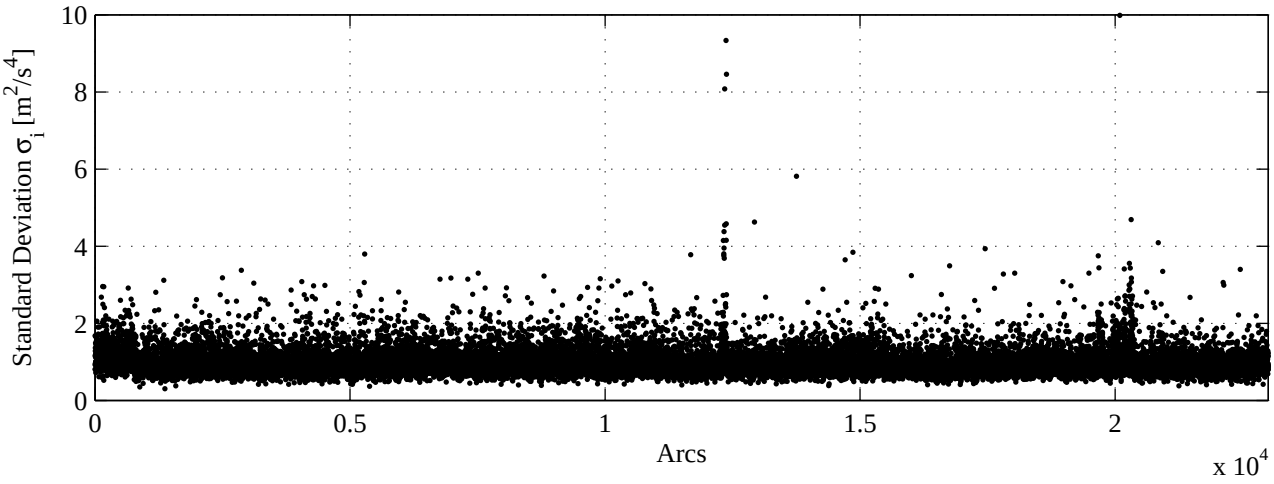

Figure 3.28: Formal coefficient errors.

Regularization: Another attempt to improve the solution and to extend the range of meaningful potential coefficients beyond degree 70 is to regularize the system of normal equations with a priori information. As the standard deviation of the coefficients above degree 70 becomes larger than their expected standard deviation determined by Kaula's rule of thumb, it suggests itself to constrain the coefficients. This is done by adding an additional observation equation for each coefficient with an expected value of 0 and the standard deviation taken from Kaula's rule of thumb. This leads to the so-called Kaula regularization (cf. sec. 2.4.2). As a result, the diagonal regularization matrix $\mathbf{R}$ is added to the normal equation matrix weighted by the factor $\sigma_0^2 = 1.205\mathrm{m}^4/\mathrm{s}^4$. The result is displayed again as degree RMS difference between the solution and the reference model in figure 3.29. It can be seen, that the degree RMS difference now follows Kaula's rule of thumb closer above degree 70. But this actually shows, that nothing was gained, as the coefficients now just obtain random values within the range of freedom that was defined by the a priori standard deviation.

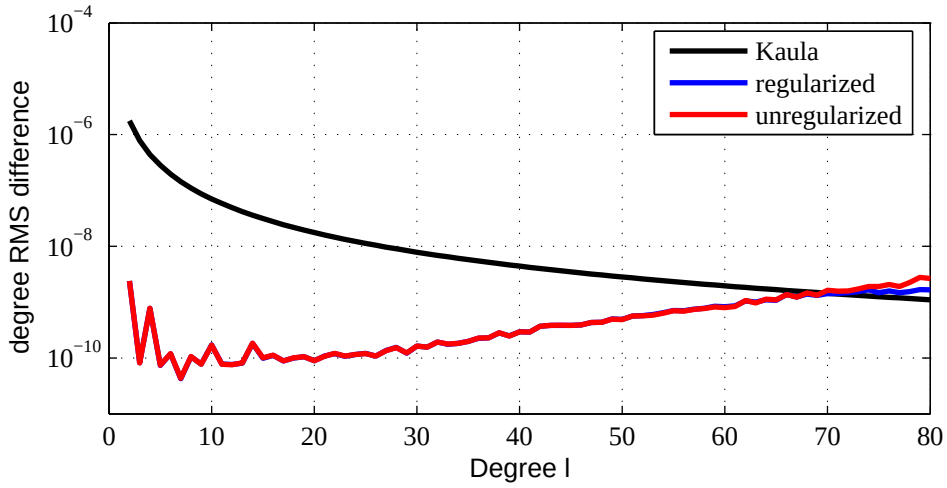

Figure 3.29: Regularized solution.

A contribution analysis of the regularization matrix (cf. 3.30) shows, that the influence of the a priori information dominates above degree 70, and is almost negligible below degree 60. Thus it is decided, that no regularization is employed.

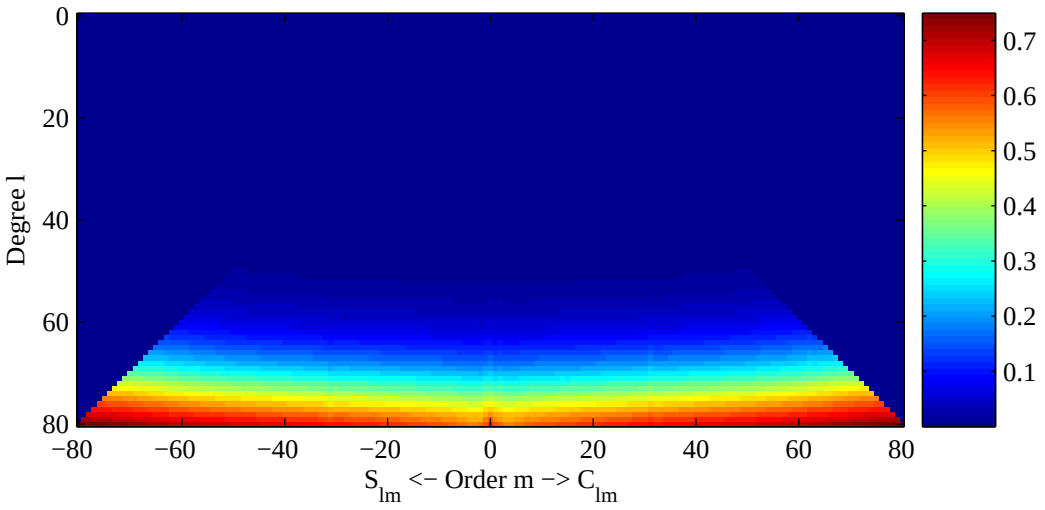

Figure 3.30: Contribution of the regularization matrix to the solution.

3.3 Semi-Analytical Solution

Although the direct gravity field analysis worked well and in a reasonable time for the whole 2 years of data, the semi-analytic approach is applied to the same data to show its potential and limitations in perspective of the GOCE and future missions. The preprocessing sequence to derive disturbing potential values T along the orbit is exactly the same as for the direct solution. As the semi-analytical approach does not provide the possibility to solve for additional parameters like accelerometer biases, they have to be removed from the observations beforehand according to (cf. sec. 3.1). Both the 1D-FFT and 2D-FFT approaches are applied to the data.

3.3.1 1D-FFT Approach

It was shown in section 2.5 that the one-dimensional spectrum of a time series along the orbit can be mapped to spherical harmonic functions if several conditions are – at least approximately – fulfilled. The orbit should be circular – which implies a constant orbit radius r and inclination I – and the orbit should close after β revolutions in α nodal days to meet the periodicity condition for a Fourier transform. It was also stated, that deviations from these requirements can be overcome to a certain extent by iteration.

A look at the orbit height in figure 3.1 shows that the requirement of a constant semi-major axis is obviously not met as the satellite is constantly sinking. In addition the two orbit maneuvers cause large discontinuities, which may result in difficulties in a spectral analysis.

As an effect of the varying orbit height and small variations in the inclinations I, the ratio between β and α (cf. equ. 2.81) is varying too. Figure 3.31 shows the (smoothed) fluctuations in the ratio β/α, where high frequency signals with sub-revolution period have been removed for clarity.

Despite the fact that many repeat patterns could be found – meaning that the ground-track of an orbit passes very close to where it had passed an integer number β of revolutions before – it was not possible to find one where the number of nodal days α is integer as well and the number of revolutions $\beta > 140$, which is necessary for a solution up to degree 70.

As an example the average ratio β/α is at about 15.734729 in the period before the first orbit maneuver. This would come close enough to a repeat cycle of $\beta = 771$ revolutions in $\alpha = 49$ nodal days. But the real orbit is too far away from the theoretical circular orbit, so that the spectral mapping fails. In this case an iterative solution cannot overcome the deviations and does not converge.

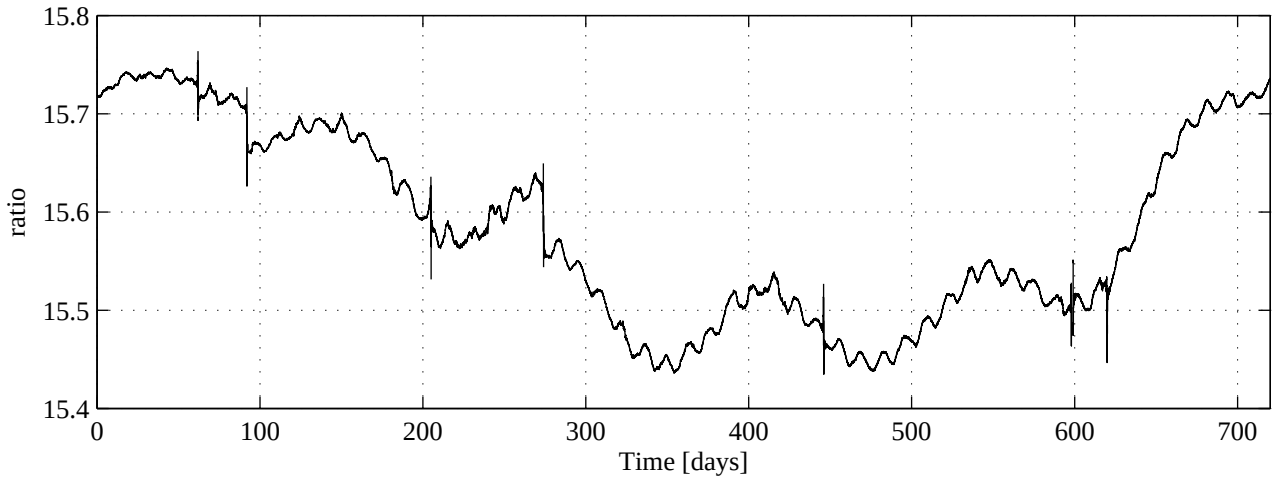

Figure 3.31: Revolutions per day β/α.

After the second orbit maneuver the satellite passes several times the resonance band, where $\beta/\alpha = 15.5$ and the orbit repeats after 2 days and 31 revolutions. While that might be interesting for resonance analysis, 31 revolutions are clearly not enough for a gravity field solution up to degree and order 70.

In conclusion one can say, that the 1D-FFT approach is not suited for a missions like CHAMP, which has no orbit control that maintains a constant orbit height. It may very well be suited for mission like GOCE, where the drag-free control maintains a constant orbit height and certain repeat-cycles are planned.

3.3.2 2D-FFT Approach

In contrast to the 1D-FFT approach, the 2D-FFT approach is not dependent on a constant repeat-ratio as the observations are interpolated to the (u, Λ)-torus. However the problem of a non-constant orbit radius r and inclination I remains, as the torus is based on the assumption of these two parameters being constant and an error is introduced by using the observations at a wrong height. The real height differs from the mean up to $\pm 30\,\mathrm{km}$. An additional error is introduced by the interpolation itself, as the disturbing potential values T which are irregularly distributed and afflicted by an error have to be interpolated to a regular grid. Hence the interpolation method has to be regarded thoroughly.

Interpolation on the Torus: A basic and commonly applied method for the interpolation of irregular 2D data is to define a certain area around each interpolation point and to compute a weighted average of all values within the area, where the weight is an isotropic function of the distance d_i between interpolation point P and data point P_i. The interpolated value of the disturbing potential T at point P becomes:

$$T_P = \frac{\sum_i T_i f(d_i)}{\sum_i f(d_i)} \ , \tag{3.10}$$

with T_i being the disturbing potential at point P_i. The distance between point P and P_i is defined by $d_i^2 = \sqrt{(u_i - u_P)^2 + (\Lambda_i - \Lambda_P)^2}$, which is a simplification as the metric of the (u, Λ)-system is non-Euclidian. But as only data points in the vicinity of the interpolation point are considered, this can be neglected.

For example weighting functions like inverse distance $f(d) = 1/d$, inverse squared distance $f(d) = 1/d^2$ or the Gauss-function $f(d) = e^{-\sigma d^2}$ can be used. The steepness of the weighting function and the

maximum distance define the characteristics of the interpolation. A Gauss-function with a small σ is smoothing as also farther points get a high weight, while the inverse quadratic distance is quite rough. Nevertheless the choice of the weighting function is quite arbitrary and the quality of the interpolation or respectively the interpolation error can only be judged empirically. Out of the tested functions, the inverse square distance performed best leaving residuals with an RMS of $1.34\,\mathrm{m}^2/\mathrm{s}^2$ over all grid points, which is quite good but worse than the residual RMS of $1.01\,\mathrm{m}^2/\mathrm{s}^2$ over all data points of the direct solution (cf. sec. 3.2).

A less arbitrary approach is to estimate the values on the interpolation points. Figure 3.32 shows the vicinity of a selected interpolation point ($u = 21°, \Lambda = 216°$). It can be imagined, that the measurement values form a two-dimensional surface. Hence the surface can be approximated by a 2D-polynomial of second order:

$$f(x, y) = a_5x^2 + a_4xy + a_3y^2 + a_2x + a_1y + a_0 \ , \tag{3.11}$$

where $x = \Lambda - \Lambda_P$ and $y = u - u_P$. The polynomial coefficients can now be estimated by a least-squares adjustment using all data points within a certain distance from the interpolation point:

$$\mathbf{a} = \left(\mathbf{A}^{\mathrm{T}}\mathbf{A}\right)^{-1}\mathbf{A}^{\mathrm{T}}\mathbf{l} \ , \tag{3.12}$$

where $\mathbf{a}$ is the vector of polynomial coefficients, $\mathbf{l}$ the vector of observed values and $\mathbf{A}$ the design matrix with partial derivatives. It was found out, that with this data set using a higher order polynomial than second order does not improve the solution as well as taking points which are farther than $d = 2°$ into the computation. As for the interpolation point P $x = 0$ and $y = 0$ only the coefficient a_0 needs to be determined, as $f(0, 0) = a_0$. Hence equation 3.12 can be reduced to the dot-product of the first line of $\left(\mathbf{A}^{\mathrm{T}}\mathbf{A}\right)^{-1}\mathbf{A}^{\mathrm{T}}$ with the vector of observations $\mathbf{l}$. The elements of the first line of $\left(\mathbf{A}^{\mathrm{T}}\mathbf{A}\right)^{-1}\mathbf{A}^{\mathrm{T}}$ sum up to exactly one. This can be interpreted as weighting as well, as the interpolated value is the weighted average of the observations. The weights which are shown in figure 3.33 show a dependence on the radial distance d_i to the interpolation point but is not completely isotropic. This interpolation method accommodates better to the point distribution than those mentioned above. As a result this interpolation method reduces residuals to $1.03\,\mathrm{m}^2/\mathrm{s}^2$ and thus performs much better than the other methods. As a drawback it takes much longer to compute as a least squares adjustment has to be solved for each point. It can be accelerated to a level which is acceptable for a *quick-look* solution by doing all the indexing of which data point is used for which interpolation point before the actual computation of the first iteration, which as a drawback uses much memory.

Solution: The solution of the block-diagonal system is very fast compared to the direct solution. The overall computation time is 4 min per iteration at $L_{\max} = 80$. The iteration converges very quickly after only few iterations, which is shown in figure 3.34 in form of degree RMS differences to the EIGEN-GL04C reference model. It can be seen, that already after the second iteration no significant improvements can be achieved. The final semi-analytic solution (black curve) comes very close to that of the direct solution (green curve). Only below degree $l = 30$ the errors are slightly larger.

The interpolated values on the torus are displayed in figure 3.35. From the solution, the a posteriori potential values were computed on the torus grid by synthesis (equ. 2.16). The residuals which are the difference between a posteriori values and interpolated values are displayed in figure 3.36. As mentioned above, the overall RMS of the residuals on the torus is $1.03\,\mathrm{m}^2/\mathrm{s}^2$, which is very small – but they shows a systematic behavior, which reflects the orbit tracks on the satellite. This pattern can be attributed to the deviations in orbit height and is most likely responsible for the slightly decreased accuracy of the semi-analytical solution. The possibility of a height dependent correction of the potential values should be further investigated.

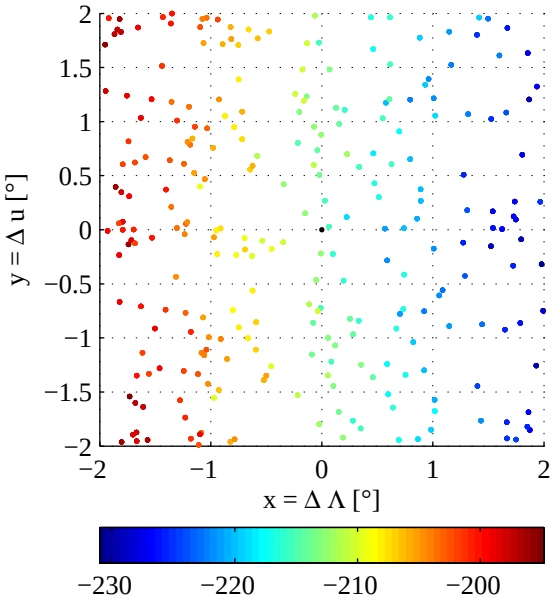

Figure 3.32: Observations T [m^2/s^2] in the vicinity of a grid point (black) at ($u = 21°, \Lambda = 216°$).

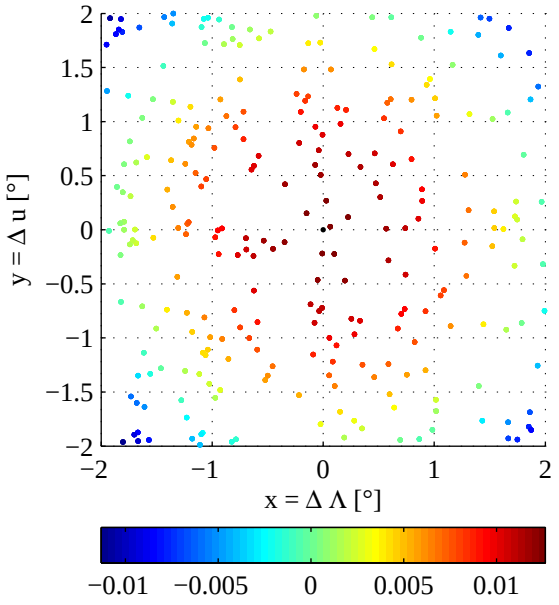

Figure 3.33: Weight-factors for data points (sum=1) contributing to the grid point (black) at ($u = 21°, \Lambda = 216°$).

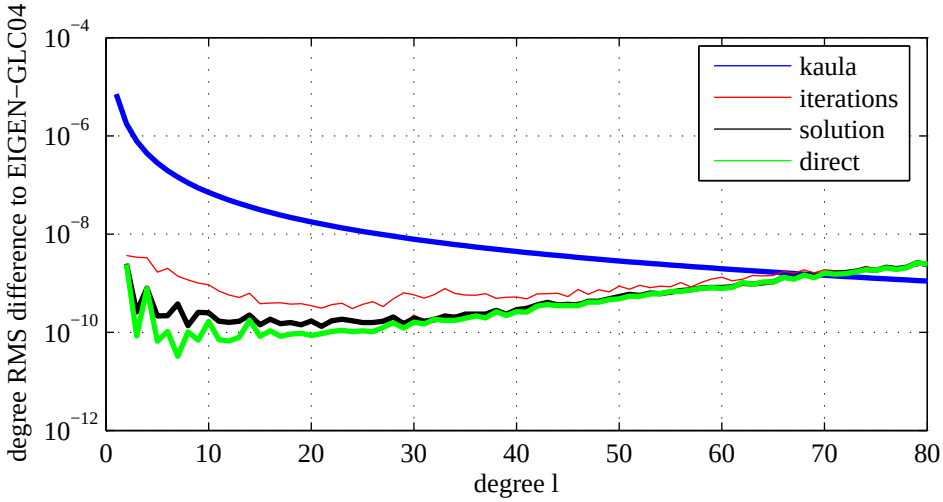

Figure 3.34: Comparison of the semi-analytic and direct solutions.

3.4 Validation

In order to asses the quality of the gravity field solution it has to be validated with external data and compared to other gravity field models. This is done by a test procedure described by Gruber (2004). The model derived in section 3.2 is referred to as TUM-2Sb. It is based on the same data as the TUM-2S model (Wermuth et al. (2005)) but includes some improvements in processing. The model derived in section 3.3 using the semi-analytical approach will be labeled TUM-2Ss.

The external data that is used for validation here are six national and regional GPS-leveling datasets. They contain geoid heights obtained by GPS-leveling on irregularly distributed points. Geoid heights computed from a global gravity model are compared to the GPS-leveling points. The RMS difference around their mean serves as quality measure. In order to be comparable, all tested global

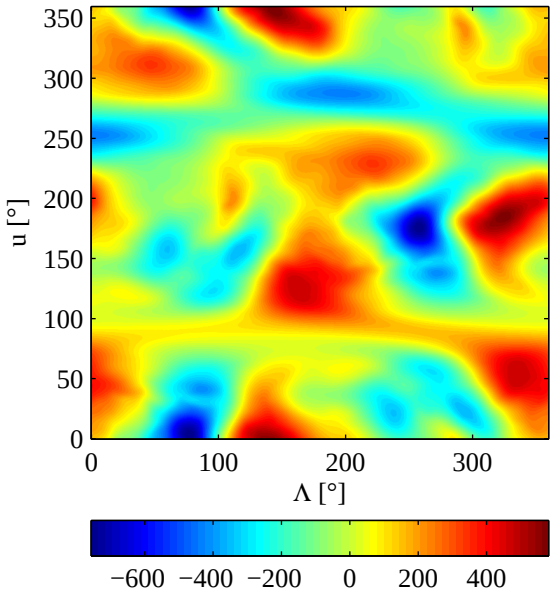

Figure 3.35: Interpolated disturbing potential values T $[m^2/s^2]$ on the torus grid.

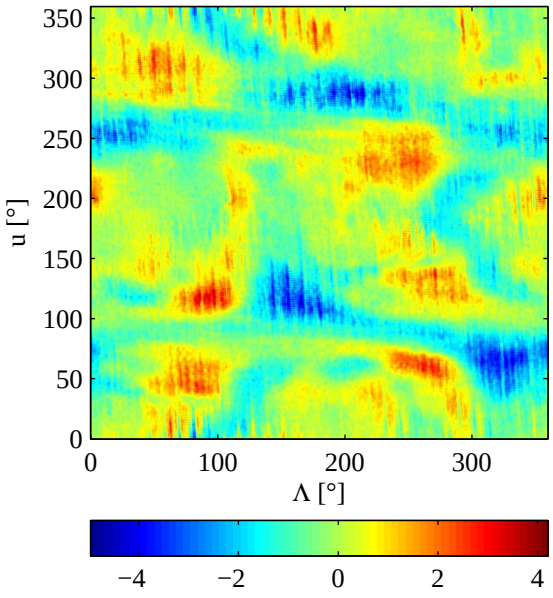

Figure 3.36: Residuals $[m^2/s^2]$ on the torus grid.

models are truncated at degree/order 60. As the GPS-leveling points contain the information of the full gravity field, the information above degree 60 has to be filtered out. This is done by computing the corresponding geoid heights from degree 61 to 720 using the high degree geopotential model GMP98A (cf. Wenzel (1999)) and removing them from the GPS-leveling data. Figure 3.37 shows the difference between geoid heights computed from the TUM-2Sb model and the GPS-leveling data set of the USA containing 5168 points. The difference for most of the points is within ±1 m - only few outliers have a difference of up to 1.5 m. The RMS difference around mean is 0.364 m.

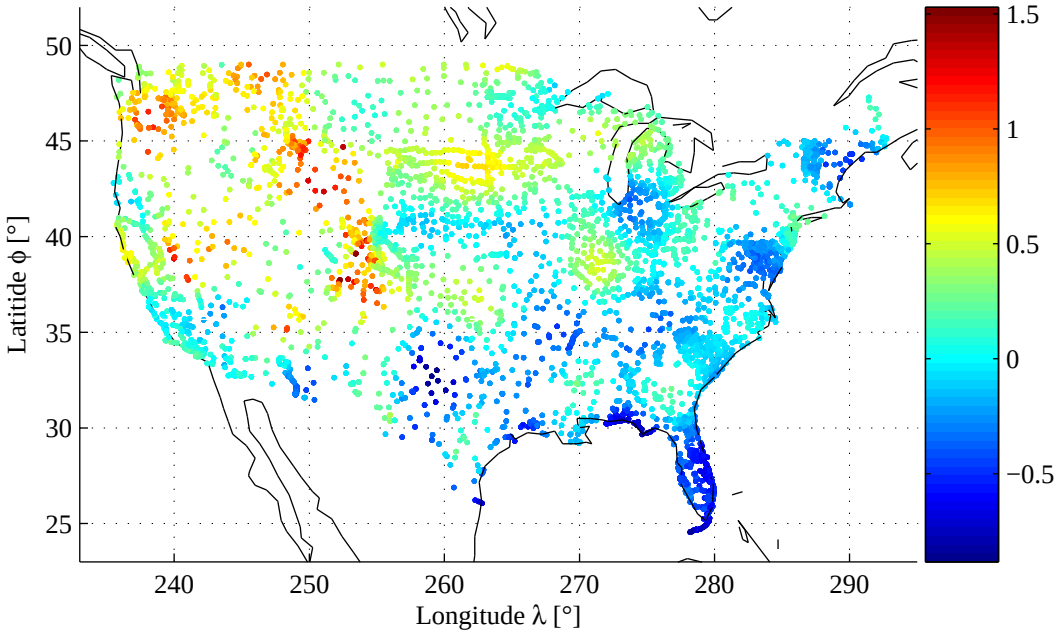

Figure 3.37: Geoid height differences [m] between the TUM-2Sb model and GPS-leveling points in the USA.

Next to the TUM-2Sb and TUM-2Ss models, which are derived from CHAMP-data only, five other global gravity models are included for comparison. Three of them are CHAMP-only models as well. The EGM96 model (Lemoine et al. (1998)) is considered the best pre-CHAMP model. The EIGEN-GL04C model (Förste et al. (2006)) is a combination of GRACE and terrestrial data and supposed to be more accurate than any CHAMP-only model. The CHAMP-only models are EIGEN-2S (Reigber et al. (2003)) computed from two years of CHAMP data using perturbation theory, EIGEN-3P (Reigber et al. (2005)) using 3 years of CHAMP data as well as an improved processing compared to EIGEN-2S and the ITG_CHAMP01S model (Mayer-Gürr et al. (2005)). It is based on the integral equation approach and uses one year of the same kinematic orbits (computed by Švehla and Rothacher (2004)) as the TUM-2Sb model. The results are shown in table 3.7.

The GPS-leveling data set used here are from six different regions (Australia, Canada, Europe, Germany, Japan and the USA) and have different characteristics. The USA data spreads over the largest area and contains the most points (5168). The Germany data set contains the most dense data distribution (675 points in a relatively small area) while the data distribution over Australia and Europe is very sparse (less than 200 points distributed over a relatively large area).

data set	points	TUM-2Sb	TUM-2Ss	EGM96	EIGEN-2S	EIGEN-3P	ITG-CH.01S	E.-GL04C
Australia	197	0.293	0.303	0.269	0.497	0.273	0.310	0.240
Canada	1443	0.253	0.254	0.303	0.312	0.235	0.241	0.197
Europe	180	0.266	0.260	0.386	0.579	0.251	0.259	0.230
Germany	675	0.073	0.076	0.345	0.484	0.120	0.135	0.035
Japan	837	0.136	0.141	0.251	0.550	0.128	0.178	0.116
USA	5168	0.364	0.364	0.370	0.521	0.348	0.375	0.332

Table 3.7: Geoid model validation using GPS-leveling. RMS Errors around mean [m].

As expected, the EIGEN-GL04C model fits best to all data sets. Out of the CHAMP-only models, which are – apart from EIGEN-2S – all on a similar level of accuracy, the EIGEN-3P fits best. The direct solution TUM-2Sb fits to most data sets slightly better than the semi-analytical solution TUM-2Ss. This confirms the results of the previous section. Only for the European data set, the TUM-2Ss solution fits slightly better. This is still within statistical boundaries of the statement, that the accuracy of the TUM-2Sb model is slightly higher, considering that the GPS-leveling data sets have errors, too. Table 3.7 shows, that the data sets which are spread over larger areas like USA or Europe fit less well to the satellite data than the data sets of relatively small areas like Germany or Japan. Hence the test results should be rather seen as a relative comparison than as an absolute error measure.

As a further test geoid height slopes are compared to analyze wavelength dependent errors. Geoid height slopes are computed – by taking the differences – between all possible points of a GPS-leveling data set. The same is done for the global models and the slopes are compared. The slopes are grouped in classes depending on their distance. For each class the standard deviation can be computed leading to a wavelength dependent error curve. The results are shown in figure 3.38 for the USA data set and in 3.39 for Germany. Here again the TUM-2Sb model is slightly better than TUM-2Ss. Both are roughly on the same level of accuracy than the other CHAMP-only models. They seem to fit less well to USA data in the very short wavelength below 500 km but better to the Germany data than the other CHAMP models.

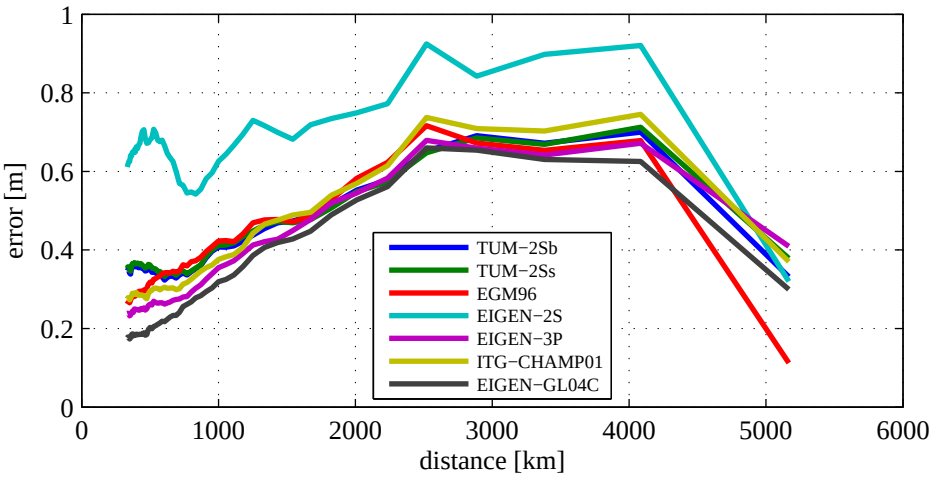

Figure 3.38: Geoid height differences [m] for USA GPS-leveling data set and geoid models.

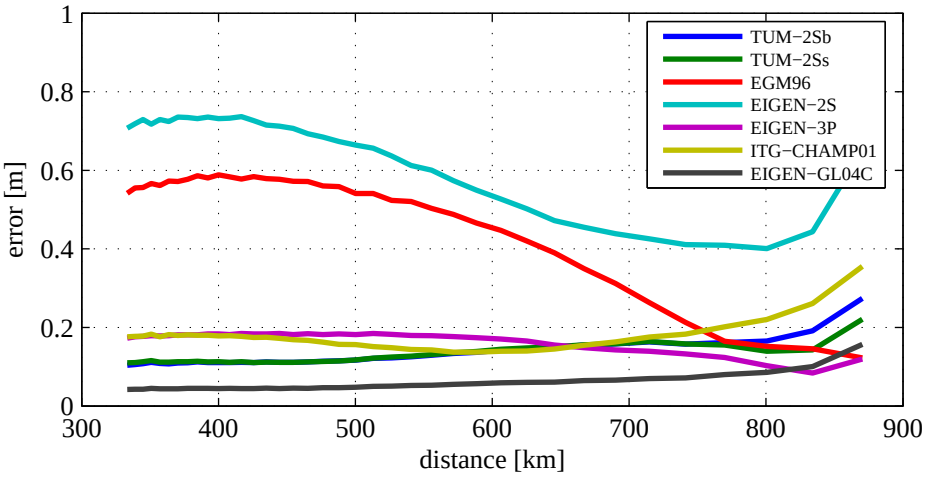

Figure 3.39: Geoid height differences [m] for Germany GPS-leveling dataset and geoid models.

4 GOCE QUICK-Look Gravity Field Analysis

A direct gravity field solution from GOCE-data is only possible with a computer cluster or a super-computer with many nodes. Due to the complexity of the complete processing procedure, the results will only be available several weeks after the end of the mission. As it is necessary to evaluate mission performance already in parallel to the mission, a quick-look processing chain has been implemented for the processing of GOCE data (e.g. Pail et al. (2006b)). The work presented in this chapter has contributed to the development of the operational software.

The purpose of the quick-look gravity field processing is to provide an analysis of the observations with a short latency of only a few days after they are acquired. Quick-look gravity fields will be computed on a regular basis from partial data sets. In addition an estimate of the spectral noise behavior will be provided in order to design filters for the final high-quality gravity field solution (see Pail et al. (2006a)).

The fast gravity field analysis will be achieved by using the semi-analytical approach (see sec. 2.5). As mentioned above, the semi-analytical approach is based on simplifying assumptions, which allow for a very efficient solution – at the cost of accuracy. In section 4.1, the performance of the semi-analytic approach will be analyzed using error-free simulations. This allows to separate the errors caused by the simplifications of the method from the influence of true measurement errors.

In section 4.2 the semi-analytic approach is applied to a simulated data set in the course of the mission preparations. Let us denote this data set SIM. This simulation uses a realistic mission scenario and includes a realistic instrument noise model.

4.1 Error-free Simulation

This simulation study consists of four test cases in order to evaluate the effect of three different error-sources. The first one will show a proof of concept with a perfectly circular polar orbit. In the sequel one more error source will be added per test case. The second one will use a circular orbit with a GOCE-like inclination of $I = 96.6°$ in order to show the effect of the *polar gap*, which is the area around the poles left without observations. The third one will use the realistic orbit from the simulation but keep the satellite perfectly oriented in the orbit system, in order to show the effect of the deviations from a theoretical circular orbit (which is a requirement for the semi-analytical theory). Finally the fourth test case will use the simulated realistic orientation. The satellites orientation will deviate from a nominal orientation in flight direction. This test will asses the effect of this deviation on the solution.

All four cases will use a repeat orbit with 403 revolutions in 25 nodal days to be in line with the simulation. A disturbing potential series T and tensor of second derivatives of the disturbing potential T_{ij} were simulated error-free using the EGM96 model up to degree and order 200 with the GRS80 normal field subtracted. The goal is to reproduce the input model as good as possible. Differences between the coefficients of the solution and the input model can be seen as errors.

Proof of Concept (test case 1) : For a proof of concept a perfectly circular and polar repeat orbit with only the central term of the Earth's gravity field was created. The simulated SGG-observations are perfectly oriented in the LORF.

Using only the central term of the Earth's potential ($J_2 = 0$) and a constant Earth rotation ($\omega_e = 2\pi/86164\,\mathrm{s}$), equation 2.82 leads to $\dot{u} = n = \sqrt{GM/r^3}$ and equation (2.83) to ($\dot{\Lambda} = -\omega_e$). In order to

match the repeat cycle that is used in section 4.2 with the simulation data, the parameters are chosen as $\alpha = 25$ and $\beta = 403$. This results in a constant radius $r = 6607439.914\,\mathrm{m}$ or respectively an orbit height of about 229 km. The duration is $25 \cdot 86164\,\mathrm{s} = 2154100\,\mathrm{s}$. With a sampling rate of 1 s there are 2154100 samples.

Figure 4.1 (left graph) shows, that the 1D-FFT solution converges very fast. After 6 iterations the differences between the solution and the input model reaches numerical accuracy, which is the proof, that the methods works perfectly if all preconditions are fulfilled.

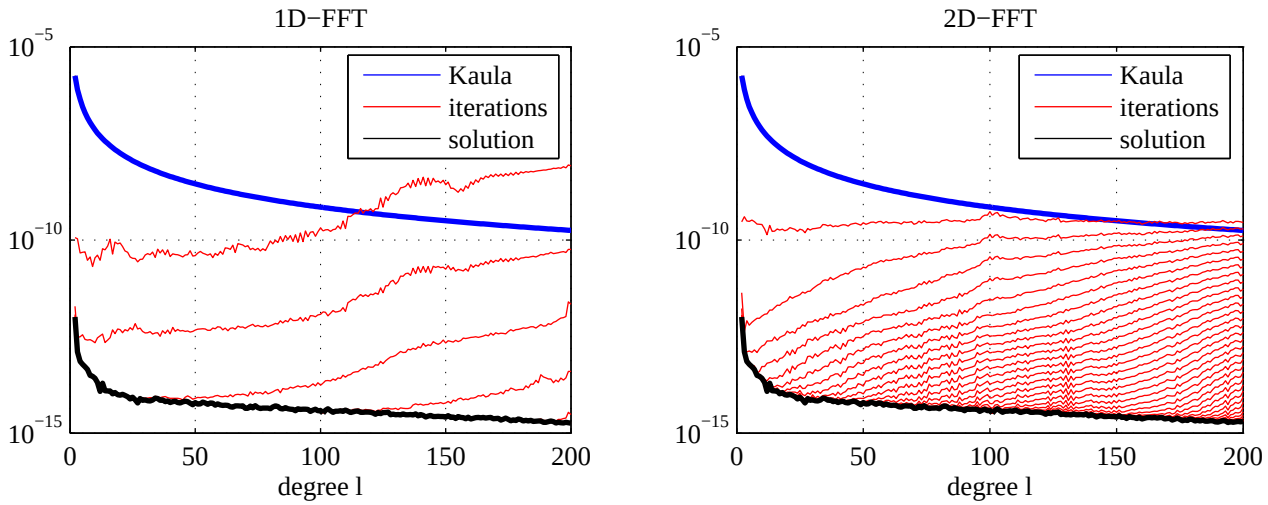

Figure 4.1: Degree-RMS-errors obtained by the 1D-FFT (left) and 2D-FFT approach (right) with a perfect simulation.

For the 2D-FFT approach things look different. As can be seen in figure 4.1 (right graph), the numerical accuracy can only be reached after 33 iterations. The reason is, that the interpolation on the torus adds an error to the error-free simulated observations, which is reflected in the solution of the first iteration. The errors can finally be overcome, but the convergence rate is much slower than that of the 1D-FFT.

Effect of the Polar Gap: The second test uses basically the same circular repeat orbit which is now tilted with an inclination of 96.6° leaving a gap of 6.6° at both poles without observations. This leads to a severe degradation of the system of normal equations. As the semi-analytic approach has a block-diagonal system of normal equations, the systems of normal equations corresponding to a certain order m can be analyzed separately. Figure 4.2 shows the condition numbers of the systems of normal equations per order for a polar orbit (green curve) and an inclined orbit(blue curve). It is evident that below order $m = 16$ towards order $m = 0$ there is a strong increase in the condition number, which shows that the zonal and near-zonal harmonics are ill-defined. As the relative numerical precision using 64-bit variables is about 10^{-16}, a condition number of 10^{16} would mean that the normal equation matrix is singular w.r.t. the numerical accuracy. The highest condition number for the system with order $m = 0$ is about 10^{10}, which means that the largest coefficients can only be determined with 6 significant digits. As the range of coefficients up to degree and order 200 (with the normal field removed) spans over four orders of magnitude (cf. Kaula's rule), the smallest coefficients can hardly be resolved. It should be noted, that a direct solution is affected by the polar gap in a similar way.

The 1D-FFT solution converges after 15 iterations (cf. fig. 4.3). The degree-RMS-error shows a zigzag pattern as the degree-RMS-error of the even degrees is much higher than that of the odd degrees. Within one order m, only coefficients of the same parity of $(l - m)$ are correlated (cf. equ. 2.86). The symmetry of the polar gap effects the blocks of the normal equations corresponding to even functions more than those corresponding to odd functions. The representation of the error as degree-RMS-errors is misleading, as only the coefficients with low harmonic orders are ill-determined. Therefore it is common to display a degree median error (showing only the median error of all coefficients within one degree) which is displayed by the green curve in figure 4.3. This is as well misleading as it hides the

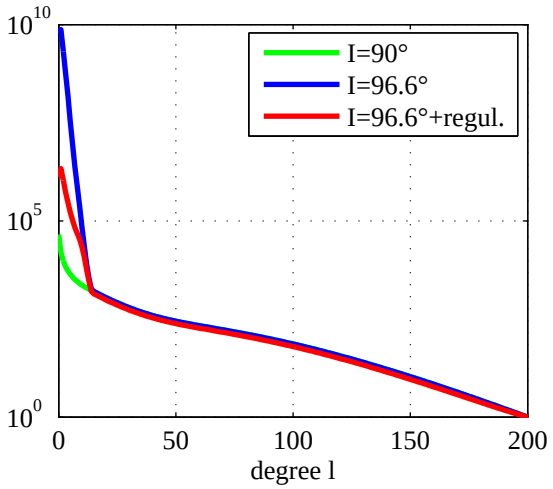

Figure 4.2: Condition numbers of the system of normal equations per order m.

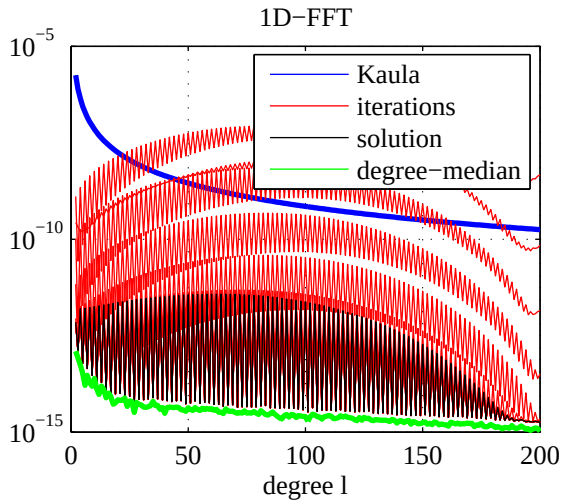

Figure 4.3: Degree-RMS-Errors obtained by the 1D-FFT approach with an inclined orbit.

large errors of zonal coefficients and it is more clear to display the errors of each coefficient as its done in figure 4.4 for all four test cases. The 2D-FFT solution reaches a similar result but again needs more than 30 iterations to converge.

If the coefficient errors are converted to the spatial domain, e.g. geoid height errors, only geoid heights located directly inside the polar gap areas obtain errors of up to 15 cm, while for the largest part of the Earth, errors stay well below the mm-level.

Effect of a Realistic Orbit and Orientation (test case 3): For the third test a part of the orbit from the SIM-data will be used with simulated error-free observations along this orbit. The tensor T_{ij} is still perfectly oriented in the LORF. The orbit is no longer circular as a realistic force model has been used to simulate the orbit. However a repeat-cycle with $\beta = 403$ revolutions in $\alpha = 25$ days could be found. The duration of this cycle is not exactly 25 nodal days but it is about 6000 seconds longer, which indicates, that all orbit parameters will differ slightly from the theoretical orbit, which is defined by α and β.

Figure 4.4 shows, that the coefficient errors of both the 1D-FFT and 2D-FFT solution are much larger than those of test case 2 but apparently the 2D-FFT solution has been affected less. Especially a wedge of near-zonal coefficients obtained large errors. The 1D-FFT solution did not converge at all unless regularization was applied.

The deviation of the real orbit from the theoretical circular orbit introduces an error in the measurements, as the measurements are observed at a slightly different location than they are assumed to be. This error prevents, that the solution converges with numerical accuracy and the solution has significant errors despite the error-free observations. The error is amplified by the ill-posedness of the normal equations. An ill-posed system of linear equations corresponds in the two-dimensional case to the intersection of two straight lines under a very small angle. If these lines are well defined (error free), the point of intersection is still well defined. But if the lines contain an uncertainty, the point of intersection becomes very weakly defined. This explains, why the error of the near-zonal coefficients is so much larger than for test case 2.

Effect of the Satellite's Misorientation (test case 4): In addition to test case 3, the simulated orientation of the satellite is used which differs from the nominal along-track orientation by up to $\sim 3°$ as shown in figure 4.5. This poses a problem for the semi-analytic approach, as the gradiometer

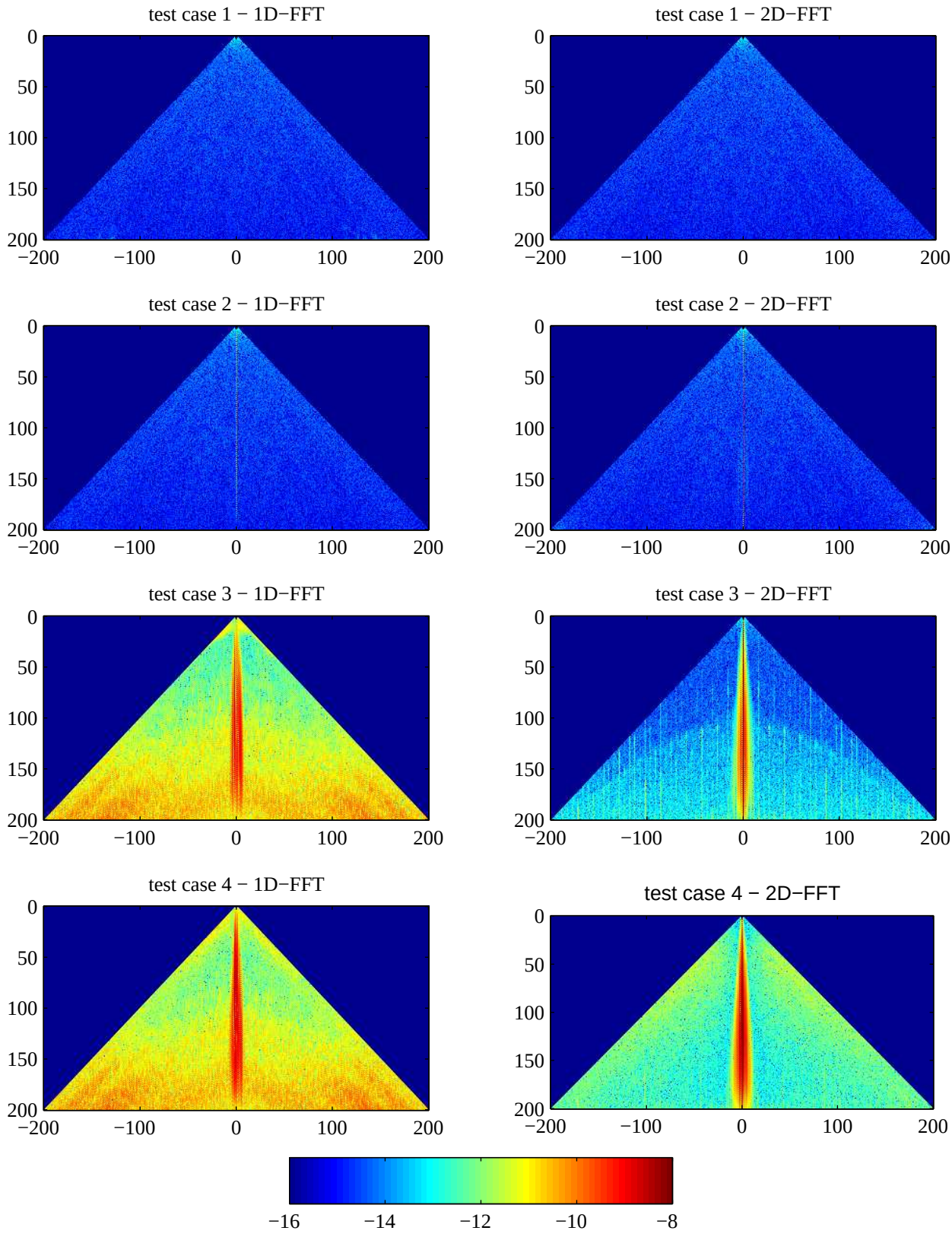

Figure 4.4: Coefficient errors of the four test cases. 1D-FFT left column, 2D-FFT right column.

measurements cannot be rotated to the nominal orientation in the LORF without loss of precision. Due to the lower accuracy of the xy and yz tensor components, a rotation will degrade the other components. The observation equations cannot be rotated to the real orientation – like it is possible for a direct solution – as the semi-analytic approach is defined in the nominal orbit frame and the SGG-observations have to be used as they are.

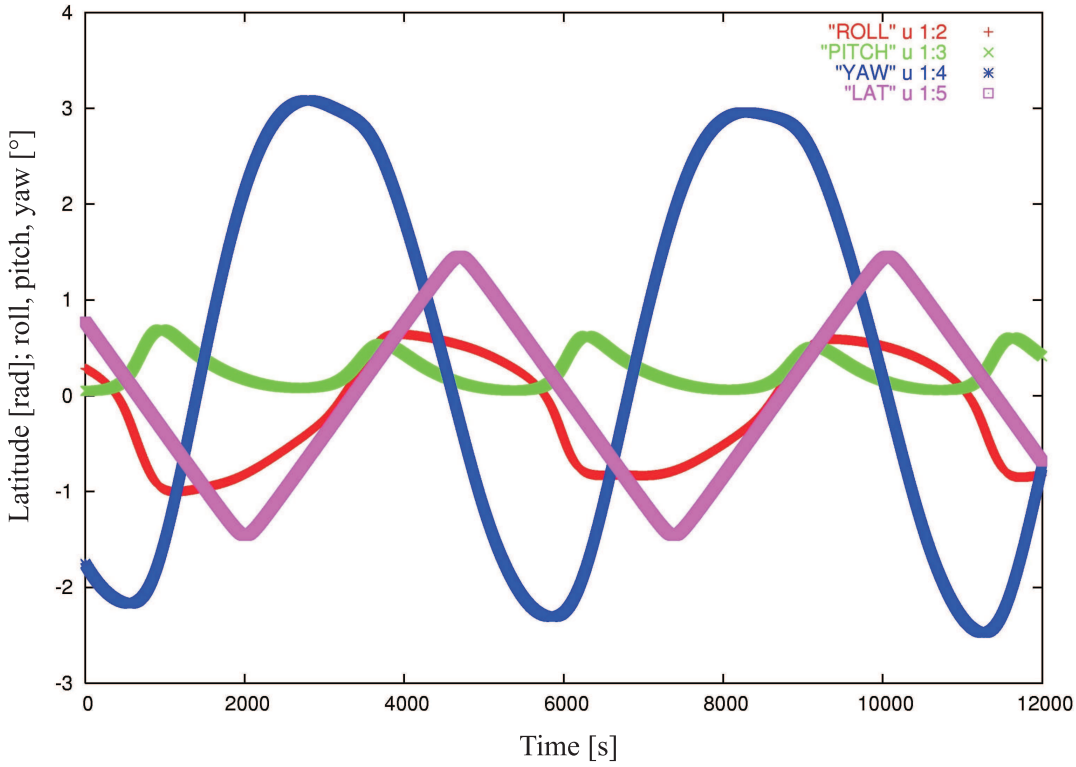

Figure 4.5: Deviation of the satellite's orientation from the flight direction in roll, pitch and yaw (source:ESA).

Figure 4.4 shows that the results have further deteriorated for both approaches, and the 2D-FFT approach is again less affected. Especially the sectorial coefficients have been affected. In conclusion one can state that both approaches are affected by the deviations from the requirements of the semi-analytical approach. The accuracy of the solution can not reach reach that of direct solution. The error introduced by the deviations is amplified in the solution by the ill-condition of the normal equations. The 1D-FFT approach is affected most by the orbit configuration, while the 2D-FFT solution is more effected by the misorientation of the satellite. In general, the 2D-FFT approach seems to perform better in this error-free test.

Contribution Analysis: Figure 4.6 shows the contribution of the SST component, the six tensor elements and the regularization matrix to the coefficients. All contributions sum up exactly to one. It should be noted, that this only reflects the geometry of the repeat orbit with $\beta = 403$ revolutions in $\alpha = 25$ days and the orbit inclination $I = 96.6$ and not the error characteristics of the observations.

The solution below degree 20 is dominated by SST. Above that the influence of SST is declining towards the higher degrees and above degree 50 SST has almost no influence. Out of the SGG components, the V_{zz}-component is the most important with a contribution of up to 36% for all coefficients, that are not dominated by SST or the polar gap. The wedge of coefficients with low harmonic order $m < 16$, that is caused by the orbit inclination is clearly visible. The contributions to coefficients below degree 100 inside this wedge have an irregular distribution. Above degree 100 the regularization matrix seems to

have a stabilizing influence. It should be noted, that without regularization applied, the contributions in this wedge show an erratic behavior. Some would even obtain values above 1 or below 0.

One advantage of the semi-analytical approach is, that regularization can be applied more selective. If the regularization as described in section 2.4 is applied to a full least squares solution, the regularization would contribute to all coefficients of high spherical harmonic degrees. This is an undesired effect as coefficients of orders larger than 16 can be estimated well without regularization. Hence here the regularization is applied only to the blocks of the system of normal equation that correspond to orders below $m = 16$.

4.2 Simulation with Realistic Noise

The SIM simulation contains about 60 days of observations covering 957 revolutions. The SGG-observations are simulated using the EGM96 model up to to degree and order 200 at a sampling rate of 1s. This leads to 5.1 million samples. The orbits are distributed irregularly as can be seen in figure 4.7. Some ground tracks are clustered, which leaves irregular gaps. This means, that the β/α-ratio is not constant over the whole period, and a repeat cycle spanning all or most of the simulation cannot be found. The best-fitting repeat-cycle that could be found in the data set is – as mentioned before – a period of 25 days containing 403 revolutions. It has a very regular ground track distribution as shown in figure 4.8. According to the Nyquist-theorem, the minimum number of required revolutions is $N = 2L_{\max}$ (cf. Sneeuw (2000)). Hence a solution to degree $L_{\max} = 200$ is just possible but the redundancy in Λ-direction is very low. The repeat-cycle has to be used for a 1D-FFT solution – not making use of the full data set, while the whole period of 60 days can be used for a 2D-FFT solution. As both, the SST and SGG observations contain realistic noise and data gaps, they have to undergo a preprocessing step. The simulation contains no tides and uses only a simplified Earth rotation with a constant $\boldsymbol{\omega}$.

SST-Preprocessing – Energy Balance: The GPS observations are not synchronized with the gradiometer and star tracker observations. For the quick-look analysis a rapid science orbit (RSO) is used, which is available with a very short latency after the measurement, but reduced accuracy compared to a precise science orbit (PSO). The rapid science orbit is only available in 10s sampling, while the SGG observations are available in 1s sampling. Hence the SST and SGG observations have to be synchronized by interpolating the orbit positions to the gradiometer epochs. This is done using a Newton-Gregory interpolation (equ. A.9) over seven points. The RSO will be available as either kinematic or reduced dynamic orbit. Contrary to the CHAMP gravity field solution in chapter 3, and to the high-quality GOCE solution based on the Energy Balance Approach (cf. Pail et al. (2006a)), it has been chosen to use the reduced dynamic orbit for the semi-analytic quick-look processing for two reasons: the noise of the kinematic RSO will be about one order of magnitude larger than that of the PSO (e.g. $\sigma_x > 10\,\text{cm}$). This would lead to large velocity errors – even if a smoothing algorithm for velocity derivation would be applied – which would propagate to the disturbing potential values. The second reason is, that it is not a requirement for quick-look processing to derive a solution independent of a priori information (which would make the use of the kinematic orbit necessary). In addition the reduced dynamic orbit already contains the full state-vector at any epoch. Velocity derivation as discussed in chapter 3 is not necessary.

The algorithm applied for the derivation of the disturbing potential values from the orbit via the energy balance is basically the same as described in section 3.1, but has some differences. Due to the drag-free-control the orbit is not sinking like the CHAMP-orbit (cf. fig. 3.1), but the altitude is not constant either. In figure 4.9 it can be seen, that the orbit is oscillating between 231 km and 247 km due to the orbit eccentricity (black curve). With the orbit frequency filtered out (red curve), it becomes apparent, that the orbit is rising slowly from a mean altitude of 239.9 km to 240.2 km over the 25 days (of the

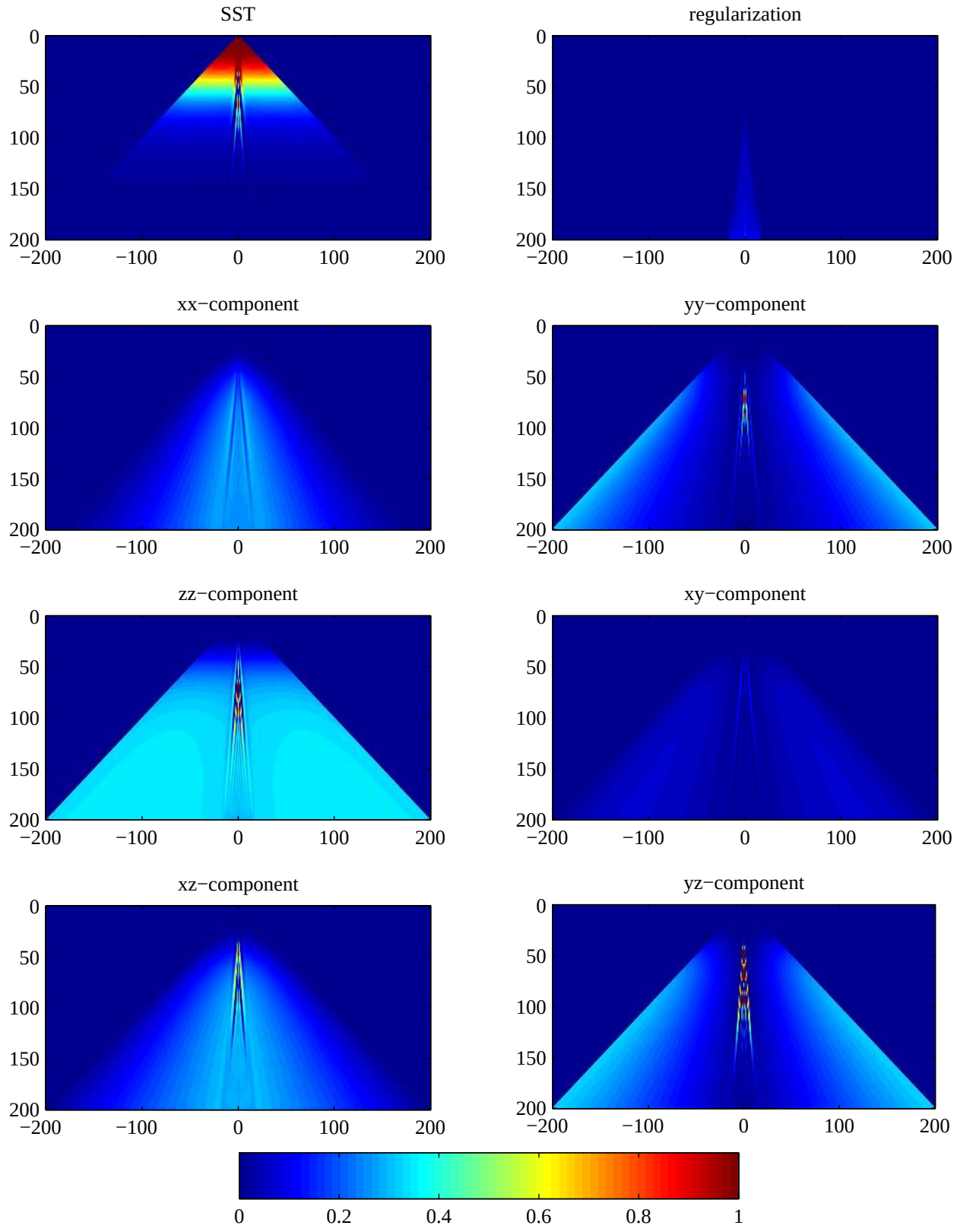

Figure 4.6: Contributions of the different components to the solution. Sum of all contribution is 1.

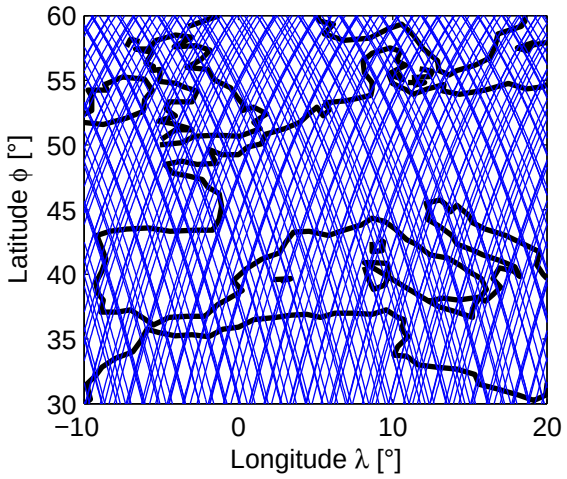

Figure 4.7: Orbit coverage of the full data set over a selected area.

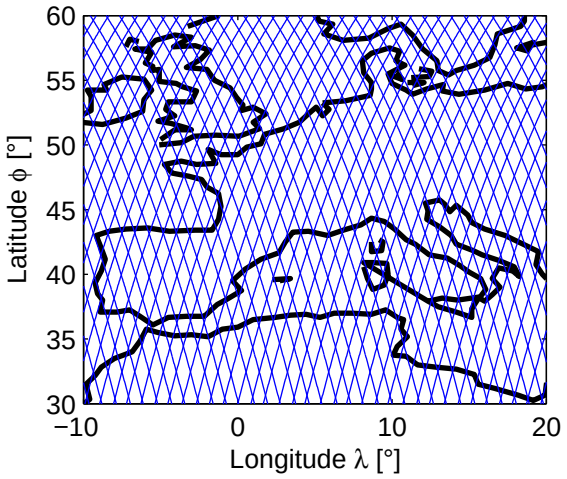

Figure 4.8: Orbit coverage of the repeat-cycle over a selected area.

repeat cycle). This means, that the DFACS which is only compensating drag in the measurement bandwidth is (in this simulation) slightly overcompensating in the long run.

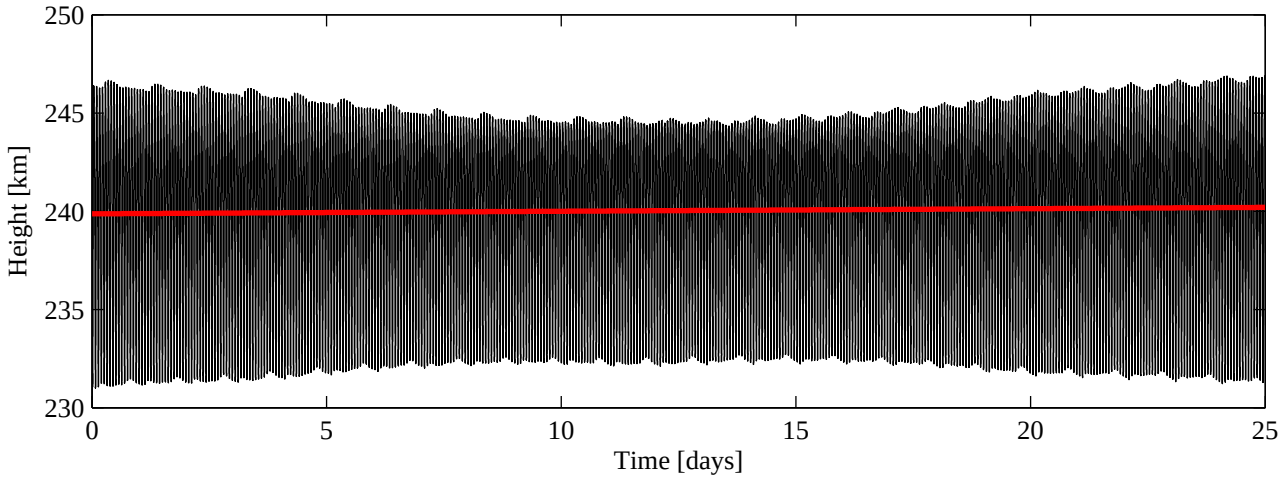

Figure 4.9: Orbit height.

This overcompensation, which means that the DFACS is adding energy to the system, can be seen as well in the disturbing potential after normal potential and centrifugal potential have been removed from the kinetic potential. Figure 4.10 shows the potential $T = \frac{1}{2}\dot{\mathbf{r}}_e^2 - U - \frac{1}{2}\left(\boldsymbol{\omega} \times \mathbf{r}_e\right)^2 - C$ (where the constant C has been approximated by the mean of the time series) is slowly increasing, indicating, that energy is added to the system. It should be noted comparing figure 4.10 with figure 3.10, that the addition of energy by the DFACS is about factor 10 smaller than the energy loss of CHAMP during the same period.

The remaining forces on the satellite, which are not compensated by the DFACS are at least one order of magnitude smaller, than the uncompensated accelerations would be. Nevertheless, the common mode accelerations contain an unknown constant bias and long-periodic errors (meaning longer than one day). Integrated along the orbit, this will lead to a drift and long-periodic errors in the correction term for external forces. Figure 4.11 shows this correction $\int \mathbf{a}_{se} d\mathbf{r}_e$, after a linear trend has been removed. It can be seen, that mainly a daily signal remains, which is smaller than $\pm 10\,\mathrm{m}^2/\mathrm{s}^2$. After removing this short wavelength signal from the disturbing potential, a long wavelength signal of $\pm 500\,\mathrm{m}^2/\mathrm{s}^2$ remains.

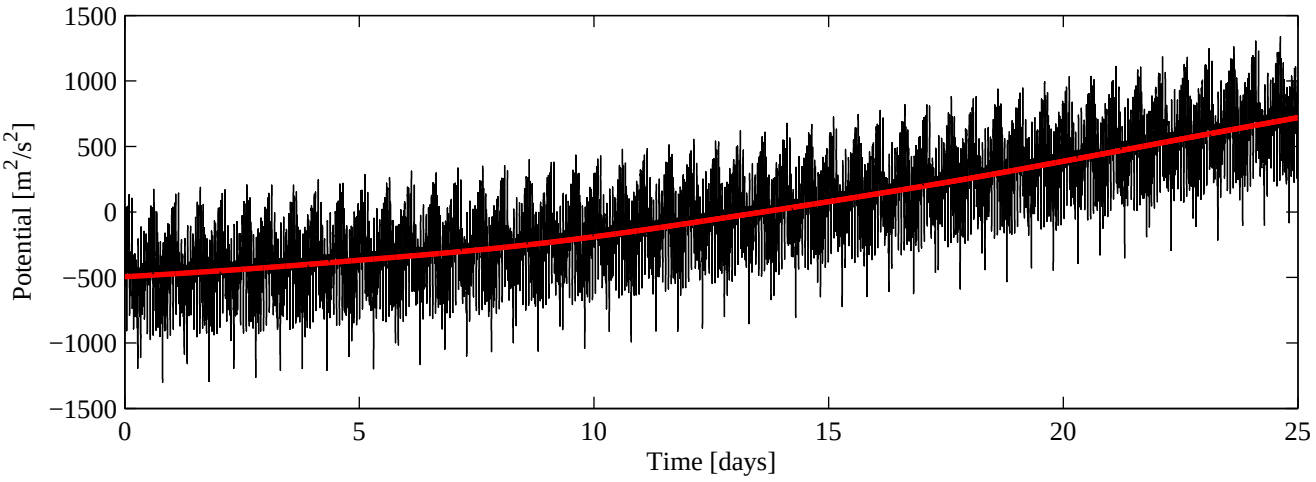

Figure 4.10: $T = 1/2\dot{\mathbf{r}}_e^2 - U - 1/2(\boldsymbol{\omega} \times \mathbf{r}_e)^2$*-C.*

This signal is caused by unknown accelerometer errors.

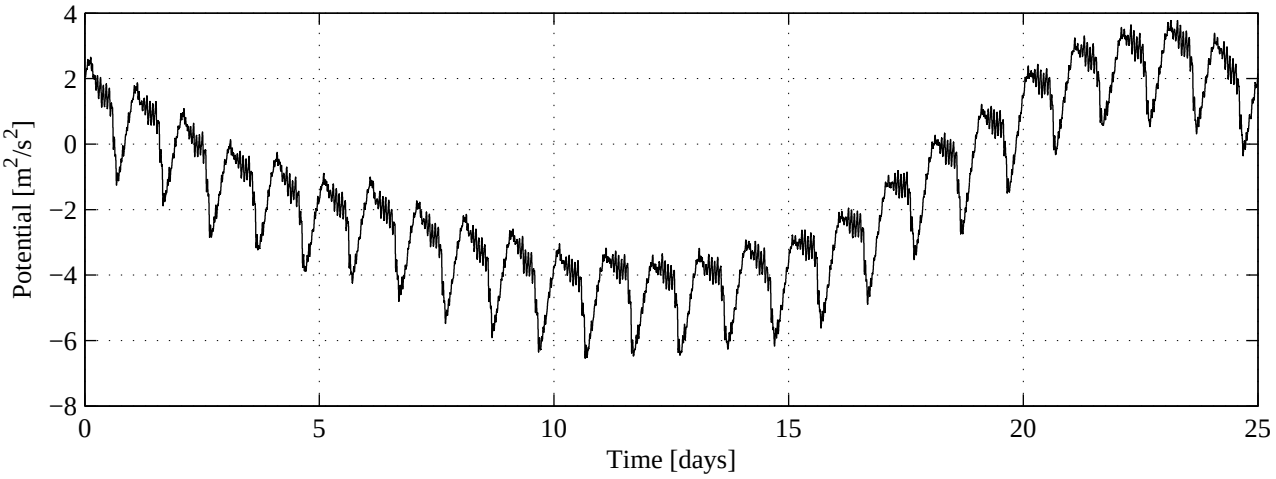

Figure 4.11: $\int \mathbf{a}_{se} d\mathbf{r}_e$ *(linear trend removed).*

The two methods proposed in section 3.1 for the removal of the uncompensated accelerometer errors from the CHAMP data are not applicable here. The algorithm to estimate a long-periodic error using an a priori gravity model, would use too much computation time due to the higher sampling rate. The estimation of additional unknown parameters like accelerometer biases is not possible with a semi-analytic solution. Hence it was proposed by Pail et al. (2006b) to estimate the additional parameters in a smaller least-squares adjustment with a reduced set of unknowns and eliminate their corresponding signal from the data, before the actual semi-analytic adjustment.

In this case the signal to be eliminated, $f(t)$, is the uncompensated potential due to long-periodic accelerometer errors. The data is divided in several parts of equal length (e.g. one day). The error function $f(t)$ is parameterized as a linear combination of Legendre polynomials P_n (which form an orthogonal set of functions in the domain [-1 1]) over each part:

$$f(t) = \sum_{n=0}^{N} a_n \cdot P_n(\tau) \ , \tag{4.1}$$

where $\tau \in [-1; 1]$ is the normalized time t over one part, ensuring that the argument of the Legendre

polynomials is in the correct domain. The coefficients a_n of all parts are then estimated in a least-squares adjustment together with the zonal coefficients ($m = 0$) of up to degree $l = 20$. If two adjacent orbit parts are not separated by data gaps, a constraint is added to the adjustment to make the function $f(t)$ continuous. By choosing the maximum series expansion of the Legendre polynomials N and the length of the parts one can define the characteristics of error function $f(t)$. For the GOCE simulation, polynomials of oder $N = 2$ over a period of one day are sufficient to describe the uncorrected signal due to external forces well enough. The estimated error function is displayed in figure 4.10 (red curve) and removed from the disturbing potential. By comparing the result – which enters the semi-analytic adjustment – to a time series of disturbing potential computed by synthesis from the input model, one obtains an error standard deviation of $\sigma_T = 1.208\mathrm{m}^2/\mathrm{s}^2$. This is slightly larger than the a posteriori error of the CHAMP adjustment, but acceptable considered, that only a RSO with reduced accuracy was used.

SGG-Preprocessing – Reduction of Systematics: The SGG-observations of the SIM data contain gravity gradients from the input model with realistic instrument noise. In Figure 4.12 the error PSDs of the simulated gravity gradients are displayed. For the V_{xx}, V_{yy} and V_{zz} components, the error stays below the specified accuracy of 10^{-2} E within the measurement bandwidth between 5 mHz and 100 mHz. Below the measurement bandwidth, the error rises with $1/f^2$. The errors of the V_{xy} and V_{yz} are about 2 orders of magnitude larger than those of the diagonal tensor components. The V_{xz} component would meet the requirement in the band from 10 mHz to 100 mHz but the increase towards the low frequencies starts already within the specified MBW and is even steeper than for the diagonal tensor components. Hence it was decided to only use V_{xx}, V_{yy} and V_{zz} for the SGG processing.

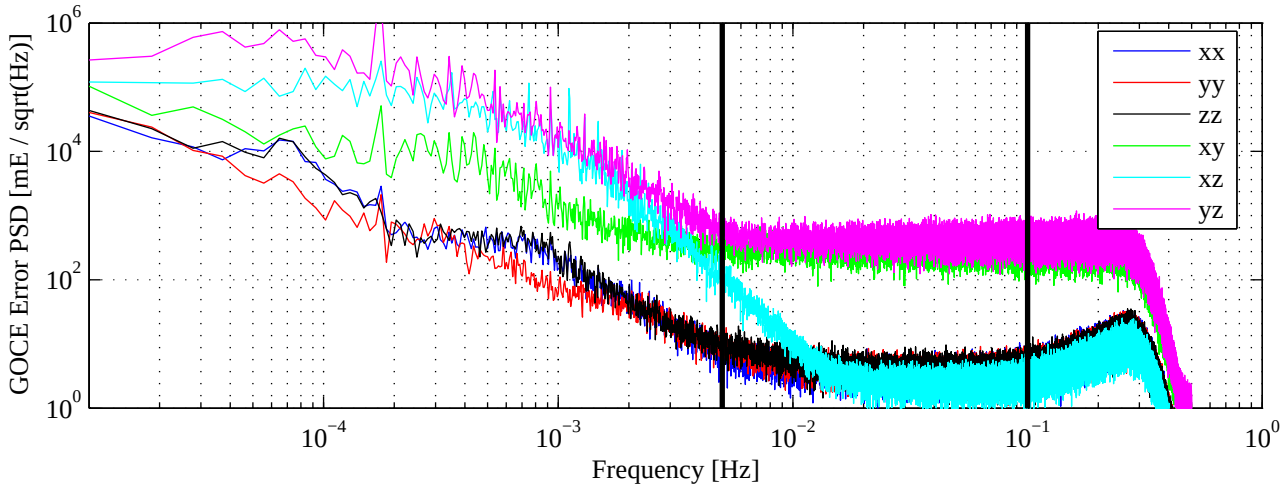

Figure 4.12: Spectral noise behavior of the SGG-observations.

The strong increase of the error spectrum towards the low frequencies generates a random walk in the time domain, which is several orders of magnitude larger than the signal of the normal gravity field. Generally, the observation data does not need to be filtered before the adjustment, when using the semi-analytical approach. The filter will be applied during the adjustment in the spectral domain (see sec. 2.5). Nevertheless it is necessary to reduce the largest long-periodic errors from the observations for two reasons. As the systematic errors are several orders of magnitude larger than the signal, it is numerically more stable to reduce the range of observation values. Especially for the 2D-FFT approach it is important to remove long-periodic errors before the interpolation on the torus. For the interpolation, observations are combined which are geographically close to each other but not necessarily in time. If these observations carry offsets which are larger than the signal itself, the interpolation will completely fail. The reduction of systematic effects is done with the same pre-elimination method proposed by Pail et al. (2006b) as is used for SST-derived potential time series described above. For SGG observations a higher polynomial degree (e.g. $N = 3$) is necessary.

Results 1D-FFT: The solution has been computed combining the disturbing potential T derived by the Energy Balance Approach and the three diagonal components of the tensor T_{xx}, T_{yy} and T_{zz} (with the normal field removed). Filtering in order to account for the spectral noise behavior of the SGG-observations was applied as described Pail et al. (2004). The normal equations for SST have been set up to degree $L_{\mathrm{SST}} = 100$, as the contribution of SST to higher degrees is negligible. For the SGG components normal equations were set up to degree $L_{\mathrm{SGG}} = 200$ to recover the full signal contained in the simulation. The different observables were combined on the level of normal equations. To show the influence of the SST observations, separate solutions were computed using SST only and SGG-only. The degree median errors of the three solutions are compared in figure 4.13. Above degree 20 the solution is dominated by SGG. Below degree the errors of the SGG-only solution strongly increase towards the lower degrees. In this band the solution is supported by SST.

The combined SST and SGG solution converges after 11 iterations. The coefficient errors are shown in figure 4.14. The influence of the polar gap is clearly reflected in the high errors of zonal coefficients. Apart from that the errors seem reasonable. Geoid height differences to the input model are shown in figure 4.15. The error is very large (± 60 m) in the polar areas, which are not covered by observations. But for the rest of the globe which is below the latitude of $\phi < \pm 83°$ the geoid height error stays mostly below 20 cm, and the RMS error is 7.2 cm. This is more than twice as large than what is expected from a direct solution using the same data (cf. Pail et al. (2006a)) but well within the requirements the for quick-look gravity models. The errors are displayed in a Mollweide projection (cf. Snyder (1987)) which is area-accurate. This displays, that the area affected by the polar gap is actually very small.

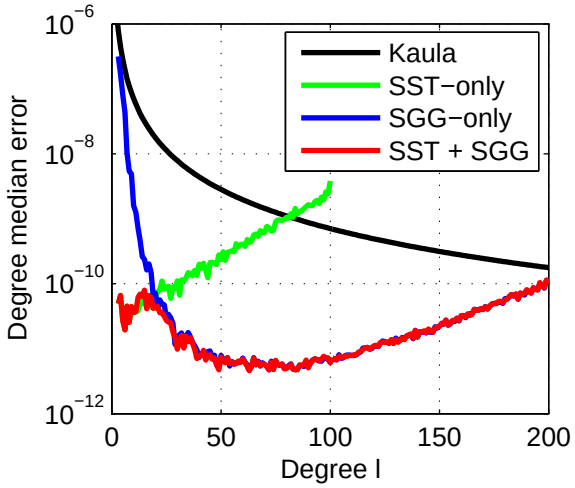

Figure 4.13: Degree median errors of the SST-only, SGG-only and combined SST+SGG solutions.

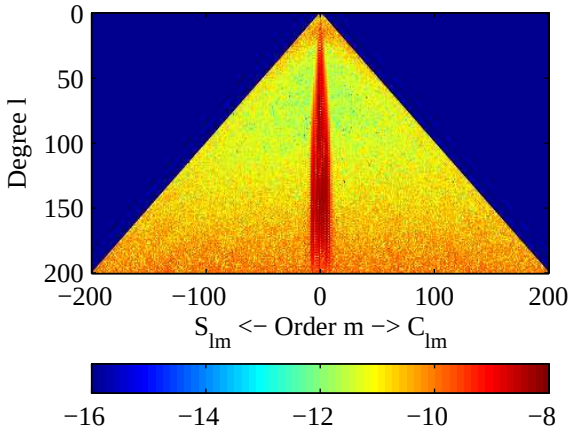

Figure 4.14: Coefficient errors of the 1D-FFT combined SST+SGG solution.

Results 2D-FFT: The solution using the 2D torus approach does not come to a satisfying result. The coefficient errors displayed in figure 4.16 show large errors apart from the polar gap effect. Whole orders of coefficients have been effected. Figure 4.17, which displays the interpolated T_{zz} gradient on the torus explains the reason. The reduction of long-periodic errors from the SGG-observations did obviously not remove all systematic effects from the data. This is reflected in a track-pattern in the interpolated function on the torus. The problem will be further investigated and the reduction of systematic effects or the interpolation on the torus should be improved.

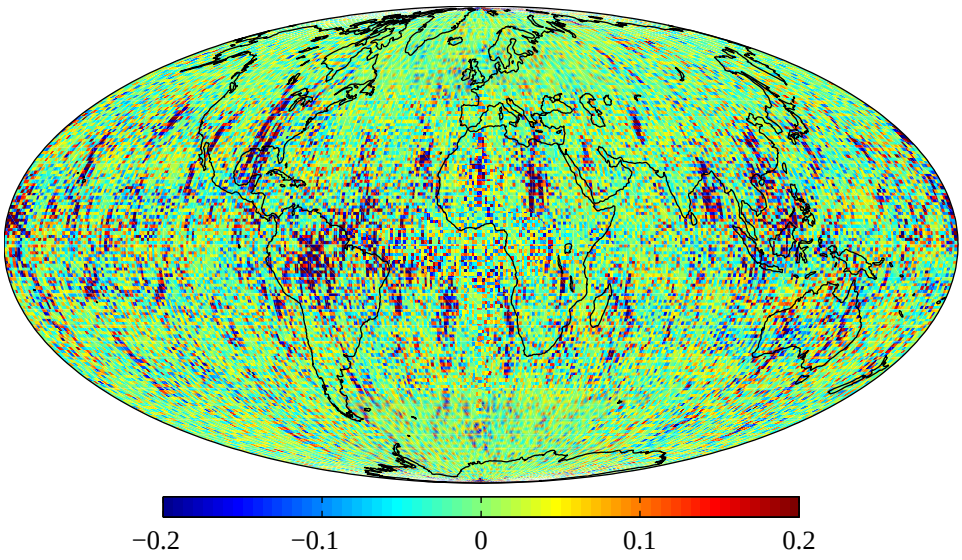

Figure 4.15: Geoid height error [m] of the 1D-FFT solution.

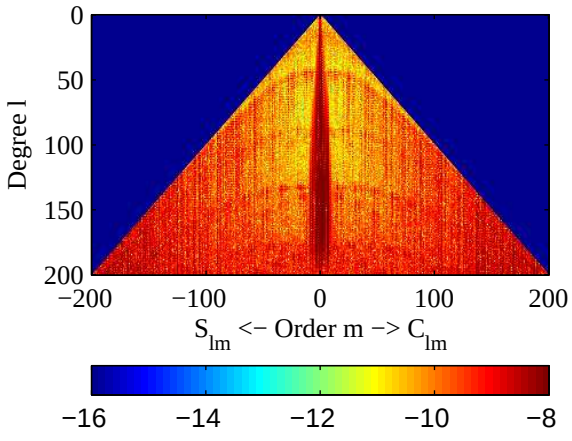

Figure 4.16: Coefficient errors of the 2D-FFT solution.

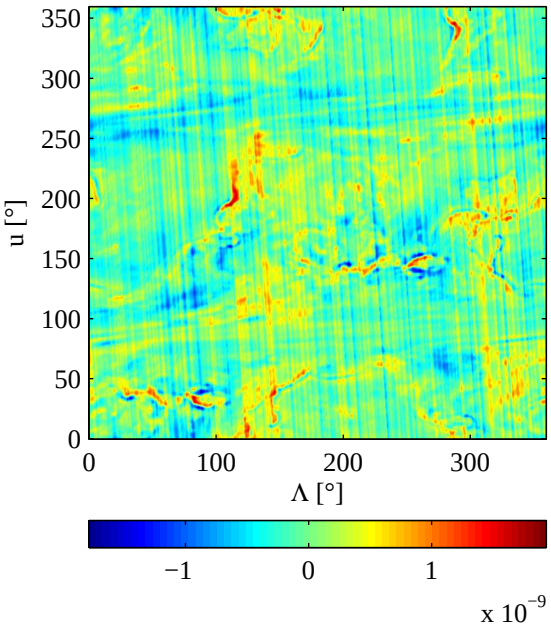

Figure 4.17: T_{zz} interpolated on the torus.

5 Conclusions

In the following some of the findings of this work will be summarized.

Energy Balance Approach: It has been demonstrated, that the Energy Balance Approach is a suitable method for global gravity field determination from hl-SST. The quality of the solution using two years of CHAMP observations is competitive with solutions using alternative approaches (cf. sec. 3.4). Using kinematic orbits it is possible to derive a single satellite gravity field solution independent of a priori models. Therefore the method is suggested for gravity field analysis from future LEO missions which are equipped with a GPS receiver and an accelerometer. The method will also be used for the SST analysis of GOCE (cf. Pail et al. (2006a)). It will complement the SGG-analysis for both, the quick-look and the final (high-quality) solution.

However the method has a weakness in the determination of very low coefficients – especially of the coefficients C_{20} and C_{40}. It seems that due to unknown accelerometer errors, which integrate up to a long-periodic error in the disturbing potential time series, the long-term consistency between the observations is lost. This could be possibly improved by developing a better modeling of accelerometer errors enabling the recovery of long wavelength gravity signal.

The variance/covariance propagation did not work successfully, as no suitable covariance information of the orbits was available. It is recommended to provide covariance information with orbit products and the variance/covariance propagation should be taken up again.

Semi-Analytic vs. Direct Solution: The Semi-analytic approach is a very efficient method for gravity field determination with low requirements of computer resources. Using simplified simulations as in section 4.1 it can provide a quick analysis of the characteristic features of a certain mission design. However using real data or simulations with realistic error assumptions, it cannot compete with a direct adjustment in terms of accuracy.

The degree of degradation of the semi-analytic solution is dependent on the deviation of the real mission data from the theoretical assumptions (e.g. a circular orbit) underlying the semi-analytical approach. For CHAMP the deviations are relatively small and the semi-analytic solution reaches almost the quality of the direct one. Only the small eccentricity and the slow decay of the orbit cause deviations from a circular orbit. Nevertheless it should be noted, that the orbit decay, and the resulting orbit pattern prevented a solution with the 1D-FFT approach. Due to the stable height of the GOCE orbit finding a repeat orbit for the 1D-FFT was possible, although not optimal.

The semi-analytic processing of GOCE SGG observations is affected by an additional error source: the orientation of the satellite. The semi-analytic approach requires observations to be oriented in the local orbit reference system. As GOCE SGG observations are given in a slightly oscillating frame (and cannot be rotated without loss of precision) a considerable error is introduced.

In conclusion it can be stated, that the semi-analytic approach is a good quick-look tool for the GOCE mission, as it will provide a comprehensive and good insight into the performance of the mission. It will also serve as a tool for pre-mission analysis of future gravity field missions, as the performance of possible theoretical mission scenarios can be examined efficiently. But it is not an alternative to a direct full solution for high quality gravity field analysis from real data.

1D-FFT vs. 2D-FFT Solution: Both the 1D-FFT and 2D-FFT approach have certain advantages and disadvantages and it cannot be concluded, that one of the two methods would generally be superior. The choice rather depends on mission characteristics like orbit parameters and observation errors which are different for each mission.

It has been shown in section 4.1 that if the requirements of a perfect circular orbit are met, the 1D-FFT approach delivers the best results. But in reality such a requirement is never met perfectly. The more the real orbit deviates from the theoretical assumptions, the larger the error is. This is due to the fact, that measurements are observed at a location different from what it is assumed to be. In addition, the 1D-FFT approach relies on a constant orbit height as only then a constant repeat cycle is provided. This limits the approach to satellite missions with an active orbit maintenance such as GOCE.

The 2D-FFT approach is less sensitive to orbit geometry. Observations enter the interpolation on the torus at their true location in the (u, Λ) domain. Only deviations from the assumed constant orbit height introduce an error. But the interpolation itself is an error source – especially if the data distribution is very inhomogeneous. As shown in section 4.2, long-periodic errors cause difficulties for the interpolation and are reflected in systematic errors on the torus grid. This is subject to further investigation. It should be possible to remove the systematic errors from the interpolated SGG observations either by using statistic properties of the function on the grid, or by using SST observations.

Acknowledgements

I would like to thank a number of people who have all contributed directly and indirectly to this work. First of all my thank goes to Prof. Reiner Rummel for supervising this thesis and for making it possible for me to work in this interesting field of science. The numerous discussions, helpful comments and ideas have greatly benefited to this work. I would like to thank Prof. Nico Sneeuw for accepting the position as second advisor and for initially introducing me to gravity field analysis by supervising my diploma thesis.

Furthermore I would like to thank all colleagues of the *Institut für Astronomische und Physikalische Geodäsie*, the EGG-C and the GOCE-GRAND projects for successful cooperation and for the excellent atmosphere. I am grateful in particular to Prof. Christian Gerlach and Dr. Lorant Földváry for cooperation and many discussions concerning the Energy Balance Approach, Dipl.-Ing. Drazen Švehla for providing the CHAMP-orbits, Prof. Roland Pail for the cooperation in semi-analytic gravity field solution and Dr. Thomas Gruber for providing the geoid validation test.

Last but not least I have to mention my family and friends who have supported me during the last years.

This work was funded by the programme GEOTECHNOLOGIEN of BMBF and DFG, Grant 03F0329A.

A Appendix

A.1 Numerical Differentiation

As mentioned in section 2.2, kinematic positions contain considerable high frequent noise, which is amplified by differentiation, as it corresponds to a multiplication of the spectrum with $i\omega$. These high frequency errors are even squared before they enter the gravity field estimation. So the aim is to smooth the velocities or filter out the high frequency errors without eliminating the gravity signal, which makes the choice of an appropriate differentiation algorithm important.

In order to differentiate an orbit, it is sufficient to derive each of the components separately $\dot{\mathbf{r}} = \mathrm{d}\mathbf{r}/\mathrm{d}t = (\mathrm{d}x/\mathrm{d}t, \mathrm{d}y/\mathrm{d}t, \mathrm{d}z/\mathrm{d}t)^{\mathrm{T}}$. The following derivations are done only for $\dot{x} = \mathrm{d}x/\mathrm{d}t$, representative for all components. Nevertheless it should be considered, that correlations between the components of the position vector are propagated to correlations between the components of the velocity vector (cf. sec 2.2).

Polynomial Differentiation: The fundamental principle underlying many differentiation algorithms of discrete data, is to fit a known analytical function (e.g. an interpolation function) to the sampled values and determine the derivative by analytically differentiating the function. The most obvious choice to differentiate a time-series of n samples, is to use a polynomial of (n-1)th order, as there is only one unique set of n coefficients $(a_0, a_1, ..., a_{n-1})$ which describes the polynomial containing all n interpolation points:

$$x = \sum_{i=0}^{n-1} a_i t^i = a_0 + a_1 t + a_2 t^2 + ... + a_{n-1} t^{n-1}. \tag{A.1}$$

The velocities are obtained by differentiation of the polynomial:

$$\dot{x} = \sum_{i=1}^{n-1} i a_i t^{i-1} = a_1 + 2a_2 t + ... + (n-1) a_{n-1} t^{n-2} \ . \tag{A.2}$$

The coefficients a_i are obtained by solving a linear system of equations with n equations and n unknowns:

$$\begin{pmatrix} x_1 \\ x_2 \\ \vdots \\ x_n \end{pmatrix} = \begin{bmatrix} 1 & t_1 & t_1^2 & \cdots & t_1^{n-1} \\ 1 & t_2 & t_2^2 & \cdots & t_2^{n-1} \\ \vdots & \vdots & \vdots & \ddots & \vdots \\ 1 & t_n & t_n^2 & \cdots & t_n^{n-1} \end{bmatrix} \begin{pmatrix} a_0 \\ a_1 \\ \vdots \\ a_{n-1} \end{pmatrix} \tag{A.3}$$

As the linear system of equations becomes ill-posed for high orders and the computational effort rises, it is advisable to compute the polynomial not over the whole time-series, but only in a short window which moves over the whole time series, making the differentiation only for the central point of the window.

The computation can be made even more effective, if the polynomial is restrained to an odd number of interpolation points n, assuming all points are equidistant, with the sampling rate h and the polynomial

is evaluated only at the central point. If this central point is defined as x_0 at $t_0 = 0$, the moving window contains the points $x_{-(n-1)/2}, ..., x_0, ...x_{(n-1)/2}$ from $t_{-(n-1)/2} = -(n-1)/2 \cdot h$ to $t_{(n-1)/2} = (n-1)/2 \cdot h$, and equation A.2 simplifies to

$$\dot{x} = a_1. \tag{A.4}$$

Thus the solution of the linear system of equations A.3 yields depending on the number of samples used:

$$n = 3 \quad => \quad \dot{x}_i = \frac{-x_{i-1} + x_{i+1}}{2h} \tag{A.5}$$

$$n = 5 \quad => \quad \dot{x}_i = \frac{x_{i-2} - 8x_{i-1} + 8x_{i+1} - x_{i+2}}{12h} \tag{A.6}$$

$$n = 7 \quad => \quad \dot{x}_i = \frac{-x_{i-3} + 9x_{i-2} - 45x_{i-1} + 45x_{i+1} - 9x_{i+2} + x_{i+3}}{60h} \tag{A.7}$$

$$n = 9 \quad => \quad \dot{x}_i = \frac{x_{i-4} - 10\frac{2}{3}x_{i-3} + 56x_{i-2} - 224x_{i-1} + 224x_{i+1} - 56x_{i+2} + 10\frac{2}{3}x_{i+3} - x_{i+4}}{280h} \tag{A.8}$$

So the numerical differentiation by polynomials is basically a convolution of the time-series with an anti-symmetric set of coefficients, which can be seen as a MA (moving average) or FIR (finite impulse response) filter (see fig. A.1). It should be noted, that no value can be derived for the first and last $(n-1)/2$ samples of a time-series, as the derivation is only computed for the central point of the moving window. This can be regarded as the warm-up phase of the filter. As a convolution in the time-domain corresponds to a multiplication of the spectrum in the frequency-domain, the spectrum of the orbit is multiplied by the spectrum of the filter coefficients. This is analyzed in section 3.1 and 4.2.

12f		*x*	$\dot{x}$
1		1	
-8		3	
0	*	5	1.75
8		6	-0.50
-1		4	-2.67
		1	-3.83
		-3	-2.83
		-4	0.83
		-2	
		-1	

60f		*x*	$\dot{x}$
-1		1	
9		3	
-45		5	
0	*	6	-0.51
45		4	-2.67
-9		1	-3.87
1		-3	-2.97
		-4	
		-2	
		-1	

Figure A.1: Polynomial interpolation as convolution over $n = 5$ samples (left) and $n = 7$ samples (right).

An alternative representation of equation A.1, which is more efficient in the case of an irregular sample distribution is the Newton-Gregory interpolation:

$$x = a_0 + a_1(t - t_1) + a_2(t - t_1)(t - t_2) + ... + a_{n-1}(t - t_1)(t - t_2)...(t - t_{n-1}), \tag{A.9}$$

where the coefficients $(a_0, a_1, ..., a_{n-1})$ are computed by successive difference ratios:

$$a_0 = x_1;\ a_1 = \frac{x_2 - x_1}{t_2 - t_1};\ a_2 = \frac{\frac{x_3 - x_2}{t_3 - t_2} - \frac{x_2 - x_1}{t_2 - t_1}}{t_3 - t_1}; ... \ . \tag{A.10}$$

The derivation is obtained by:

$$\dot{x} = a_1 + a_2((t-t_2)+(t-t_1)) + a_3((t-t_2)(t-t_3)+(t-t_1)(t-t_3)+(t-t_1)(t-t_2)) + \dots \,. \quad \text{(A.11)}$$

The computation can be efficiently vectorized using a difference table (see fig. A.2), as it is also a moving window running over the time-series. Note that for the simplicity of the example a constant sampling rate was used and the differentiation is done for the central point of a 5-point window. This yields exactly the same result as shown in figure A.1. The advantage of the Newton-Gregory algorithm lies in interpolating and differentiating time-series with non-constant sampling intervals, as applied in section 4.2, as the computation of the difference table is more effective than solving a linear system of equations for each point.

x	a_0	a_1	a_2	a_3	a_4	$\dot{x}$
1	1					
3	3	2				
5	5	2	0			
6	6	1	-0.5	-0.17	-0.04	1.75
4	4	-2	-1.50	-0.33	0.17	-0.50
1	1	-3	-0.50	0.33	-0.08	-2.67
-3	-3	-4	-0.50	0	0.17	-3.83
-4	-4	-1	1.50	0.67	-0.17	-2.83
-2	-2	2	1.50	0	-0.17	0.83
-1	-1	1	-0.50	-0.67		

Figure A.2: 5-point Newton-Gregory differentiation.

Smoothing Polynomial Differentiation: The Polynomials determined in the previous paragraph have the disadvantage, that they pass exactly through every interpolation point including its error. Additionally they are overshooting at the edges, so that the $(n-1)/2$ points at the begin and end of the time-series can only be derived with large errors. However if one uses more points for the determination of the polynomial than necessary ($n > o+1$ where n is the number of samples and o the order of the polynomial), which leads to an overdetermined system of equations, the polynomial becomes a smoothing curve, which no longer passes exactly through each interpolation point. The polynomial coefficients a_i can be estimated in a least squares adjustment:

$$\mathbf{a} = \left(\mathbf{A}^{\mathrm{T}}\mathbf{A}\right)^{-1}\mathbf{A}^{\mathrm{T}}\mathbf{x}, \quad \text{(A.12)}$$

where $\mathbf{a}$ is the vector of polynomial coefficients, $\mathbf{x}$ the values of the time-series, and $\mathbf{A}$ the $(n, o+1)$-matrix containing the partial derivatives of the polynomial (equ. A.1) w.r.t. the polynomial coefficients a_i:

$$\mathbf{A} = \begin{bmatrix} 1 & t_1 & t_1^2 & \cdots & t_1^o \\ 1 & t_2 & t_2^2 & \cdots & t_2^o \\ \vdots & \vdots & \vdots & \ddots & \vdots \\ 1 & t_n & t_n^2 & \cdots & t_n^o \end{bmatrix}. \quad \text{(A.13)}$$

Also in the overdetermined case filter coefficients, which are referred to as Savitzky-Golay coefficients (cf. Savitzky and Golay (1964)) can be easily estimated for the central point of an odd number of points with constant sampling interval. Using equation (A.4) only the second row of $(\mathbf{A}^{\mathrm{T}}\mathbf{A})^{-1}\mathbf{A}^{\mathrm{T}}$, which contains the filter coefficients needs to be computed.

Here again, the formula can be simplified, if one determines a 2nd-order polynomial at the central point of an odd number of equidistant points (cf. Lanczos (1956)):

$$\dot{x} = \frac{\sum_{\alpha=-k}^{+k} \alpha f\left(x + \alpha h\right)}{2\sum_{\alpha=1}^{k} \alpha^2 h} \tag{A.14}$$

where $k = (n-1)/2$. For $k = 1, n = 3$ the system is not overdetermined, and the differentiation becomes:

$$\dot{x}_i = \frac{x_{i+1} - x_{i-1}}{2h}, \tag{A.15}$$

which is equal to equation (A.5). This is the most simple form of numerical differentiation. For $k = 2, k = 3$ and $k = 4$, the equations become:

$$k = 2, n = 5 \quad => \quad \dot{x}_i = \frac{-2x_{i-2} - x_{i-1} + x_{i+1} + 2x_{i+2}}{12h} \tag{A.16}$$

$$k = 3, n = 7 \quad => \quad \dot{x}_i = \frac{-3x_{i-3} - 2x_{i-2} - x_{i-1} + x_{i+1} + 2x_{i+2} + 3x_{i+3}}{28h} \tag{A.17}$$

$$k = 4, n = 9 \quad => \quad \dot{x}_i = \frac{-4x_{i-4} - 3x_{i-3} - 2x_{i-2} - x_{i-1} + x_{i+1} + 2x_{i+2} + 3x_{i+3} + 4x_{i+4}}{60h} \tag{A.18}$$

A.2 Base Functions

A.2.1 Legendre Functions

The closed analytical form of the *fully normalized associated Legendre functions* (equ. 2.4) is not suited for numerical computations. The functions and their first and second order derivatives can easily be computed by recurrence relations instead (cf. Gerstl (1980)). For convenience the following substitutions were made: $\bar{P}_{lm} = \bar{P}_{lm}(\cos\theta)$, $\bar{P'}_{lm} = \frac{\partial \bar{P}_{lm}(\cos\theta)}{\partial\theta}$ and $\bar{P''}_{lm} = \frac{\partial^2 \bar{P}_{lm}(\cos\theta)}{\partial\theta^2}$. The recursive computation starts with $\bar{P}_{00} = 1$, or $\bar{P'}_{00} = 0$ and $\bar{P''}_{00} = 0$ respectively, using equation (A.19) (dashed arrows in fig. (A.3)) until $\bar{P}_{mm}$ is computed.

$$\bar{P}_{ll} = W_{ll} \sin\theta \bar{P}_{l-1,l-1} \ , \tag{A.19a}$$

$$\bar{P'}_{ll} = W_{ll}(\cos\theta \bar{P}_{l-1,l-1} + \sin\theta \bar{P'}_{l-1,l-1}) \ , \tag{A.19b}$$

$$\bar{P''}_{ll} = W_{ll}(-\sin\theta \bar{P}_{l-1,l-1} + 2\cos\theta \bar{P'}_{l-1,l-1} + \sin\theta \bar{P''}_{l-1,l-1}) \ . \tag{A.19c}$$

For $l > m$, the next step is computed by (dotted arrows):

$$\bar{P}_{l,l-1} = W_{l,l+1} \cos\theta \bar{P}_{l-1,l-1} \ , \tag{A.20a}$$

$$\bar{P'}_{l,l-1} = W_{l,l+1}(-\sin\theta \bar{P}_{l-1,l-1} + \cos\theta \bar{P'}_{l-1,l-1}) \ , \tag{A.20b}$$

$$\bar{P''}_{l,l-1} = W_{l,l+1}(-\cos\theta \bar{P}_{l-1,l-1} - 2\sin\theta \bar{P'}_{l-1,l-1} + \cos\theta \bar{P''}_{l-1,l-1}) \ , \tag{A.20c}$$

followed by equation (A.21) (solid arrows) up to $\bar{P}_{lm}$:

$$\bar{P}_{lm} = W_{lm}\left(\cos\theta \bar{P}_{l-1,m} - W_{l-1,m}^{-1} \bar{P}_{l-2,m}\right) \ , \tag{A.21a}$$

$$\bar{P'}_{lm} = W_{lm}\left(-\sin\theta \bar{P}_{l-1,m} + \cos\theta \bar{P'}_{l-1,m} - W_{l-1,m}^{-1} \bar{P'}_{l-2,m}\right) \ , \tag{A.21b}$$

$$\bar{P''}_{lm} = W_{lm}\left(-\cos\theta \bar{P}_{l-1,m} - 2\sin\theta \bar{P'}_{l-1,m} + \cos\theta \bar{P''}_{l-1,m} - W_{l-1,m}^{-1} \bar{P''}_{l-2,m}\right) \ . \tag{A.21c}$$

The normalization factors W_{lm} are computed by

$$W_{11} = \sqrt{3} \,, \tag{A.22a}$$

$$W_{ll} = \sqrt{\frac{2n+1}{2n}} \quad \text{for } \; l > 1 \,, \tag{A.22b}$$

$$W_{lm} = \sqrt{\frac{(2n+1)(2n-1)}{(n+m)(n-m)}} \,. \tag{A.22c}$$

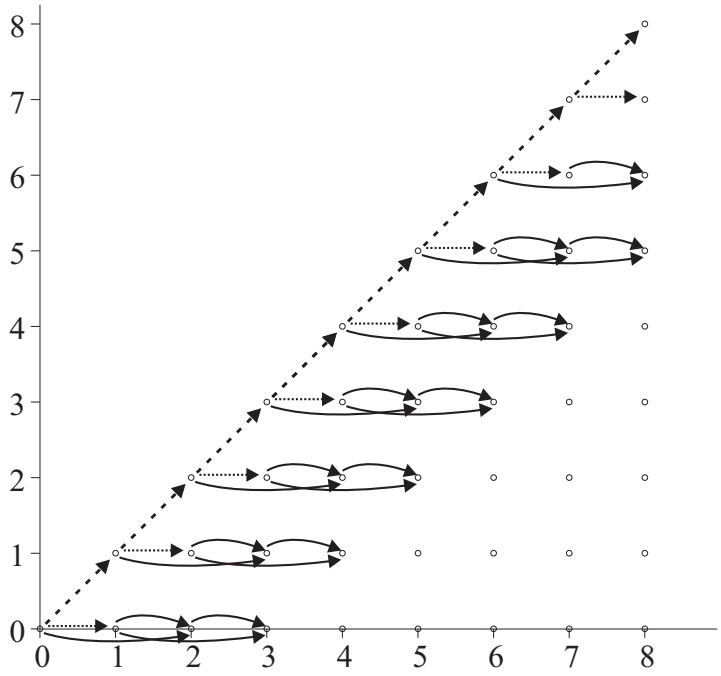

Figure A.3: Recursion scheme for the Legendre functions (from Rummel (1992))

A.2.2 The Inclination Functions

The inclination functions can be very efficiently computed by FFT. This method was introduced by Goad (1987), and its performance was evaluated by comparison with other algorithms by Wermuth (2001). An alternative derivation, which regards the inclination functions as Legendre functions along the orbit and produces the same result, is described in Sneeuw (1991).

If the equations (2.11) and (2.16) are set equal ($V(r,\theta,\lambda) = V(r,I,u,\Lambda)$), one gets after canceling all constant terms and setting all potential coefficients to one:

$$\bar{P}_{lm}(\cos\theta)(\cos m\lambda + \sin m\lambda) = \sum_{k=-l}^{l} \bar{F}_{lmk}(I) \left(\left[\begin{array}{c} \cos\psi_{mk} \\ \sin\psi_{mk} \end{array} \right]_{\mathrm{o}}^{\mathrm{e}} + \left[\begin{array}{c} \sin\psi_{mk} \\ -\cos\psi_{mk} \end{array} \right]_{\mathrm{o}}^{\mathrm{e}} \right) \,. \tag{A.23}$$

Where e stands for $l-m =$ even and o stands for $l-m =$ odd. With a sample orbit $\Omega = \Theta = 0$, $m\Lambda$ becomes 0 and equation (A.23) becomes:

$$\bar{P}_{lm}(\cos\theta)(\cos m\lambda + \sin m\lambda) = \sum_{k=-l}^{l} \bar{F}_{lmk}(I) \left(\left[\begin{array}{c} \cos ku \\ \sin ku \end{array} \right]_{\mathrm{o}}^{\mathrm{e}} + \left[\begin{array}{c} \sin ku \\ -\cos ku \end{array} \right]_{\mathrm{o}}^{\mathrm{e}} \right) \,. \tag{A.24}$$

A discrete Fourier series has the form:

$$f(x) = a_0 + \sum_{k=1}^{K} a_k \cos kx + b_k \sin kx \quad , \tag{A.25}$$

If the left side of equation (A.24) is taken as f, the Fourier coefficients a_k and b_k can be found by comparison of coefficients:

$$a_0 = \left[\begin{array}{c} \bar{F}_{lm0}(I) \\ -\bar{F}_{lm0}(I) \end{array} \right]_{\mathrm{o}}^{\mathrm{e}} \quad , \tag{A.26}$$

$$a_k = \left[\begin{array}{c} \bar{F}_{lmk}(I) + \bar{F}_{lm,-k} \\ -\bar{F}_{lmk}(I) - \bar{F}_{lm,-k} \end{array} \right]_{\mathrm{o}}^{\mathrm{e}} \quad , \tag{A.27}$$

$$b_k = \bar{F}_{l,m,k}(I) - \bar{F}_{l,m,-k} \quad . \tag{A.28}$$

The Fourier coefficients a_k and b_k can be computed by a Fourier transformation of the function $f = \bar{P}_{lm}(\cos\theta)\left[\bar{C}_{lm}\cos m\lambda + \bar{S}_{lm}\sin m\lambda\right]$. For computation it is reasonable to use the FFT-algorithm (Fast-Fourier Transform). The FFT-algorithm works best with a number of samples K which is a power of two. As k is summed from $-l$ to l, the minimum number of required samples is $2L+1$. So K should be a power of two higher than $2L+1$. The $\bar{F}_{lmk}$ result in:

$$\bar{F}_{lm0}(I) = \left[\begin{array}{c} a_0 \\ -a_0 \end{array} \right]_{\mathrm{o}}^{\mathrm{e}} \quad , \tag{A.29}$$

$$\bar{F}_{lmk}(I) = \left[\begin{array}{c} \frac{a_k+b_k}{2} \\ \frac{-a_k+b_k}{2} \end{array} \right]_{\mathrm{o}}^{\mathrm{e}} \quad , \tag{A.30}$$

$$\bar{F}_{lm,-k}(I) = \left[\begin{array}{c} \frac{a_k-b_k}{2} \\ \frac{-a_k-b_k}{2} \end{array} \right]_{\mathrm{o}}^{\mathrm{e}} \quad . \tag{A.31}$$

A.3 Frame Transformation

In order to transform observations and observation equations from the inertial frame to the Earth-fixed frame with highest accuracy, the IERS Standards 2003 (McCarthy and Petit (2003)) have to be applied. It should be noted, that the Earth-fixed reference frame, which is abbreviated ERF in all GOCE-related documents is referred to as TRS (terrestrial reference system) in the IERS Conventions 2003, while the inertial reference frame is labeled IRF in GOCE-documents and CRS (celestial reference system) in the conventions.

The transformation given in the IERS Conventions 2003 is consistent with the IAU 2000 Resolution and consists of three transformations:

$$\mathbf{r}_{\mathrm{i}} = \mathbf{R}^{\mathrm{i}}{}_{\mathrm{e}}\mathbf{r}_e = \mathbf{Q}(t)\mathbf{R}(t)\mathbf{W}(t)\mathbf{r}_{\mathrm{e}} \; . \tag{A.32}$$

The basic idea is that the first transformation $\mathbf{W}(t)$ corrects for the polar motion (e.g. the orientation of the rotation axis in the Earth-fixed system), the Earth-fixed system is transformed to a conventional system, where the rotation axis of the Earth is defined by the polar coordinates (x_p, y_p). The Earth rotation $\mathbf{R}(t)$ is computed in this conventional system and the final transformation $\mathbf{Q}(t)$ accounts for the movement of the rotation axis in the celestial system, which is expressed by the coordinates (X, Y).

Time Scales: Several different time-scales are involved in the computation of the transformation: on the one side, there is the TAI (Temps Atomique International) which defines a uniform time scale by atomic clocks. On the other side there is the UT1 (Universal Time) which is connected to the non-uniform rotation of the Earth.

Both are connected via UTC, which has an integer offset to TAI. Always when the difference (UT1-UTC) approaches 0.6s, a leap-second is inserted by the IERS to keep the difference within ± 0.9s:

$$\mathrm{TAI} - \mathrm{UTC} = N\mathrm{s}\ , \text{where } N \in \mathbb{N}\ . \tag{A.33}$$

This happened once during the lifetime of CHAMP – a leap second was introduced on December 31 2005 and N increased from 32 to 33. Satellite measurements are normally given in the GPS time-scale, which has a constant offset to TAI:

$$\mathrm{TAI} - T_{\mathrm{GPS}} = 19\,\mathrm{s}\ . \tag{A.34}$$

At the introduction of T_{GPS} on January 1 1980, the GPS time-scale which is constant was chosen to coincide with UTC, which had a difference of 19s to TAI at that time, but departed since then. Most of the parameters of the frame transformation are defined in the TT time scale (Temps Terrestre), which has another constant offset to TAI:

$$\mathrm{TT} - \mathrm{TAI} = 32.184\,\mathrm{s}\ . \tag{A.35}$$

The parameter t, which is used in this section is defined as Julian centuries since J2000 (January 1 2000 12h) in the TT time scale:

$$t = \frac{\mathrm{JD(TT)} - 2\,451\,545.0}{36\,525}\ . \tag{A.36}$$

Polar Motion: The transformation of the polar motion is defined by:

$$\mathbf{W}(t) = \mathbf{R}_3(-s')\mathbf{R}_2(x_p)\mathbf{R}_1(y_p)\ , \tag{A.37}$$

where x_p and y_p are the *polar coordinates* of the Celestial Intermediate Pole (CIP) in the terrestrial reference system. The IERS publishes daily values in the `EOP-C04` series, which are defined at 0:00 UTC. The main term $(x, y)_{\mathrm{IERS}}$ can be obtained by linear interpolation of the neighboring values. The polar coordinates have to be corrected for sub-daily variations from ocean tides and nutation:

$$(x_p, y_p) = (x, y)_{\mathrm{IERS}} + (\Delta x, \Delta y)_{\mathrm{tidal}} + (\Delta x, \Delta y)_{\mathrm{nutation}}\ . \tag{A.38}$$

Both corrections are given as coefficients of a series expansion of 71 tidal frequencies and 10 frequencies of the nutation (out of 25 nutation terms only the 10 sub-daily terms have to be applied as correction as the others are already included in the `EOP-C04` data):

$$\Delta x = \sum_j xc_j \cos(\omega_j t) + xs_j \sin(\omega_j t)\ ,\quad \Delta y = \sum_j yc_j \cos(\omega_j t) + ys_j \sin(\omega_j t)\ . \tag{A.39}$$

The amplitudes and frequencies can be taken from tables 5.1 and 8.2 of the IERS-Conventions or the corrections can be computed by the subroutines `ortho_eop` and `PMsdnut` provided by the International Earth rotation and Reference systems Service (IERS). It should be noted, that the polar coordinates

which are given in arcseconds and the corrections which are given in microarcseconds, have to be converted before adding them up.

The quantity s' which provides an exact Greenwich meridian is defined as:

$$s'(t) = \frac{1}{2}\int_{t_0}^{t} (x_p\dot{y}_p - \dot{x_p}y_p)\,\mathrm{d}t \ . \tag{A.40}$$

It is only sensitive to the largest variations in polar motion and can be linearly approximated as:

$$s'(t) = -47\mu\mathrm{as}\,t \ . \tag{A.41}$$

Earth Rotation: The Earth rotation matrix is defined by:

$$\mathbf{R}(t) = \mathbf{R}_3(-\theta) \ , \tag{A.42}$$

where θ is the Earth rotation angle. It is defined as a linear function of the observed time UT1:

$$\theta(T_u) = 2\pi(0.779\,057\,273\,2640 + 1.002\,737\,811\,911\,354\,48\,T_u) \ , \tag{A.43}$$

where T_u is the number of days since J2000 in the UT1 time-scale: T_u = (Julian UT1 date - 2 451 545.0). The difference UT1-UTC is published by IERS as daily values in the EOP-C04 time series and can be linearly interpolated from that table. It should be noted, that the factor 1.00273781191135448 is the ratio between the duration of a solar day and a sidereal day. Thus the angle θ makes one revolution in an observed sidereal day.

Motion of the Rotation Axis: Contrary to the historic representation of precession and nutation by separate transformations **P** and **N**, the orientation of the Earth's rotation axis is now represented by the transformation based on the celestial coordinates of the CIP X and Y:

$$\mathbf{Q} = \begin{pmatrix} 1 - aX^2 & -aXY & X \\ -aXY & 1 - aY^2 & Y \\ -X & -Y & 1 - a(X^2 + Y^2) \end{pmatrix} \cdot \mathbf{R}_3(s) \ , \tag{A.44}$$

where $a = 1/(1 + Z)$ with $Z = \sqrt{}(1 - X^2 - Y^2)$. The expression s can be computed by:

$$s(t) = -\int_{t_0}^{t} \frac{X(t)\dot{Y}(t) - Y(t)\dot{X}(t)}{1 + Z(t)}\mathrm{d}t - s_0 \ , \tag{A.45}$$

where $s_0 = 94\mu$as. The coordinates X and Y can be computed by a polynomial and a series expansion:

$$\begin{aligned} X = \ & - \ 0.016\,616\,99'' + 2004.191\,742\,88''t - 0.427\,219\,05''t^2 && \text{(A.46)} \\ & - \ 0.198\,620\,54''t^3 - 0.000\,046\,05''t^4 + 0.000\,005\,98''t^5 && \text{(A.47)} \\ & + \ \sum_i \left[(a_{s,0})_i \sin(\theta_i) + (a_{c,0})_i \cos(\theta_i)\right] + \sum_i \left[(a_{s,1})_i t \sin(\theta_i) + (a_{c,1})_i t \cos(\theta_i)\right] && \text{(A.48)} \\ & + \ \sum_i \left[(a_{s,2})_i t^2 \sin(\theta_i) + (a_{c,2})_i t^2 \cos(\theta_i)\right] + \delta_X \ , && \text{(A.49)} \end{aligned}$$

$$Y = - 0.006\,950\,78'' + 0.025\,381\,99''t - 22.407\,250\,99''t^2 \quad (A.50)$$
$$- 0.001\,842\,28''t^3 - 0.001\,113\,06''t^4 + 0.000\,000\,99''t^5 \quad (A.51)$$
$$+ \sum_i [(b_{s,0})_i \sin(\theta_i) + (b_{c,0})_i \cos(\theta_i)] + \sum_i [(b_{s,1})_i t \sin(\theta_i) + (b_{c,1})_i t \cos(\theta_i)] \quad (A.52)$$
$$+ \sum_i [(b_{s,2})_i t^2 \sin(\theta_i) + (b_{c,2})_i t^2 \cos(\theta_i)] + \delta_Y \ . \quad (A.53)$$

The a and b coefficients and the arguments θ_i are published in tables by IERS. The quantities X, Y and s can be computed by the subroutine `XYS2000A` provided by IERS. The terms δ_X and δ_Y are corrections due to free core nutation (FCN). They are a published by IERS and have to be applied additionally.

A.4 Tides and Temporal Variations

The effect of tides and temporal variations of the gravity field on the satellite has to be removed from the measurements in order to obtain the signal of the Earth's static gravity field. Therefore these effects have to be computed from models in the form of accelerations on the satellite for the energy balance approach (cf. sec. 2.2), and in the form of gravity gradients for the processing of SGG measurements (cf. sec. 2.3). While for the direct tides there are explicit equations to compute the accelerations and gradients, a set of supplemental potential coefficients $\Delta\bar{C}_{lm}$ and $\Delta\bar{S}_{lm}$ defined for a certain epoch has to be computed for the indirect tidal effects and temporal variations. The accelerations and gravity gradients have then to be obtained by spherical harmonic synthesis (cf. equ. 2.12).

A.4.1 Direct Tides

Direct tides are the gravitational effect of a celestial body on the satellite in a geocentric system. As a celestial body attracts both the satellite and the Earth, the difference of both is used to express the relative attraction of the satellite w.r.t. the center of the Earth (see fig. A.4). This results in a relatively small acceleration, as the geocentric distance $|\mathbf{r}_j|$ to the celestial body is much larger, than the geocentric distance of the satellite $|\mathbf{r}|$:

$$\mathbf{a}_j = GM_j \cdot \left(\frac{\mathbf{r}_j - \mathbf{r}}{|\mathbf{r}_j - \mathbf{r}|^3} - \frac{\mathbf{r}_j}{|\mathbf{r}_j|^3} \right) = GM_j \cdot \left(\frac{\mathbf{l}}{l^3} - \frac{\mathbf{r}_j}{r_j^3} \right) \ . \quad (A.54)$$

The index j denotes the body: $j = 2$ for the moon, $j = 3$ for the sun and $j > 3$ for the planets of the solar system - which are often neglected as their tidal effects are much smaller than that of moon and sun. For an exact computation, the coordinates of $\mathbf{r}_j$ for the celestial bodies can be computed by subroutines provided with the JPL DE405 planetary ephemeris catalogue (Standish (1998)) and the constants GM_j are listed in McCarthy and Petit (2003).

The tidal tensor can be obtained in the geocentric frame by differentiation of the accelerations as given in equation (A.54):

$$\Gamma_j = \frac{GM}{l^5} \begin{pmatrix} 3(x_j - x)^2 - l^2 & 3(x_j - x)(y_j - y) & 3(x_j - x)(z_j - z) \\ 3(y_j - y)(x_j - x) & 3(y_j - y)^2 - l^2 & 3(y_j - y)(z_j - z) \\ 3(z_j - z)(x_j - x) & 3(z_j - z)(y_j - y) & 3(z_j - z)^2 - l^2 \end{pmatrix} \ . \quad (A.55)$$

In order to compute the tidal potential, the acceleration has to be integrated along the path from the center of the Earth to the satellite's position:

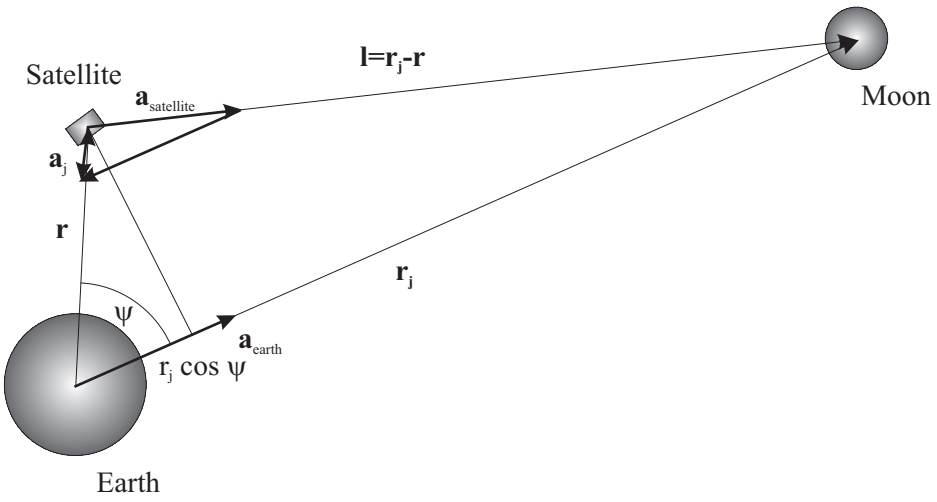

Figure A.4: Relative attraction of the Moon on the Satellite in a geocentric system.

$$V_j = \int_{\mathbf{0}}^{\mathbf{r}} \mathbf{a}_j \mathrm{d}\mathbf{r} = \int_{\mathbf{0}}^{\mathbf{r}} GM_j \cdot \left(\frac{\mathbf{l}}{l^3} - \frac{\mathbf{r}_j}{r_j^3} \right) \mathrm{d}\mathbf{r} = GM_j \cdot \left(\frac{1}{l} - \frac{1}{r_j} - \frac{\mathbf{r}_j\,\mathbf{r}}{r_j^3} \right) \ . \tag{A.56}$$

The scalar product $\mathbf{r}_j\,\mathbf{r}$ can be replaced by $r_j r \cos(\psi)$, where ψ is the angle between $\mathbf{r}_j$ and $\mathbf{r}$ (cf. fig. A.4). The inverse distance $1/l$ may be replaced by a series expansion (cf. Torge (1980)):

$$\frac{1}{l} = \frac{1}{|\mathbf{r}_j - \mathbf{r}|} = \frac{1}{r_j} \sum_{l=0}^{\infty} \left(\frac{r}{r_j} \right)^l P_l(cos\psi) \ , \tag{A.57}$$

where $P_l(\cos\psi)$ are the Legendre Polynomials. The terms of zeroth and first order cancel out when the the series expansion is substituted to equation A.56 and the potential can be written as:

$$V_j = \frac{GM_j}{r_j} \sum_{l=2}^{\infty} \left(\frac{r}{r_j} \right)^l P_l(\cos\psi). \tag{A.58}$$

Often the series expansion is truncated after the second term as it contains about 98 % of the signal and a good approximation equation is obtained:

$$V_j = \frac{3}{4} GM_j \frac{r^2}{r_j^3} \left(\cos 2\psi + \frac{1}{3} \right) \ . \tag{A.59}$$

Using the addition theorems for Legendre functions, equation A.58 can be rewritten as:

$$V_j = \frac{GM_j}{r_j} \sum_{l=2}^{\infty} \left(\frac{r}{r_j} \right)^l \frac{1}{2l+1} \sum_{m=0}^{l} \bar{P}_{lm}(\cos\theta) \bar{P}_{lm}(\cos\theta_j) \, (\cos m\lambda \cos m\lambda_j + \sin m\lambda \sin m\lambda_j). \tag{A.60}$$

This can now be easily converted to a series expansion of the tidal potential on the Earth's surface ($r = R_e$). A set of additional potential coefficients $\Delta\bar{C}_{lm}$ and $\Delta\bar{S}_{lm}$ which represents the additional tidal potential obtained by a simple comparison with equation 2.11:

$$\left. \begin{matrix} \Delta\bar{C}_{lmj} \\ \Delta\bar{S}_{lmj} \end{matrix} \right\} = \frac{1}{2l+1} \frac{GM_j}{GM_e} \left(\frac{R_e}{r_j} \right)^{l+1} \bar{P}_{lm}(\cos\theta_j) \left\{ \begin{matrix} \cos\lambda_j \\ \sin\lambda_j \end{matrix} \right. \tag{A.61}$$

A.4.2 Solid Earth Tides

The gravitational attraction of moon, sun and other celestial bodies does not only affect the gravity potential directly but also deforms the Earth. This results in a relocation of masses, which has an indirect effect on the Earth's potential field - the solid Earth tides. If the Earth is assumed perfectly elastic, i.e. responding immediately to the deforming forces, the indirect effect on the potential is proportional to the direct potential: $\Delta V_j = k \cdot V_j$, where the *Love*-number k is the scaling factor. As the Earth is anelastic and the deformation responds to the attraction with a phase-shift, the *Love*-number k is not only different for each degree and order of the spherical harmonic expansion, but also obtains a small imaginary part and a frequency dependent part.

The IERS Conventions 2003 (McCarthy and Petit (2003)) propose to model the effect of solid Earth tides as changes to the potential coefficients $\bar{C}_{lm}$ and $\bar{S}_{lm}$ in two steps. In step 1, the contribution using the frequency independent part of the love numbers k_{lm} for degrees 2 and 3 as scaling factors to the potential given in equation A.60 is computed by:

$$\Delta\bar{C}_{lm} - i\Delta\bar{S}_{lm} = \frac{k_{lm}}{2l+1} \sum_{j=2}^{3} \frac{GM_j}{GM_\oplus} \Big(\frac{R_e}{r_j}\Big)^{l+1} \bar{P}_{lm}(\sin\theta_j) e^{-im\lambda_j} \ . \tag{A.62}$$

The Love numbers according to McCarthy and Petit (2003) are given in table A.1. Additionally the tides of degree 2 induce changes in the degree 4 coefficients, which can be computed by:

$$\Delta\bar{C}_{4m} - i\Delta\bar{S}_{4m} = \frac{k^{(+)}_{2m}}{5} \sum_{j=2}^{3} \frac{GM_j}{GM_\oplus} \Big(\frac{R_e}{r_j}\Big)^{3} \bar{P}_{2m}(\sin\Phi_j) e^{-im\lambda_j}, \quad (m = 0, 1, 2) \ . \tag{A.63}$$

n	m	$\Re k_{nm}$	$\Im k_{nm}$	k^+_{nm}
2	0	0.30190	-0.00000	-0.00089
2	1	0.29830	-0.00144	-0.00080
2	2	0.30102	-0.00130	-0.00057
3	0	0.093		
3	1	0.093		
3	2	0.093		
3	3	0.094		

Table A.1: Love numbers for solid Earth tides for an anelastic Earth.

In step 2 frequency dependent corrections are computed for the degree 2 coefficients:

$$\Delta\bar{C}_{2m} - i\Delta\bar{S}_{2m} = \eta_m \sum_{f(2,m)} \left(A^{ip}_m + iA^{op}_m\right) e^{i\theta_f} \text{ for } m = 0, 1, 2, \tag{A.64}$$

with $\eta_0 = 1$, $\eta_1 = -i$ and $\eta_2 = 1$. The in-phase amplitudes A^{ip}_m and out-phase amplitudes A^{op}_m are given in tables in McCarthy and Petit (2003). The corresponding frequencies θ_f can be computed from the Doodson-numbers given in those tables.

$$\theta_f = \mathbf{n} \cdot \boldsymbol{\beta} = \sum_{i=1}^{6} n_i \beta_i \ , \tag{A.65}$$

where $\boldsymbol{\beta}$ is the vector of Doodson's fundamental arguments (τ, s, h, p, N', p_s), and $\mathbf{n}$ is the vector of integer multipliers, which are encoded in the 6 digit Doodson numbers after Doodson (1921):

$$A = n_1(n_2 + 5)(n_3 + 5).(n_4 + 5)(n_5 + 5)(n_6 + 5) \ . \tag{A.66}$$

The β_i are linear combinations of the fundamental arguments of nutation theory F_i and the GMST:

$$\beta_1 = GMST + \pi - F_2 \ , \tag{A.67a}$$
$$\beta_2 = F_3 + F_5 \tag{A.67b}$$
$$\beta_3 = F_3 - F_4 + F_5 \ , \tag{A.67c}$$
$$\beta_4 = -F_1 + F_3 + F5 \ , \tag{A.67d}$$
$$\beta_5 = -F_5 \ , \tag{A.67e}$$
$$\beta_6 = -F_2 + F_3 - F_4 + F_5 \ , \tag{A.67f}$$

with

$$F_1 = 134.^\circ 963\,402\,51 + 1\,717\,915\,923.''2178t + 31.''8792t^2 + 0.''0516\,35t^3 - 0.''000\,244\,70t^4 \tag{A.68a}$$
$$F_2 = 357.^\circ 529\,109\,18 + 129\,596\,581.''0481t - 0.''5532t^2 + 0.''000\,136t^3 - 0.''000\,011\,49t^4 \tag{A.68b}$$
$$F_3 = 93.^\circ 272\,090\,62 + 1\,739\,527\,262.''8478t - 12.''7512t^2 - 0.''001\,037t^3 + 0.''000\,004\,17t^4 \tag{A.68c}$$
$$F_4 = 297.^\circ 850\,195\,47 + 1\,602\,961\,601.''2090t - 6.''3706t^2 + 0.''006\,593t^3 - 0.''000\,031\,69t^4 \tag{A.68d}$$
$$F_5 = 125.^\circ 044\,555\,01 - 6\,962\,890.''2665t + 7.''4722t^2 + 0.''007\,702t^3 - 0.''000\,059\,39t^4 \ . \tag{A.68e}$$

Solid Earth Pole Tide: The centrifugal effect of polar motion is creating an additional change to the potential, which can be developed to changes in the coefficients $\bar{C}_{21}$ and $\bar{S}_{21}$:

$$\Delta\bar{C}_{21} = -1.333 \cdot 10^{-9}(m_1 + 0.0115m_2) \ , \tag{A.69}$$
$$\Delta\bar{S}_{21} = -1.333 \cdot 10^{-9}(m_2 - 0.0115m_1) \ , \tag{A.70}$$

with the wobble variables (m_1, m_2) in arc seconds:

$$m_1 = x_p - 0''.054 - 0''.00083t_y \ , \tag{A.71}$$
$$m_2 = -y_p + 0''.357 + 0''.00395t_y \ , \tag{A.72}$$

where x_p and y_p are the polar coordinates in arc seconds and t_y is the number of Julian years since January 1, 2000 noon. The terms are a correction for the secular drift of the mean pole.

Permanent Tide: The zonal tide potential for degree 2 has a non-zero mean when averaged over time. If all corrections for direct and indirect tides were applied as mentioned in the previous paragraphs, this constant part would be added and the *tide free* potential would be obtained. This represents the potential field of the Earth without the permanent influence of other celestial bodies.

In order to obtain the full static gravity potential (*zero tide* potential) and only correct for time variable signals - which is recommended by McCarthy and Petit (2003) - the constant part of $\Delta\bar{C}_{20}$ has to be restored again and subtracted from the correction:

$$\Delta\bar{C}_{20} = \Delta\bar{C}^{*}_{20} - \left\langle \Delta\bar{C}_{20} \right\rangle \ , \tag{A.73}$$

where $\Delta\bar{C}^{*}_{20}$ is the correction computed according to equation A.64 and $\left\langle \Delta\bar{C}_{20} \right\rangle$ is the constant part:

$$\left\langle \Delta\bar{C}_{20} \right\rangle = A_0 H_0 k_{20} = (4.4228 \cdot 10^{-8}) \cdot (-0.31460) \cdot 0.3010 \ . \tag{A.74}$$

A.4.3 Ocean Tides

Similar to the solid Earth, the oceans are deformed by the tides and the transport of the water causes variations in the gravity potential. In order to model these variations, the height of tidal waves is separated in dominant frequencies θ_s and each frequency is expanded into a spherical harmonic series, distinguishing between retrograde $(C^{+}_{slm}, S^{+}_{slm})$ and prograde $(C^{-}_{slm}, S^{-}_{slm})$ waves. The effect on the potential coefficients can be computed by:

$$\Delta\bar{C}_{lm} = F_{lm} \sum_{s(l,m)} \left[\left(C^{+}_{snm} + C^{-}_{snm}\right) \cos\theta_s + \left(S^{+}_{snm} + S^{-}_{snm}\right) \sin\theta_s \right] \ , \tag{A.75a}$$

$$\Delta\bar{S}_{lm} = F_{lm} \sum_{s(l,m)} \left[\left(S^{+}_{snm} - S^{-}_{snm}\right) \cos\theta_s - \left(C^{+}_{snm} - C^{-}_{snm}\right) \sin\theta_s \right] \ , \tag{A.75b}$$

with

$$F_{lm} = \frac{4\pi G \rho_w}{g_e} \sqrt{\frac{(n+m)!}{(n-m)!(2n+1)(2-\delta_{lm})}} \left(\frac{1+k'_n}{2l+1} \right) \ , \tag{A.76}$$

where $g_e = 9.7803278\mathrm{m/s}^2$ is the mean equatorial gravity, $G = 6.673 \cdot 10^{-11}\mathrm{m}^3\mathrm{kg}^{-1}\mathrm{s}^{-2}$ is the constant of gravitation, $\rho_w = 1025\mathrm{kgm}^{-3}$ is the density of seawater and the k'_n are the load deformation coefficients.

In this work the FES 2004 ocean tide model (Le Provost (2001)) has been employed. It should be noted, that values of ocean tides are generally given in cm and have to be divided by 100 when used in equation A.75.

A.4.4 Temporal Variations due to Geophysical Fluids

Next to the tides, mass transports of geophysical fluids cause temporal variations of the gravity potential. In order to determine the static part of the gravity field, the temporal mass variations have to be modeled and the measurements have to be corrected for. This has first been done for the effects of atmosphere and oceans for the GRACE mission and is often referred to as *de-aliasing*. This means that the high frequent signal of the temporal variations which is superimposed to the signal of the static gravity field, is removed from the measurements to extract the static potential only.

A simplified approach to assess the the influence is to model the mass variations w.r.t. a mean mass distribution over a certain period and evolve it into a spherical harmonic series expansion using the classical integration approach (cf. Heiskanen and Moritz (1967)). But instead of integrating over three-dimensional mass elements, a single layer approximation is applied and one integrates surface pressure values P_s over the Earth's surface:

$$\Delta\bar{C}_{lm} = \frac{R^2\,(1+k_l)}{(2l+1)Mg} \iint\limits_{\text{Earth}} (P_s - \bar{P}_s)\bar{P}_{lm}(\cos\theta)\cos m\lambda \,\mathrm{d}S \;, \tag{A.77}$$

$$\Delta\bar{S}_{lm} = \frac{R^2\,(1+k_l)}{(2l+1)Mg} \iint\limits_{\text{Earth}} (P_s - \bar{P}_s)\bar{P}_{lm}(\cos\theta)\sin m\lambda \,\mathrm{d}S \;, \tag{A.78}$$

where $\bar{P}_s$ is the mean surface pressure, M the mass of the Earth and g the mean gravitational acceleration. Similar to the ocean tides, the mass variations not only create a direct variation of the gravity field, but also deform the Earth by loading. This is represented by the term $(1 + k_l)$. As $k_l < 0$, the effect of the gravitating masses is diminished by the load deformation. The load coefficients k_n are given by Dong et al. (1996).

The surface pressure values P_s are derived from meteorological data on a regular grid in intervals of 6 hours (cf. Flechtner (2007)) and the $\bar{C}_{lm}$and $\bar{S}_{lm}$values are computed at 0h, 6h, 12h and 18h every day. In order to compute the corrections for accelerations on the satellite or the gravity tensor at a given epoch, a corresponding set of coefficients is obtained by linear time interpolation from the the two neighboring sets and using this set in a spherical harmonic synthesis (cf. equ. 2.12).

This simplified approach has the disadvantage, that all mass variations of the atmosphere are assumed be condensed on the surface of the Earth. A more elaborate approach takes into account several density layers of the atmosphere, as well as a digital elevation model for a more accurate representation of the Earth's surface. A vertical integration step ensures that the masses are taken at their correct position. For details cf. Flechtner (2007).

The atmosphere models are entered also into the computation of ocean models as the atmosphere is one of the driving forces of the ocean. The ocean models delivers ocean bottom pressure values which are interpolated to the same spatial and temporal resolution of the atmospheric surface pressure values. They are combined with the atmosphere model and used to derive coefficient sets $\Delta\bar{C}_{lm}$ and $\Delta\bar{S}_{lm}$ which represent the combined effect of atmosphere and oceans.

The remaining unmodeled mass variations, which include hydrology, ice, model errors from atmosphere and oceans and other minor effects still create a significant signal in the gravity potential, that can be detected by GRACE (but not separated), which is represented by the monthly GRACE gravity field solutions. In order to improve the de-aliasing product for the GOCE mission, these temporal solutions from GRACE are interpolated to fit the 6-hourly resolution of the atmosphere and ocean product (see ESA (2005)) and the GOCE observations will be corrected for.

Bibliography

Austen G., Reubelt T. (2000). Räumliche Schwerefeldanalyse aus semi-kontinuierlichen Ephemeriden niedrigfliegender GPS-vermessender GPS Satelliten vom Typ CHAMP, GRACE und GOCE. Diplomarbeit, Universität Stuttgart.

Baur O. (2007). Die Invariantendarstellung in der Satellitengradiometrie. Band 609 der Reihe C. Deutsche Geodätische Kommission, München.

Dong D., Gross R. S., Dickey J. O. (1996). Seasonal Variations of the Earth's Gravity Field: An Analysis of Atmospheric Pressure, Ocean Tidal and Surface Water Excitation. *Geophysical Research Letters*, Vol. 23, No. 7, p. 725-728.

Doodson A. T. (1921). The Harmonic Development of the Tide-Generating Potential. *Proceedings of the Royal Society*, A(100):305-329.

ESA (1999). *Gravity Field and Steady-State Ocean Circulation Mission*. ESA Publications Division, Reports for Mission Selection - The Four Candidate Earth Explorer Core Missions, ESA-SP 1233(1).

ESA (2005). GOCE Level 2 Data Handbook. GO-MA-HPF-GS-0110.

Flechtner F. (2007) AOD1B Product Description Document. GRACE 327-750, GR-GFZ-AOD-0001, Rev. 3.1, GeoForschungsZentrum Potsdam.

Földváry L., Švehla D., Gerlach C., Wermuth M., Gruber T., Rummel R., Rothacher M., Frommknecht B., Peters T., Steigenberger P. (2004). Gravity Model TUM-2Sp Based on the Energy Balance Approach and Kinematic CHAMP Orbits. *Proceedings of the 2nd CHAMP Science Meeting*, GeoForschungZentrum Potsdam, 1-4 September, 2003. Springer-Verlag.

Förste C. (2002). Format Description: The CHAMP Data Format. CH-GFZ-FD-001, GeoForschungsZentrum Potsdam.

Förste C., Flechtner F., Schmidt R., König R., Meyer U., Stubenvoll R., Rothacher M., Barthelmes F., Neumayer H., Biancale R., Bruinsma S., Lemoine J. M., Loyer S. (2006). A Mean Global Gravity Field Model from the Combination of Satellite Mission and Altimetry/Gravimetry Surface Data - EIGEN-GL04C. *Geophysical Research Abstracts*, Vol. 8, 03462.

Gerlach C., Földváry L., Švehla D., Gruber T., Wermuth M., Sneeuw N., Frommknecht B., Oberndorfer H., Peters T., Rothacher M., Rummel R., Steigenberger P. (2003). A CHAMP-only gravity field model from kinematic orbits using the energy integral. *Geophysical Research Letters*, Vol. 30, No. 20, 2037, doi:10.1029/2003GL018025.

Gerlach C. (2003). A note on the use of energy integrals for gravity field recovery. IAPG TU Munich, internal note.

Gerstl M. (1980) On the recursive computation of the integrals of the associated Legendre functions. *Manuscripta Geodaetica*, 5, 181199.

Gruber T. (2004). Validation Concepts for Gravity Field Models from Satellite Missions. Proceedings of Second International GOCE User Workshop "GOCE, The Geoid and Oceanography", ESA-ESRIN, Frascati, 8.-10. March 2004.

Goad C. C. (1987). An Efficient Algorithm for the Evaluation of Inclination and Eccentricity Functions. *Manuscripta Geodaetica*, Vol 12, pp 11-15.

Heiskanen W. A., Moritz H. (1967). *Physical Geodesy*. W.H. Freeman Publications Co., San Francisco.

Jäggi A., Beutler G., Bock H., Hugentobler U. (2006). Kinematic and highly reduced-dynamic LEO orbit determination for gravity field estimation. In: Rizos C. and Trgoning P. (eds.) *Dynamic Planet Monitoring and Understanding a Dynamic Planet with Geodetic and Oceanographic Tools*. pp. 354-361, Springer, ISBN 3-540-49349-2.

Jekeli C. (1999). The Determination of Gravitational Potential Differences from Satellite-to-Satellite Tracking. *Celestial Mechanics and Dynamical Astronomy*, 75:85-101, Kluiver Academic Publishers, Netherlands.

Kaula W. M. (1966). *Theory of Satellite Geodesy*. Blaisdell Publishing Company.

Koch K. R., Kusche J. (2001). Regularization of geopotential determination from satellite data by variance components. *Journal of Geodesy*, 76(11-12):629-640.

Lanczos C. (1949). *The Variational Principles of Mechanics*. University of Toronto Press, (1986) as Dover Pocket.

Lanczos C. (1956). *Applied Analysis*, Prentice-Hall, Englewood Cliffs, N.J., (1988) as Dover Pocket.

Landau L. D., Lifschitz E. M.(1976). *Mechanik*. Akademie Verlag Berlin.

Lawson C. L., Hanson R. J., Kincaid D., Krogh F. T. (1979). Basic Linear Algebra Subprograms for FORTRAN usage. *ACM Transactions on Mathematical Software*, 5, pp. 308–323.

Lemoine F. G., Kenyon S. C., Factor J. K., Trimmer R. G., Pavlis N. K., Chinn D. S., Cox C. M., Klosko S. M., Luthke S. B., Torrence M. H., Wang Y. M., Williamson R. G., Pavlis E. C., Rapp R. H., Olson T. R. (1998). The Development of the Joint NASA GSFC and National Imagery and Mapping Agency Geopotential Model. NASA Technical Paper NASA/TP-1998-206861, Goddard Space Flight Center, Greenbelt, USA.

Le Provost C. (2001). Ocean Tides. In: Fu L. L. and Cazenave A. (eds.), *Satellite Altimetry and Earth Sciences*. Springer, 267-303.

Mayer-Gürr T., Ilk K. H., Eicker A., Feuchtinger M. (2005). ITG-CHAMP01: a CHAMP gravity field model from short kinematic arcs over a one-year observation period. *Journal of Geodesy*, 78(8):462-480.

Mayer-Gürr T. (2006). Gravitationsfeldbestimmung aus der Analyse kurzer Bahnbögen am Beispiel der Satellitenmissionen CHAMP und GRACE. Dissertation, Rheinische Friedrich-Willhelm-Universität, Bonn.

McCarthy D. D. and Petit G. (2003). IERS Conventions (2003). IERS Technical Note 32, Frankfurt am Main: Verlag des Bundesamts für Kartographie und Geodäsie, 2004. 127 pp., paperback, ISBN 3-89888-884-3 (print version).

Metzler B. (2007). Spherical Cap Regularization - A Spatially Restricted Regularization Method Tailored to the Polar Gap Problem. Dissertation, TU Graz.

Migliaccio F., Reguzzoni M., Sansò F. (2004). Space-wise approach to satellite gravity field determination in the presence of coloured noise. *Journal of Geodesy*, Vol. 78, pp. 304-313.

Newton I. (1687). *Philosophiae Naturalis Principia Mathematica*.

Niemeier W. (2002). *Ausgleichungsrechnung*, de Gruyter, Berlin.

Pail R., Wermuth M. (2003). GOCE SGG and SST quick-look gravity field analysis. *Advances in Geosciences* (2003) 1:1-5, European Geosciences Union.

Pail R., Preimesberger R., Wermuth M. (2004). GOCE Quick-Look Gravity Field Analysis of satellite gravity gradiometry and high-low satellite-to-satellite tracking data. Proceedings of the 1st Workshop on International Gravity Field Research Graz 2003, *Österreichische Beiträge zur Meteorologie und Geophysik*, University of Vienna.

Pail R., Metzler B., Lackner B., Preimesberger T., Höck E., Schuh W. D., Alkhatib H., Boxhammer C., Siemes C., Wermuth M. (2006). GOCE Gravity Field Analysis in the Framework of the HPF: Operational Software System and Simulation Results. *Proceedings 3rd GOCE User Workshop*, Frascati, ESRIN, November 2006, ESA.

Pail R., Metzler B., Preimesberger T., Lackner B., Wermuth M. (2006). GOCE Quick-Look Gravity Field Analysis in the Framework of HPF. *Proceedings 3rd GOCE User Workshop*, Frascati, ESRIN, November 2006, ESA.

Plank G. (2004). Numerical solution strategies for the GOCE mission by using cluster technologies. Dissertation, Technical University Graz.

Reigber C. (1969). Zur Bestimmung des Gravitationsfeldes der Erde aus Satellitenbeobachtungen. Band 137 der Reihe C. Deutsche Geodätische Kommission, München.

Reigber C., Lühr H., Schwintzer P. (1998). Status of the CHAMP mission. In: Rummel R., Drewes H., Bosch W., Hornik H. (eds) *Towards an Integrated Global Geodetic Observation System (IGGOS)*, pp. 63-65, Springer, ISBN 3-540-22804-7.

Reigber Ch., Schwintzer P., Neumayer K.-H., Barthelmes F., König R., Förste Ch., Balmino G., Biancale R., Lemoine J.-M., Loyer S., Bruinsma S., Perosanz F., Fayard T. (2003). The CHAMP-only Earth Gravity Field Model EIGEN-2. *Advances in Space Research* 31(8), 1883-1888, 2003 (doi: 10.1016/S0273–1177(03)00162-5).

Reigber Ch., Jochmann H., Wünsch J., Petrovic S., Schwintzer P.,Barthelmes F., Neumayer K.-H., König R., Förste Ch., Balmino G., Biancale R., Lemoine J.-M., Loyer S., Perosanz F. (2005) Earth Gravity Field and Seasonal Variability from CHAMP . In: Reigber Ch., Lühr H., Schwintzer P., Wickert J. (eds.) *Earth Observation with CHAMP - Results from Three Years in Orbit*, Springer, Berlin, 25-30, 2005.

Rummel R. (1992). *Physical Geodesy I.* Collegediktaat, Technische Universiteit Delft.

Savitzky A., Golay M. J. E. (1964). Smoothing and Differentiation of Data by Simplified Least Squares Procedures *Analytical Chemistry*, 36, 1627.

Schneider M. (1968). A General Method of Orbit Determination. Library Translation, Vol. 1279, Royal Aircraft Establishment, Minstry of Technology, Farnborough, England.

Schuh W. D. (1996). Tailored Numerical Solution Strategies for the Global Determination of the Earth's Gravity Field. Mitteilungen der geodätischen Institute der Technischen Universität Graz, Folge 81.

Schwintzer P. (1960). Sensitivity Analysis in Least Squares Gravity Field Modelling Redundancy Decomposition of Stochastic A Priori Information. Deutsches Geodätisches Forschungsinstitut, München.

Snyder J. P. (1987). *Map Projections: A Working Manual.* U.S. Geological Survey Professional Paper 1395, Washington.

Švehla D., Rothacher M. (2002). Kinematic orbit determination of LEOs based on zero or double difference algorithms using simulated and real SST GPS data. *IAG Proceedings, Symposium No. 125*, Vistas for Geodesy in the New Millenium, Springer Verlag, Heidelberg.

Švehla D., Rothacher M. (2004). Two Years of CHAMP Kinematic Orbits for Geosciences. European Geosciences Union, 1st General Assembly, 2530 April 2004, Nice, France. *Geophysical Research Abstracts*, European Geophysical Society Vol. 6. ISSN:10297006.

Sharifi M. A., Keller W. (2005). GRACE Gradiometer. In: Jekeli C, Bastos L, Fernandes J (eds), Gravity Geoid and Space Mission, *International Association of Geodesy Symposia*, Vol. 129, 42-47.

Sneeuw N. J. (1991). *Inclination Functions.* Delft University of Technology.

Sneeuw N. J. (2000). A Semi-Analytical Approach to Gravity Field Analysis from Satellite Observations. Band 527 der Reihe C. Deutsche Geodätische Kommission, München.

Standish E. M. (1998). JPL Planetary and Lunar Ephemerides, DE405/LE405, JPL IOM 312.F-98-048.

Tapley B D and Reigber C (2001), The GRACE Mission: Status and future plans, in EOS, Transactions, 82(47), American Geophysical Union.

Torge W. (1980). *Geodesy.* W. de Gruyter, Berlin.

Wenzel H. G. (1999). Ultra High Degree Geopotential Models GPM98A and GPM98B, Paper presented at 2nd IGC-IGeC Meeting Trieste 1999.

Wermuth M. (2001). Global Spherical Harmonic Analysis of GOCE-SGG Measurements with a Full Normal Equation System. Diplomarbeit, Technische Universität München.

Wermuth M., Földváry L., Švehla D., Gerlach C., Gruber T., Frommknecht B., Peters T., Rothacher M., Rummel R., Steigenberger P. (2005). Gravity Field Modelling From CHAMP Kinematic Orbits Using the Energy Balance Approach. *Proceedings of the Joint CHAMP / GRACE Science Meeting, July 6-8 2004*, GeoForschungsZentrum Potsdam.

Wertz J.R. (1988). Editor: *Spacecraft Attitude Determination and Control*, Kluwer Academic Publishers.

Wu S.C., Yunck T.P., Thronton C.L. (1991). Reduced-dynamic technique for precise orbit detrmination of low Earth satellites. *Journal of Guidance, Control and Dynamics*, 14(1), 24-30.

Yunck T.P., Wu S.C., Wu J.T., Thornton C.L. (1990). Precise Tracking of remote sensing satellites with the Global Positioning System. *IEEE Transactions on Geoscience and Remote Sensing*, 28(1), 108-116.